LAVA–SUBSTRATE HEAT TRANSFER: IMPLICATIONS FOR THE PRESERVATION OF VOLATILES IN THE LUNAR REGOLITH

A DISSERTATION SUBMITTED TO THE GRADUATE DIVISION OF THE UNIVERSITY OF HAWAIʻI AT MĀNOA IN PARTIAL FULFILLMENT OF THE REQUIREMENTS FOR THE DEGREE OF

DOCTOR OF PHILOSOPHY

IN

GEOLOGY AND GEOPHYSICS

MAY 2014

By:

M. Elise Rumpf

Dissertation Committee:

Sarah A. Fagents, Chairperson
Jeffrey Gillis-Davis
Matthew Patrick
G. Jeffrey Taylor
John Allen III

ACKNOWLEDGEMENTS

First and foremost, I would like to thank my advisor, Sarah Fagents, for years of selfless dedication, patience, and support. Her expertise in the field, in the lab, and on a computer has been an inspiration. This dissertation would not have been possible without Sarah. Thank you to my committee, Jeff Taylor, Jeff Gillis-Davis, Matt Patrick, and John Allen, who have graciously given their time and expertise; to Bruce Houghton for field trips, use of the physical volcanology lab, and international teleconferences; to John Sinton, Scott Rowland, and Andy Harris for filling my brain with facts about Hawaiian volcanics; to Rob Wright for use of the FLIR camera and related equipment; and to Chris Hamilton, for the guidance, the long talks, and the fantastic ideas.

Mahalo to Heidi Needham for always being ready for adventure and for never complaining about the number of lava flows I needed to be mapped. Thanks to Sammie Jacob and the NASA Space Grant Consortium. Thank you, Ethan Kastner and Eric Pilger for answering all of my questions and printing all of my posters. Many thanks to the University of Hawai‘i Department of Art and Art History, Fred Roster, Jen Rubin, and Gideon Gertl for their time and the use of their foundry. Amber Fischer, thank you for the Matlab help.

Thank you to my officemates – Myriam Telus and Meryl McDowell – for dealing with my clutter and always being ready for a chat; to all of the Geology grads – old and new – for the adventures, the discussions, and coffee time. Thank you to Amber, Ginger, Andrea, Katy, Alyssa, Mara, Alice, Jenny, Patrick, Omar, my goon, and Sebastian and everyone I’ve missed for the friendships and the distractions. To the Waikiki Beach Boys Canoe Club and all of the inspiring people who make it great– thanks for keeping me

sane. Without you, I may have graduated a little sooner but I wouldn't have gotten to know the beauty and the soul of Hawai‘i. Besides, racing the Napali Challenge gave me the inspiration for Chapter 4. Paddling IS good for science.

This dissertation could not have been completed without the generous financial support of many institutions. Mahalo to the Department of Geology and Geophysics and to Greg Moore for invaluable teaching assistant positions, the Earth and Planetary Science Fellowship that brought me here, and the Fred M. Bullard Graduate Fellowship, which helped me finish. The National Science Foundation Graduate Research Fellowship Program provided my salary for several years and funded a trip to present my research in Europe. The UH Graduate Student Organization also helped to fund that trip. Funding from the Jack Kleinman Grant for Volcano Research allowed for expenses related to field work and experiments.

Last, but not least, to my amazing family – thank you for your love and kindness and for supporting me from far, far away.

On-on!

ABSTRACT

This dissertation examines the preservation potential of exogenous particles in the lunar regolith through numerical models, laboratory experiments, remote sensing studies, and field investigations. Models and experiments of the thermal interaction between lava flows and the underlying substrate provide estimates of the maximum depths to which exogenous volatiles will be destroyed by an overlying lava flow. A lunar analog study using Hawaiian lava flow deposits suggests that current measurements of mare basalt flow thicknesses are overestimates.

Numerical models were used to determine the depths to which pertinent volatiles will be baked out of paleoregoliths on the Moon. Ancient regolith deposits containing exogenous particles may have been protected from the space environment by an overlying lava flow provided the lava flow did not heat the entire deposit, destroying the particle records. The inclusion of latent heat release and temperature- and depth-dependent thermophysical properties of materials is imperative to the accuracy of lava-substrate heat transfer models. Simulations revealed that implanted volatiles would be fully preserved at depths of 20 cm beneath a 1 m thick lava flow on the lunar surface.

Laboratory experiments allowed the *in situ* measurements of heat flow from molten basalt from Kīlauea Volcano, Hawai‘i into GSC-1, a lunar regolith simulant. Melt layers 8 – 10 cm thick heated simulant to particle-volatilizing temperatures to maximum depths of 5.6 – 7.2 cm. These depths represent the maximum depths to which exogenous particles will be volatilized on the Moon. Numerical simulations of experiments constrained the temperature-dependency of the effective thermal conductivity of GSC-1 to vary from 0.35 – 0.45 W m^{-1} K^{-1} at 23 °C and 0.65 – 0.80 W m^{-1} K^{-1} at 1227 °C.

Ground-truthing of remote sensing identifications of layered lava sequences in valley walls on O‘ahu, Hawai‘i reveal that lava flow thicknesses are overestimated in image interpretations. The study of eight transects at three locations on O‘ahu determined that layer thicknesses derived from image interpretations were up to 6.3 times larger than mean flow thicknesses measured in the field. Misinterpretations are primarily caused by outcrops that contain more than one lava flow unit but appear as a single layer in satellite imagery. Lava layers were also identified in Lunar Reconnaissance Orbiter Camera images. Measured average flow thicknesses of mare basalts, found to be 1.2 – 29.5 m, are representative of the maximum thickness of the flows identified, as image resolution does not allow for confirmation of the number of flows in visible outcrops.

TABLE OF CONTENTS

LIST OF TABLES

LIST OF FIGURES

CHAPTER 1.

INTRODUCTION

1.1 VOLATILE PRESERVATION IN PALEOREGOLITHS

The primary intent of research included in this dissertation was the determination of the potential preservation of ancient extra-lunar particles in paleoregoliths near the lunar surface. Having no atmosphere or magnetosphere and little internal geologic activity, the Moon potentially holds records of events in the neighborhood of the Earth since soon after formation of the Solar System. Regolith samples retrieved during the Apollo missions contained exogenous particles, including solar wind and solar flare particles, and the cosmogenetic products of galactic cosmic ray impacts [*Wieler et al.*, 1996; *National Research Council (NRC)*, 2007] and material ejected from the early Earth and other rocky bodies [*Spudis*, 1996; *Armstrong et al.*, 2002; *Ozima et al.*, 2005; *Crawford et al.*, 2008; *Ozima et al.*, 2008; *Armstrong*, 2010; *Joy et al.*, 2011, 2012]. However, the surface regolith samples were oversaturated from prolonged exposure to the space environment [*McKay et al.*, 1991; *Joy et al.*, 2011]. A paleoregolith that was exposed to space and subsequently covered by a lava flow could hold particles that, if retrieved, would give insight into ancient solar or galactic activity. The lava flow would provide protection of the underlying deposits and provide solid material to radiometrically date to determine exposure age [*McKay et al.*, 1989; *Spudis*, 1996; *Crawford et al.*, 2007, 2010; *McKay*, 2009; *Spudis and Taylor*, 2009]. Discovery of such records could reveal much about the early Solar System. However, the lava flow will have heated the regolith, volatilizing the exogenous particles and destroying the pertinent record. Chapters 2 and 3 of this dissertation focus on determining the depths to which a lava flow will destroy exogenous particle-rich deposits in underlying regoliths.

Critical to understanding preservation of exogenous particles in paleoregolith

covered by lava flows is a clear understanding of lunar lava flow thickness. The thickness of a lava flow will determine the amount of heat available to volatilize particles in the substrate [this dissertation, *Chapter 2*]. Future missions to the lunar surface will rely on accurate measurements of the thicknesses of alternating layers of lava and regolith to determine the potential of uncovering exogenous particles in a given location. Apollo 15 astronauts imaged the layered wall of Hadley Rille, revealing flows ranging in thickness from < 1 m to ~ 20 m [*Howard and Head*, 1972; *Howard et al.*, 1972; *Swann et al.*, 1972; *Spudis et al.*, 1988; *Vaniman et al.*, 1991]. Orbital data has given mare flow unit thicknesses over a broad range: 1–96 m [*Gifford and El-Baz*, 1981], ~30–60 m [*Hiesinger et al.*, 2002], and most recently, 2–14 m [*Robinson et al.*, 2012]. Chapter 4 focuses on confirming the accuracy of mare flow thicknesses determined through remote sensing techniques.

1.2 DISSERTATION OUTLINE

This dissertation contains three main sections that examine various aspects of lava-substrate heat transfer and resulting volatile preservation in the lunar regolith. It covers a broad range of techniques to approach this problem, including numerical simulations, laboratory experiments, interpretation of remote sensing imagery, and fieldwork.

Chapter 2 presents numerical simulations of lava–regolith heat transfer in a lunar environment. The minimum volatilization temperatures of specific particles are used as key parameters to determine the maximum depths to which exogenous volatiles will be heated. Emphasis is placed on the comparison of the effects of constant versus temperature- and depth-dependent material property definitions. This chapter also

examines the effects of lava flow thickness, substrate material, and diurnal temperature changes on heat transfer within the system. Chapter 2 was published in The Journal of Geophysical Research: Planets in 2013.

Chapter 3 describes a set of experiments designed to measure the direct heat transfer from molten Kīlauea basalt into GSC-1, a lunar regolith simulant. The experiments verify our previous numerical models and provide upper limits on the depths to which exogenous particles will be destroyed in paleoregoliths heated by overlying lava flows. This chapter also examines the temperature-dependence of the regolith simulant effective thermal conductivity. Chapter 3 has been presented at several scientific meetings and will be submitted Earth and Planetary Science Letters.

Chapter 4 investigates mare basalt flow thicknesses through terrestrial analogs. Sequences of layered lava flows were mapped in terrestrial and lunar satellite images to determine average flow thicknesses. Terrestrial sites were then visited and *in situ* lava flow thicknesses were measured to test remote sensing interpretations. Comparison of image interpretations to field observations at terrestrial locations suggests inaccuracies in lunar flow thickness estimates. Chapter 3 will be submitted to Icarus.

CHAPTER 2.

NUMERICAL MODELING OF LAVA–REGOLITH HEAT TRANSFER ON THE MOON AND IMPLICATIONS FOR THE PRESERVATION OF IMPLANTED VOLATILES

Published in its present form as Rumpf, M. E., S. A. Fagents, I. A. Crawford, and K.H. Joy (2013), Journal of Geophysical Research: Planets, 118, 382–397, doi:10.1029/2012JE004131.

2.1 ABSTRACT

We have performed a series of numerical simulations of heat transfer between lunar lava flows and the underlying regolith with the goal of determining the depths in the substrate beneath which implanted extralunar volatiles would survive outgassing by the downward-propagating heat pulse. Exogenous materials of interest include solar wind and solar flare particles, and the cosmogenic products of galactic cosmic ray (GCR) particles emplaced in the lunar regolith early in Solar System history. Extraction and analysis during future lunar missions would yield information about the evolution of the Sun and inner Solar System environment. Particles implanted in regolith deposits may be protected from gardening and saturation if buried by a lava flow, but must be sufficiently deep in the regolith to survive the consequent heating. Our simulations include detailed treatments of lava and regolith thermophysical properties (thermal conductivity, specific heat capacity), which vary widely over the temperature range relevant to lava flows in the lunar environment (~200 to >1500 K). Simulations adopting temperature-dependent properties, together with a treatment of latent heat of lava crystallization, indicate that implanted volatiles would be fully preserved at depths greater than 20 cm beneath 1 m thick lava flows, ~60% deeper than predicted by simulations employing constant properties. These results highlight the necessity of appropriate prescription of material properties. Consideration of the range of lunar lava flow thicknesses allows us to determine the range of depths from which pristine samples may be recovered.

2.2 INTRODUCTION

Exposed directly to space, the lunar surface is continuously bombarded with radiation and micrometeorites, and has been disrupted on local to global scales by impacts of asteroid and comet debris. These impact events excavate and redistribute material. Over time this process fragments, comminutes, and mixes the surface material forming a poorly sorted regolith [*McKay et al.*, 1991; *Korotev*, 1997; *Lucey et al.*, 2006]. This surface regolith becomes implanted with solar wind, solar flare, and the cosmogenic products of galactic cosmic ray (GCR) particles as it forms [*Wieler et al*., 1996; *NRC*, 2007]. It may also contain early materials from the Earth and other planetary bodies that were deposited on the Moon as meteorites [*Spudis,* 1996; *Armstrong et al*., 2002; *Ozima et al.*, 2005, 2008; *Armstrong*, 2010; *Crawford et al.*, 2008; *Joy et al.,* 2011]. In contrast to the ever-changing surface of Earth, the lunar surface has been exposed to such processes for billions of years. Having no atmosphere or magnetosphere and little internal geologic activity, the Moon has been passively recording events in the neighborhood of the Earth since soon after formation of the Earth–Moon system. Location and extraction of caches of exogenous materials during future lunar missions could provide valuable information on the variability of composition and flux of incoming materials over the lifetime of the Solar System.

One of the goals of the Apollo missions was to decipher solar wind, cosmic ray and bombardment history from volatiles returned in regolith core samples and soil scoops collected from the upper three meters of the lunar regolith. However, because of many millions of years of exposure of the upper portion of the regolith to space, the records of exogenous processes in these samples are often highly complex and difficult to

constrain [*McKay et al.*, 1991; *Joy et al.,* 2011]. In contrast, buried regolith layers (paleoregoliths) not exposed at the surface will have been protected from sustained bombardment by an overlying layer (Figure 2.1) thereby providing a snapshot of the exogenous particle population. Such a protective overlying layer might be provided by a lava flow, a flow of impact melt, an impact ejecta blanket, or a fall deposit from a pyroclastic eruption. A lava flow would protect the underlying paleoregolith and provide a rock sample to date isotopically, determining the enclosure age of the underlying regolith [*McKay et al*., 1989; *Spudis*, 1996; *Crawford et al*., 2007, 2010; *McKay*, 2009; *Spudis and Taylor*, 2009]. Although lava will potentially protect a paleoregolith and implanted materials from further bombardment, disruption, and gardening, it will also heat the regolith, potentially volatilizing the embedded particles and damaging the record of solar or galactic particle implantation and any fragments of volatile-bearing cometary or asteroid material. Heating experiments performed on a range of doped lunar and terrestrial samples, meteorites, and lunar simulants determined the temperature ranges over which specific volatiles are released [*Gibson and* Johnson, 1971; *Simoneit et al.,* 1973; *Haskin and Warren*, 1991; *Fegley and Swindle*, 1993]. A summary of those results (Table 2.1) shows that, although some chemical species lightly adsorbed on mineral

Table 2.1 Temperature ranges of volatile release.

Species	Temperature Range
H_2, He	300–700 °C (573–973 K)
CH_4, Ne, Ar	500–700 °C (773–973 K)
CO, CO_2, N_2, Xe	>700 °C (>973 K)

[*Simoneit et al.*, 1973]

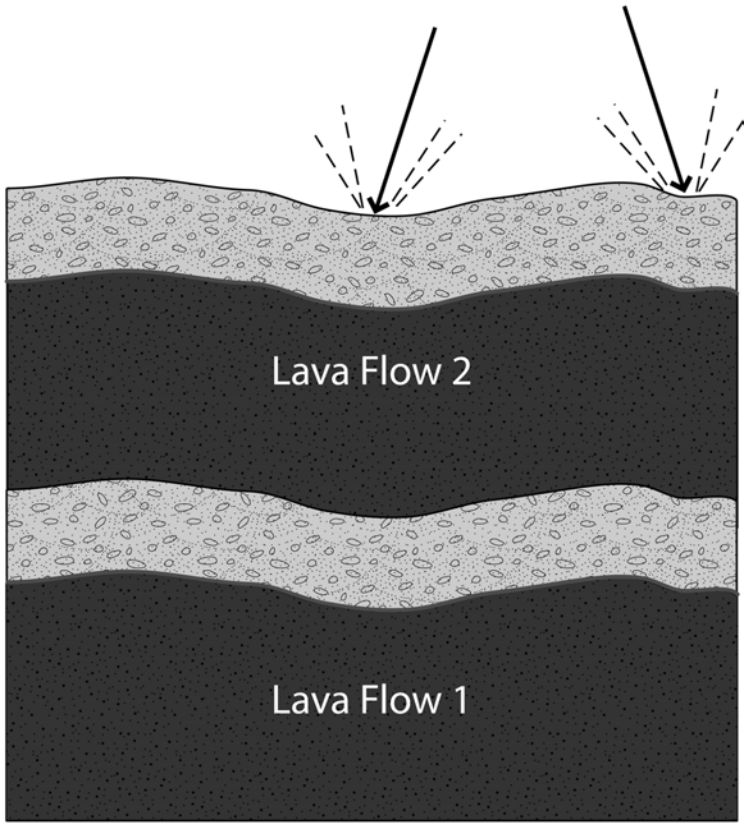

Figure 2.1 Paleoregolith development on the lunar surface.

Paleoregolith development on the lunar surface. After emplacement of Lava Flow 1, micrometeorites, solar flare particles, and galactic cosmic ray particles cause sputtering, vaporization, agglutination, and comminution of the surface of the flow, developing a layer of regolith. Particles from the solar wind, solar flares, and the products of galactic cosmic rays and impacting planet, asteroid, and comet fragments will become embedded in the regolith. Subsequently Lava Flow 2 covers the regolith layer, protecting it from further bombardment and heating it, volatilizing many of the implanted particles. Exposure to the space environment leads to development of regolith on the surface of the new flow. Repetition of this cycle creates a series of strata containing a time series archive of solar particles.

surfaces might be released at temperatures as low as ~570 K, many entrapped species and reaction-produced molecules will remain in the regolith until heated to a temperature range of 970–1600 K.

To quantify the depths to which a lava flow will heat a substrate, we have developed a numerical model based on that of *Fagents et al.* [2010]. The current model improves upon the previous by including explicit treatment of temperature-dependent thermophysical properties of both lava and substrate. A common strategy used in many thermal models of lava flows is to omit the temperature- and time-dependence of material properties, instead using constant parameters to derive analytical solutions, to save computational time, or to help ensure the stability of numerical solutions. Such approximations are sufficient for first-order accuracy; however, for detailed descriptions of lava heat transfer, inclusion of property dependences is a key element. Thermal models of lunar and terrestrial lava flows benefit from the inclusion of temperature-dependent properties and a clear definition of substrate properties. The values of thermophysical properties will vary greatly over the temperature range that a lava flow experiences from eruption [at ~1450–1715 K; *Murase and McBirney*, 1970; *Taylor et al.*, 1991; *Williams et al*., 2000] to ambient temperature on Earth (~ 295 K; 22 °C) or on the Moon [~ 200 K; -73 °C; *Vaniman et al*., 1991]. The thermophysical properties of the both lava and substrate influence the temperature distribution throughout the system. However, the particulate regolith possesses contrasting properties to those of the lava; of particular significance is the low thermal conductivity. Addressing the unique properties of the substrate beneath a lava flow is, thus, important for understanding the heat budget of the system.

In this paper, we investigate the effects of temperature- and depth-dependent definitions of material properties in a lava–substrate thermal model. Beginning with the constant thermophysical properties of the lava and substrate used by *Fagents et al*. [2010], we introduce, in turn, treatments of latent heat of crystallization, temperature-dependent lava and regolith thermal conductivities and specific heat capacities, and depth-dependent regolith density. The effects of including each temperature- or depth-dependent property are first compared to the constant-value case of *Fagents et al.* [2010], and then all variables are included in a detailed simulation to compare with the results of constant-value simulations. We also include a simulation employing a solid basalt substrate to investigate the effects of different substrates on the resulting temperature distributions, as well simulations that explore the sensitivity of regolith heating depths to diurnal variations in ambient temperature at the lunar surface. The computed maximum depths in the substrate reached by pertinent isotherms represent the minimum depths of accumulated regolith required to preserve a record of implanted solar particles during the period of regolith exposure. Assessment of temperature distributions produced by simulations including variable thermophysical properties therefore enables more reliable predictions of preservation depths.

2.3 MODEL

2.3.1 *Lava Flow Heat Transfer*

Heat transfer from a lava flow on a body with no atmosphere is governed by radiation to space, conduction to the substrate, internal conduction, advection and viscous dissipation

(if in motion), and latent heat produced during crystallization. To derive temperature distributions as a function of time, these mechanisms are balanced using the conservation of energy. In one dimension, the energy equation is given for a stationary lava flow by

$$\frac{\partial(\rho h)}{\partial t} = \frac{\partial}{\partial z}\left(\frac{k}{c}\frac{\partial h}{\partial z}\right) + S_h \quad , \qquad (1)$$

where r is density, h is enthalpy, t is time, z is depth, k is thermal conductivity, c is specific heat capacity, and S_h represents additional source terms (e.g., the rate of heat generation due to crystallization). This form allows for variable properties ($r(z)$, $k(T)$, and $c(T)$, where T is temperature), but in the case of constant properties the relation $h = cT$ holds and Equation (1) reduces to

$$\frac{\partial T}{\partial t} = \kappa \frac{\partial^2 T}{\partial z^2} \quad , \qquad (2)$$

where k is thermal diffusivity, given by $k = k/rc$, and additional source terms are neglected.

When Equation (1) is applied to a computational domain representing a lava overlying a substrate, different properties may be defined for the lava and substrate materials, but the energy flux due to conduction across the lava–substrate interface must be conserved according to Fourier's Law:

$$k_{lava}\left(\frac{dT}{dz}\right)_{lava} = k_{sub}\left(\frac{dT}{dz}\right)_{sub} , \qquad (3)$$

where subscripts *lava* and *sub* represent lava and substrate, respectively.

The lava upper surface will cool by radiation alone in the vacuum environment of the Moon. Thus a radiative boundary condition is applied to the flow surface, following the Stefan-Boltzmann law

$$q_{rad} = \sigma\varepsilon\left(T_{surf}^4 - T_\infty^4\right) \quad , \qquad (4)$$

where q_{rad} is the radiative heat flux, σ is Stefan-Boltzmann constant, ε is the emissivity of the material, T_{surf} is the temperature of the flow surface, and T_∞ is the far-field temperature of the environment into which the hot surface is radiating. (We adopt T_∞ = 4 K for the Moon, but discuss in section 3.5 the effect of using a higher T_∞). The fourth power dependency and large temperature difference at the surface boundary makes radiation an important heat loss mechanism. The surface of a lava flow will radiate significant amounts of heat until a sufficiently thick crust forms and insulates the interior of the flow, after which the cooling rate is controlled by conduction through the crust.

Once initial and boundary conditions are specified, and appropriate material properties defined, Equation (1) may be solved to derive the temperature distribution in the lava and substrate using the temperature–enthalpy relation $c\partial T/\partial z = \partial h/\partial z$. For our purposes, the source term S_h represents the volumetric rate of energy generation due to latent heat of crystallization (L), which is released at variable rates between the liquidus and solidus temperatures as the different mineral phases crystallize.

2.3.2 *Properties of Lunar Basalt*

The ability of our model to adequately represent lava–substrate heating depends upon use of appropriate material property definitions. Properties of many terrestrial materials are well documented under a wide range of conditions. However, definitions of lunar material properties, especially at high temperatures, are less common. A variety of approaches must be employed to appropriately treat lunar basalt and regolith in a

numerical simulation. The most important properties controlling the cooling of a lava flow are thermal conductivity, specific heat capacity, and latent heat of crystallization [*Fagents et al*., 2010]. For our simulations the lava is assumed to be degassed (i.e., relevant to the distal reaches of a flow), with a constant density of 2980 kg m^{-3}, appropriate to a lunar basalt in a molten state [*Murase and McBirney*, 1973].

Murase and McBirney [1973] measured the thermal conductivity of several igneous compositions in solid and liquid phases. We adopted the expression

$$k_{lava} = -(1.576 \times 10^{-3})\, T + 3.03 \qquad (5)$$

as a simple fit to data measured for a synthetic lunar basalt for temperatures up to 1500 K. Thermal conductivity decreases from 2.7 to 0.67 W m^{-1} K^{-1} as the temperature increases from 200 to 1500 K; above this temperature the trend reverses and conductivity increases with temperature [*Touloukian et al*., 1981; *Čermàk et al.*, 1982; *Büttner et al.*, 1998]. By comparison, *Fagents et al*. [2010] used a constant conductivity of 1.5 W m^{-1} K^{-1}, representing an average value for a synthetic lunar basalt over this temperature range.

The specific heat capacity represents the energy needed to increase the temperature of a given mass of material by a certain amount or, conversely, the energy released when a given mass cools by a certain amount. Measurements of specific heat capacity of lunar basalts at high temperatures are sparse, so data taken from measurements of terrestrial basalts were used to describe the simulated lunar basalt. *Keszthelyi* [1994] gives an expression for specific heat capacity based on laboratory data of *Touloukian et al.* [1989], which shows specific heat increasing from ~ 600 to 1100 J kg^{-1} K^{-1} according to

$$c_{lava} = 1211 - (1.12 \times 10^5 / T). \quad (6)$$

At a transition temperature of 1010 K, the specific heat plateaus at 1100 J kg^{-1} K^{-1}. This transition temperature, known as the Debye or Einstein temperature, represents the high temperature limit of specific heat capacity based on the crystal lattice structure of the material. The relationship in Equation (6) agrees with trends of increasing specific heat capacity with temperature given by *Touloukian et al.* [1981] and *Čermàk et al.* [1982]. For comparison, *Fagents et al*. [2010] used a constant specific heat capacity of 1500 J kg^{-1} K^{-1} based on the data given by *Hemingway et al*. [1973], *Touloukian et al.* [1981], *Lange and Navrotsky* [1992], *Büttner et al*. [1998], and *Williams et al.* [2000], and which accounts for higher values reported in the melting interval.

Fagents et al. [2010] used a simple method to account for latent heat of crystallization *L* [*Carslaw and Jaeger,* 1986], in which the specific heat capacity of the lava is adjusted over the solidification interval ($\Delta T = T_{sol} - T_{liq}$) to an effective specific heat capacity, $c'_{lava} = c_{lava} + L / \Delta T$. For one end member series of simulations, this expression was applied over the entire duration of flow cooling, therefore significantly overestimating both the latent heat produced during crystallization, and the substrate heating depths. For comparison, another end member series of simulations was run with no accounting for latent heat. These two end member simulation series therefore provided upper and lower bounds on substrate heating depths, but did not accurately represent the release of latent heat as the lava crystallizes between liquidus and solidus.

For the present study, we employed MELTS [*Ghiorso et al.*, 1995; *Asimov and Ghiorso,* 1998] and rhyolite-MELTS [*Gualda et al.*, 2012] to determine the range and the distribution of production of latent heat for a selection of mare basalts representing a

range of compositions [*Smales et al.*, 1971; *Willis et al.*, 1972; *Rhodes and Hubbard*, 1973; *Papike et al.*, 1998; electronic appendix of *Wieczorek et al.*, 2006]. Each composition released a total latent heat of 3–4 × 10^5 J kg^{-1} between the liquidus (~1450–1700 K) and solidus (~1200–1450 K) temperatures. In all cases, latent heat release was non-uniform within the crystallization interval. For our current model, we chose lunar sample 12038, a feldspathic basalt [*Keil et al.*, 1971], as a representative composition. It released a total latent heat close to the average of all compositions (3.45 × 10^5 J kg^{-1}) and had a liquidus (1470 K) similar to that of our chosen eruption temperature (1500 K), which thus ensures that our model captured the entire crystallization interval. To determine whether the latent heat release could be approximated as linear in our model, or whether it was better treated as a variable release across the solidification range, we compared the effects of two different crystallization rates. The first,

$$f_{sol} = -3.7736 \times 10^{-3} T + 5.5472 \quad , \qquad (7)$$

where f_{sol} is the fraction of material that has solidified, represents a constant rate of crystallization between liquidus and solidus (Figure 2.2). The second crystallization rate varies across the solidification range as

$$\begin{aligned} f_{sol} &= -3.7244 \times 10^{-5} T^2 + 8.9992 \times 10^{-2} T - 53.367 \ , \quad 1205 < T < 1245 \text{ K} \\ f_{sol} &= -4.6877 \times 10^{-5} T^2 + 0.11737 T - 72.511 \ , \quad 1245 < T < 1394 \text{ K} \\ f_{sol} &= -3.5761 \times 10^{-5} T + 5.2629 \ , \quad 1394 < T < 1470 \text{ K} \end{aligned} \qquad (8)$$

These expressions closely match the crystallization rate derived from MELTS for this composition (Figure 2.2).

Studies have suggested that emissivity of basaltic lava drops as low as 0.55 at very high temperatures [*Abtahi et al.*, 2002; *Burgi et al.*, 2002]. However, it is believed

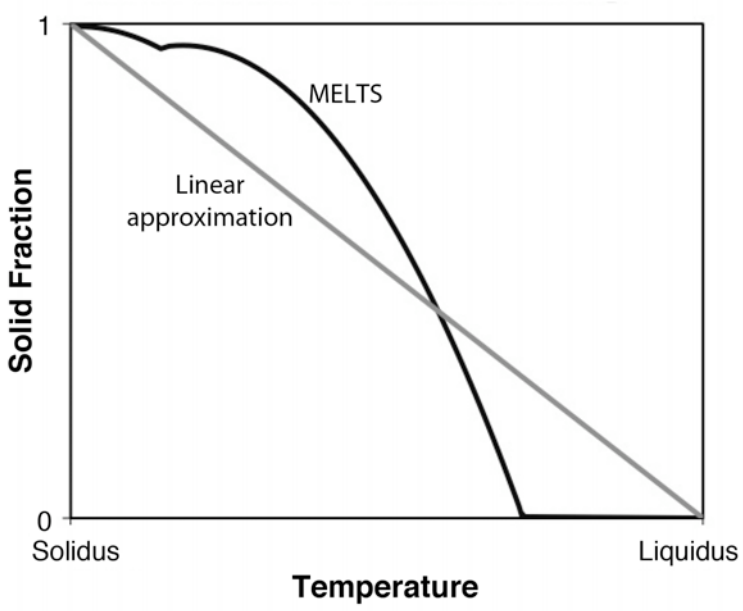

Figure 2.2 Lava solidification with temperature.

Fraction of solidified lava plotted as a function of temperature between liquidus and solidus. Nonlinear solidification (black line) represents crystallization predicted by rhyolite-MELTS [*Ghiorso et al.*, 1995; *Asimov and Ghiorso,* 1998; *Gualda et al.,* 2012]. Linear approximation of solid fraction (grey line) allows for simplification of computational model.

this transition occurs at temperatures well above our model eruption temperature of 1500 K [Ramsey and Lee, 2011; R. Wright, personal communication]. We therefore chose a constant emissivity (ε) of 0.99 [Crisp et al., 1990; Pieri et al., 1990; Flynn et al., 1993; Pinkerton et al., 2002].

2.3.3 *Properties of Lunar Regolith*

The bulk density of the regolith describes the degree of compaction of the particles, such that increased density implies increased grain-to-grain surface contacts and therefore more efficient thermal conduction. *Carrier et al.* [1991] give

$$\rho_{reg} = 1920 \frac{z + 0.122}{z + 0.18} \qquad (9)$$

where r_{reg} is density in kg m^{-3} and z is depth in meters, to describe the increase of regolith density beneath the lunar surface. Density is approximately 1300 kg m^{-3} at the surface, and rapidly approaches a maximum of 1920 kg m^{-3} within about 3 m depth. Equation (12) is valid for present-day regolith thicknesses, but density profiles may have differed for ancient regoliths. However, given that the uppermost few tens of cm of regolith are the most critical for the heat transfer process, we retain the use of Equation (12), since basic gardening processes would be the same for both young and old regoliths.

Published data exist describing the behavior of various regolith thermal properties at temperatures less than 350 K. However, properties have rarely been measured at temperatures greater than 350 K. Thus the temperature dependences of regolith properties must be extrapolated from measured values. *Fountain and West* [1970] found that the thermal conductivity of lunar regolith depends on the density, or compaction, and

the temperature of the sample. They used the relationship

$$k_{reg} = A + BT^3 \quad , \qquad (10)$$

where

$A = (2.019\rho_{reg} - 1.388) \times 10^{-3}$

and

$B = (0.1788\rho_{reg}^3 - 0.1289\rho_{reg}^2 - 0.1856\rho_{reg} + 0.3082) \times 10^{-10}$,

to describe regolith thermal conductivity in a vacuum up to a temperature of 370 K. For this equation, ρ_{reg} must be described in units of g cm^{-3}. The first term, A, in Equation (10) describes solid conduction between points of contact on the surface of regolith grains; the second term, B, represents radiation across pore spaces in the particulate substrate. Assuming that Equation (10) holds at high temperatures, and using Equation (9) to describe regolith density, a minimum thermal conductivity of 1.43 x 10^{-3} W m^{-1} K^{-1} occurs when density and temperature are at minimum values (1330 kg m^{-3} and 200 K, respectively). A maximum thermal conductivity of 0.253 W m^{-1} K^{-1} occurs if density and temperature are at maximum values (1920 kg m^{-3} and 1500 K, respectively), although in practice such high conductivities would never be achieved in our model scenario, because such high temperatures would not propagate to the depths corresponding to a density of 1920 kg m^{-3}. In comparison, *Fagents et al*. [2010] used a constant conductivity of 0.011 W m^{-1} K^{-1}, based on *in situ* heat flow data reported by *Langseth et al*. [1976] and *Vaniman et al.* [1991].

Hemingway et al. [1973] studied several lunar soils and found that

$$c_{reg} = 9.6552 \times 10^{-8} T^4 - 7.3699 \times 10^{-5} T^3 + 1.5009 \times 10^{-2} T^2 + 0.21270T - 23.173 \qquad (11)$$

describes the regolith specific heat to within 10% in the temperature range 90–350

K. Values of c_{reg} increase from ~570 to 850 J kg^{-1} K^{-1} in this range. However, extrapolation of this equation to higher temperatures leads to an unphysical increase in the specific heat. Since specific heat is an intrinsic property, its value is determined by the composition of the material, it is assumed the temperature-dependence of specific heat of the regolith is similar to that of the surrounding mare basalt, the primary source of the mare regolith. Thus, we adopt the form of Equation (6), adjusted to match the value of Equation (11) at 360 K, giving

$$c_{reg} = 1185 - (1.12 \times 10^5 / T) \quad (12)$$

to define regolith specific heat from 360 to 1010 K. We use the basalt transition temperature of 1010 K, where the regolith specific heat will plateau at a value of 1074 J kg^{-1} K^{-1}. For comparison, a constant specific heat of 760 J kg^{-1} K^{-1} was used by *Fagents et al.* [2010] based on the data of *Horai et al.* [1970], *Robie et al.* [1970], and *Hemingway and Robie* [1973].

The temperature of the lunar surface at the time of emplacement of a lava flow will depend on the timing within the lunar day-night cycle (a lunation) and with the latitude of emplacement. *In situ* measurements from a thermocouple buried in the regolith at the Apollo 17 landing site show surface temperature variation from 100 K to nearly 400 K throughout a lunation (29.5 Earth days). Diurnal temperature variations dampen to within a few degrees of ambient in the upper 2 cm of the regolith and are imperceptible at 80 cm depth [*Langseth and Keihm* 1977]. With the exception of semi and permanently shadowed polar regions, latitudinal differences in surface temperature fall within the day/night extremes [*Dalton and Hoffmann* 1972]. To investigate the effects on regolith heating depths of varying surface temperatures, we ran

simulations with initial regolith temperature profiles representative of the extremes of lunar day and night temperatures: a maximum daytime temperature of 400 K and a minimum nighttime temperature of 100 K. For both day and night simulations, initial regolith temperatures were set to converge to 200 K at ~ 80 cm depth.

2.3.4 *Model Description*

Numerical simulations were performed using PHOENICS (*Parabolic Hyperbolic Or Elliptic Numerical Integration Code Series*), a computational fluid dynamics software program designed to simulate fluid flow, heat transfer, and chemical reaction processes (http://www.cham.co.uk). PHOENICS allows significant user freedom in the customization of simulations. Through a simple graphical interface, users can create models with unique geometries and material properties. For more complex simulations, for example those involving temperature-dependent properties, the user can supply algebraic expressions to define characteristics specific to a model. We have previously used PHOENICS to model a variety of thermal and fluid dynamic problems [e.g., *Fagents and Greeley*, 2001; *Fagents et al*., 2000; 2010], and testing of the models against standard analytical solutions has demonstrated that our PHOENICS simulations have the requisite accuracy.

In this study, we used a one-dimensional formulation to simulate a stationary lava flow at an initial temperature of 1500 K emplaced instantaneously on substrate material at ambient temperature (Figure 2.3). For our sensitivity tests, the flow thickness was set to 1 m to reduce computational time, although this thickness is consistent with meter-scale lobes identified at some locations on the Moon [e.g., Hadley Rille; *Vaniman et*

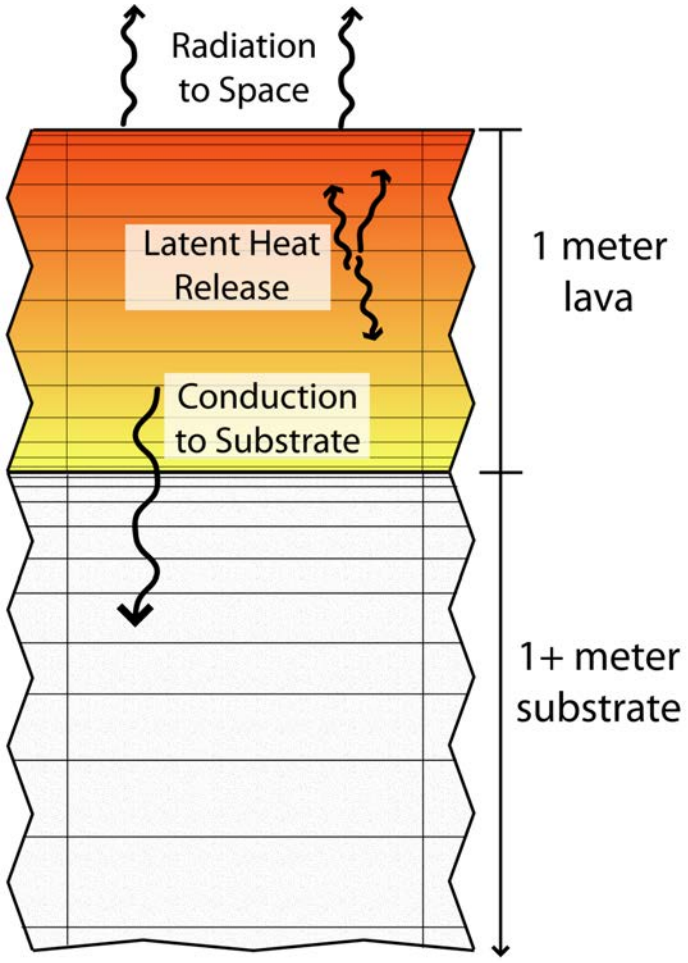

Figure 2.3 Illustration of computational grid.

Schematic illustration of computational grid used in PHOENICS. A 1 m thick lava flow initially at 1500 K is instantaneously emplaced on a 200 K substrate measuring 1 to 15 m deep, depending on material and heating conditions. Lava domain contains 60 vertical cells, substrate domain contains 60 to 240 cells, with finer cell sizes near boundaries. Heat is lost from the lava flow through radiation to space environment and conduction to the substrate. Heat is released as latent heat of crystallization in cooling lava.

al., 1991]. For most runs, excluding those exploring diurnal temperature variations, the initial regolith temperature was set to 200 K, an average of global surface temperatures [*Vaniman et al.*, 1991]. The computational grid contained 60 cells in the lava and 60 to 180 cells in the substrate, depending on modeled substrate thickness (1–15 m). The temperature of the lower boundary of the computational domain (i.e., the bottom of the substrate) was free to vary. However, the depth of the substrate was chosen so that the heat pulse never reached the lower boundary in our simulations. Cell size was refined toward the lava surface and lava–substrate boundary to ensure model accuracy in zones of large temperature gradients. Simulations were run with a 30-minute time-step. A range of cell dimensions and time-step sizes were explored to ensure optimal stability and convergence of the solution. The results were monitored to find the maximum depths of the 300, 500, and 700 °C (573, 773, and 973 K) isotherms representing the temperatures at which specific extralunar particles will begin to volatilize (Table 2.1).

2.4 RESULTS

2.4.1 *Temperature-Dependent Thermal Conductivity*

When lava conductivity, k_{lava}, varies inversely with temperature as in Equation (5), the lower conductivity at high temperatures allows the core of the lava to remain near eruption temperature for a longer duration relative to the simulations employing a constant lava conductivity (Figure 2.4 a,b). In contrast, as the lava surface cools radiatively to space, the conductivity of the lava increases, resulting in greater heat

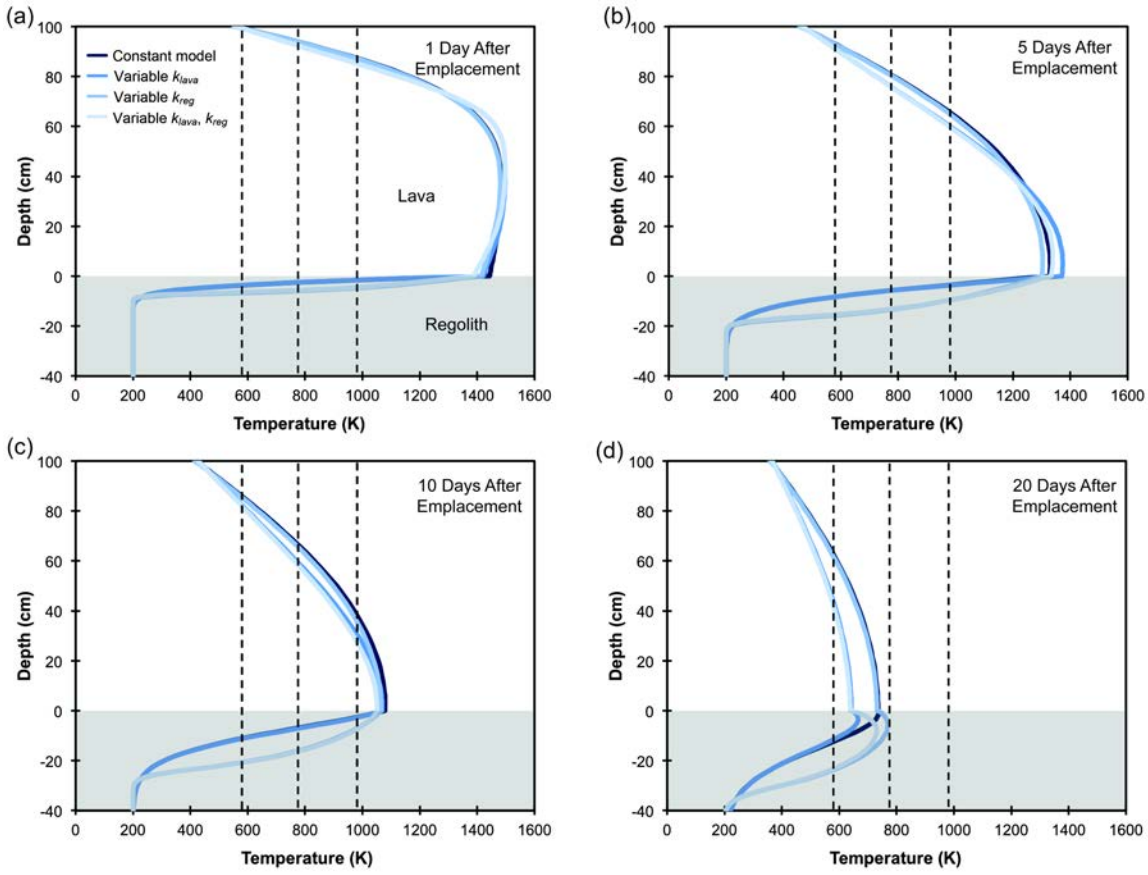

Figure 2.4 Temperature profiles with varying thermal conductivity definitions.

Temperature profiles through lava and regolith at (a) 1 day, (b) 5 days, (c) 10 days, and (d) 20 days after emplacement of 1 m thick lava flow, showing the influence of different thermal conductivity definitions. Initial lava and regolith temperatures are 1500 K and 200 K, respectively. Curves represent, from darkest to lightest, lava and regolith thermal conductivities both constant, lava conductivity variable with temperature, regolith conductivity variable with temperature, and both lava and regolith conductivity variable with temperature. Vertical dashed lines indicate temperatures at which specific particles will begin to volatilize (Table 2.1).

transfer with decreasing temperature; therefore temperatures within a few tens of centimeters of the flow surface decrease at a higher rate than for the constant lava conductivity case (Figure 2.4b). As the flow continues to cool throughout, lava thermal conductivity increases, and temperatures drop more rapidly (Figure 2.4 c,d). Overall, lava temperatures drop to near ambient more quickly than in the constant case. However, the initial retention of heat in the lava core and the increased thermal conductivity at the lava regolith interface cause more heat to be conducted into the regolith (Figure 2.4d), resulting in modest increases in the maximum penetration depths of the 773 and 973 K isotherms by 8% and 3%, respectively, over the constant-value case. The 573 K isotherm has a 2% shallower maximum depth than in the constant case due to the greater overall cooling rate of the lava.

While the effects of temperature-dependent lava thermal conductivity are quite subtle, accounting for the temperature and density dependences of regolith thermal conductivity (k_{reg}; Equation 10) has a marked effect on the amount of heat conducted from the lava into the regolith. At high temperatures, such as near the lava–regolith interface immediately after emplacement, the effect of the high temperature dominates the effect of the low density. Thus, the increased conductivity of the regolith allows for greater heat transfer than in the constant-value simulation. At shallow depths, the regolith is heated to higher temperatures than in the constant case (Figure 2.4 a,b). In contrast, at low temperatures (i.e., deeper in the substrate), the conductivity drops to values lower than in the constant case, even given the greater regolith density at depth, leading to insulation against the heat pulse as it propagates downward. As the lava cools, the regolith also becomes less conductive near the less dense lava–regolith interface,

Table 2.2 Maximum penetration depth and timing of key volatile penetration.

	Temperature					
	573 K (300˚C)		773 K (500˚C)		973 K (700˚C)	
Model Version	z_{max} **(cm)**	t_{max} **(day)**	z_{max} **(cm)**	t_{max} **(day)**	z_{max} **(cm)**	t_{max} **(day)**
All constant properties	12.8	18	7.0	10	3.7	6
Variable k_{lava} only	12.6	16	7.2	10	3.9	7
Variable k_{reg} only	23.9	21	16.2	11	10.0	6
Variable k_{lava} and k_{reg}	23.5	19	16.4	10	10.5	7
Variable c_{lava} only	11.0	14	5.8	7	3.0	5
Variable c_{reg} only	9.9	17	5.4	10	2.8	6
Variable c_{lava} and c_{reg}	8.5	14	4.5	8	2.3	5
Variable r_{reg}	13.3	17	7.3	14	3.9	6
Latent heat included, constant properties	15.3	23	8.9	14	5.0	11
All variable properties, no latent heat	17.9	14	12.6	8	8.0	5
All variable properties, latent heat included	*20.4*	*20*	*15.1*	*12*	*10.4*	*10*
Basalt substrate, variable properties, latent heat included	25.4	6	0.3	2	--	--

allowing the available heat to remain within the substrate and to continue propagating downward in the regolith layer (Figure 2.4c,d). A bulge in the temperature profile appears within the regolith (Figure 2.4d), as the temperature in the regolith is warmer than in the lava. The increased heat within the regolith leads to greater penetration depths for all isotherms than in the constant-value case, increasing the maximum depths of the 573, 773, and 973 K isotherms by factors of 1.9, 2.3, and 2.8 respectively (Table 2.2).

When both lava and regolith conductivities vary with temperature, the lava conductivity controls the lava–regolith interface temperature, but isotherm depths within the substrate are dominated by the effects of the regolith conductivity, reaching approximately the same depths as the case in which the regolith conductivity was varied alone (Figure 2.4 c,d). The effects of the inverse relationship between lava temperature and conductivity are seen in the prominence of the bulge in Figure 2.4d, as the regolith remains warmer than the rapidly cooling lava flow. With respect to the constant-value case, the 573, 773 and 973 K isotherm depths increase by factors of 1.8, 2.4, and 2.9, respectively (Table 2.2).

2.4.2 *Temperature-Dependent Specific Heat Capacity*

The inclusion of a temperature-dependent lava specific heat capacity (c_{lava}; Equation 6) results in a lower specific heat at all temperatures than the constant-value case, but particularly at low temperatures. Lower specific heat implies less energy available within the lava, such that the entire flow cools more quickly than in the constant-value case (Figure 2.5). The increased cooling rate and the decrease in the available energy result in less heat being transferred into the regolith, leading to shallower maximum

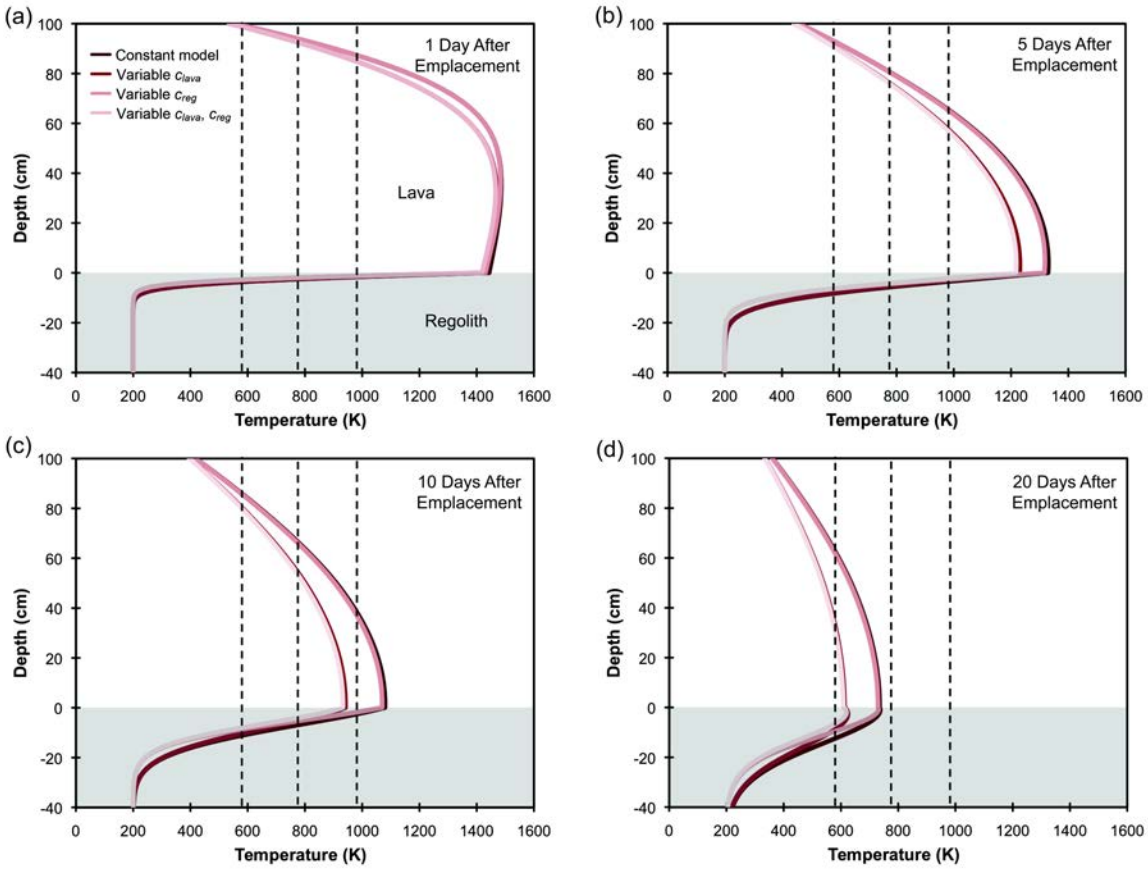

Figure 2.5 Temperature profiles with varying specific heat capacity definitions.

Temperature profiles through lava and regolith at (a) 1 day, (b) 5 days, (c) 10 days, and (d) 20 days after emplacement of 1 m thick lava flow, showing the influence of different specific heat capacity definitions. Initial lava and regolith temperatures are 1500 K and 200 K, respectively. Curves represent, from darkest to lightest, lava and regolith specific heat capacities both constant, lava specific heat variable with temperature, regolith specific heat variable with temperature, and both lava and regolith specific heat variable with temperature. Vertical dashed lines indicate temperatures at which specific particles will begin to volatilize (Table 2.1).

depths of all isotherms than in the case in which a constant lava specific heat was adopted; the 573 K, 773 K, and 973 K isotherms reach shallower maximum depths by 14%, 16%, and 17%, respectively (factors of ~0.83–0.86).

At temperatures within 100 K above ambient, the temperature-dependent specific heat capacity of the regolith (c_{reg}; Equation 12) is less than the constant value adopted for comparison (760 J kg^{-1} K^{-1}). Above this threshold, the specific heat increases to a maximum of 1074 J kg^{-1} K^{-1} at 1100 K. With a larger specific heat capacity, more energy is required to increase the temperature of the regolith, leading to shallower depths of heating and a small decrease in the temperature at the base of the lava flow (Figure 2.5). Each of the pertinent isotherms has a 23–24% shallower maximum depth (i.e., a factor of ~0.77) than for the constant-value model (Table 2.2). When both the lava and the regolith specific heat vary with temperature, the decreased total heat within the lava compounds the effects of increased regolith heat capacity, further reducing the maximum depths reached by each of the isotherms to 34–37% shallower (i.e., factors of 0.66–0.63) than in the constant case.

2.4.3 *Latent Heat of Crystallization*

Including latent heat release in our simulation has a substantial effect on the total heat available in the system. However, the use of expressions for variable (Equation 8) vs. linear (Equation 7) crystallization rates produced negligible differences in isotherm penetration depths. This implies that it is the total latent heat released over the cooling interval, and not the specific release pattern, that influences the maximum heating depths. Regardless of the equation used, as the lava cools and crystallizes through the

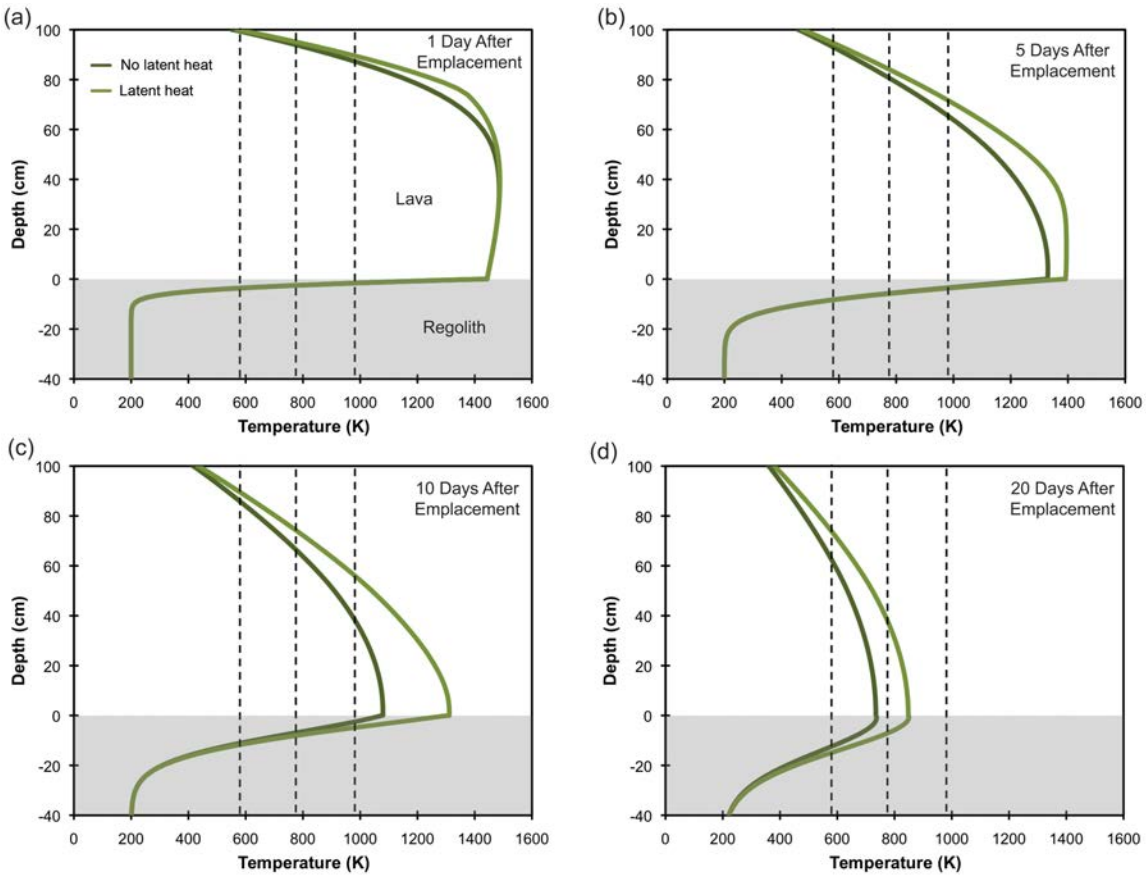

Figure 2.6 Temperature profiles with and without latent heat release.

Temperature profiles through lava and regolith at (a) 1 day, (b) 5 days, (c) 10 days, and (d) 20 days after emplacement of 1 m thick lava flow, showing the influence of latent heat release included (light line) following Equation (7), compared to no latent heat release (dark line). Initial lava and regolith temperatures are 1500 K and 200 K, respectively. Vertical dashed lines indicate temperatures at which specific particles will begin to volatilize (Table 2.1).

solidification interval, the release of latent heat slows the cooling rate of the lava (Figure 2.6). This is apparent soon after emplacement, where radiative cooling from the upper surface leads to crystallization and release of latent heat in the upper portion of the flow (Figure2.6a), maintaining warm temperatures for a longer duration than in the case where latent heat is not supplied. As the effects of surface cooling propagate downward in the lava and the core crystallizes, the latent heat maintains higher temperatures throughout the lava for a longer duration than if latent heat is not included in the model (Figure 2.6 b,c,d). The delayed lava cooling prolongs the duration of heat transfer to the regolith, thereby increasing the amount of heat introduced into the substrate, and producing deeper penetration of the heat pulse (Figure 2.6d). The maximum depths of the 573, 773, and 973 isotherms increase by 19%, 28%, and 38% (factors of 1.2, 1.3, and 1.4), respectively, over the constant-value model (Table 2.2).

Upon emplacement, a portion of the upper and lower surfaces (e.g., crusts) of the flow may cool sufficiently rapidly to quench to glass, thereby reducing the latent heat of crystallization released by the system. To account for this reduction, we ran a comparison model in which total latent heat released was reduced to 75% of the maximum amount of latent heat available within the lava, representing a lava with 25% quenching, which is likely a significant overestimation [*Keszthelyi and Denlinger*, 1996], and hence provides an extreme estimate of the effects of quenching. However, we find that, with 75% crystallization of the lava flow the maximum depths of the 573, 773, and 973 K isotherms decrease by only 4%, 5%, and 6%, respectively, from the maximum depths reached when the entire flow crystallized. This effect will be further reduced for a thicker lava flow, when the proportion of quenched crust will be less. Given that significantly reducing the

latent heat release has only a minor effect on substrate heating, we have chosen to include 100% release of latent heat in order to fully represent the potential influence of solidification on the thermal budget of the lava–substrate system.

2.4.4 *Regolith Density*

The increase in regolith bulk density from ~1300 kg m^{-3} at the surface to ~1920 kg m^{-3} at depths exceeding 3 m (Equation 9; *Carrier et al.*, 1991) has the potential to affect substrate heating in two ways: (i) by changing the bulk thermal diffusivity of the regolith ($k_{reg} = k_{reg}/r\,c_{reg}$), and (ii) by increasing the grain to grain contact areas, thus modifying regolith thermal conductivity (Equation 10). Regarding mechanism (i), we find that inclusion of the depth dependence in the simulations has little effect on the heating of the regolith, increasing the maximum depths of the 573, 773 and 973 K isotherms by less than 1 cm (3%, 5% and 8%, respectively) (Table 2.2). Similarly, compaction of the surficial regolith by the weight of the overlying lava flow is unlikely to change the isotherm penetrations depths significantly.

Effect (ii), on the other hand, is harder to constrain. However, *Wechsler et al.* (1972) show that, while both the solid conduction component (A in Equation 10) and the radiative coefficient (B in Equation 10) both increase with increasing bulk density, radiative effects become a much greater influence on thermal conductivity as temperatures increase above ambient because of the T^3 dependence. Therefore the relatively modest effect of the increase in regolith density is swamped by the dependence of thermal conductivity on temperature. We include the density effect in our calculations solely based on its importance in Equation (10).

2.4.5 *Diurnal Surface Temperature Variations*

We find that varying the initial regolith temperature profile due to diurnal fluctuations produces negligible effects on regolith heating depths. Temperature differences of 100 K or more are only present in the top 1–2 cm of the regolith. This small region of temperature gradient is trivial compared to the energy introduced to the system by the overlying lava flow, emplaced at 1500 K. Adopting a nighttime profile with a regolith surface temperature of 100 K at the time of flow emplacement produces maximum depths of the 573, 773 and 973 K isotherms that are decreased by only ~0.1 cm (~1%) each. A daytime temperature profile with an initial regolith surface temperature of 400 K yields an increase in maximum depths of less than 0.5 cm (3%, 4%, and 5%, respectively).

An additional effect of the diurnal temperature cycle is that, during the lunar day, solar irradiance on the surface of the lava will increase the effective ambient temperature to which it is radiating. We ran a comparison simulation using an effective ambient temperature of 250 K for T_∞ in Equation (4), following *Keszthelyi* [1995], to investigate the resulting effect on the lava–substrate system. We find that, because of the $T_{surf}^4 - T_\infty^4$ form of the radiative heat flux, the initially high lava surface temperatures overwhelmingly dominate the heat flux, regardless of the value of T_∞. Therefore, the specification of T_∞ proves to be an insignificant factor in maximum penetration depths of the heat pulse. The change in surface temperature using T_∞. = 4 K vs. 250 K does not affect the system until the surface of the lava cools to ~ 500 K, about 10 days after emplacement. At this time, the surface temperatures of the two cases (T_∞ = 4 K and 250

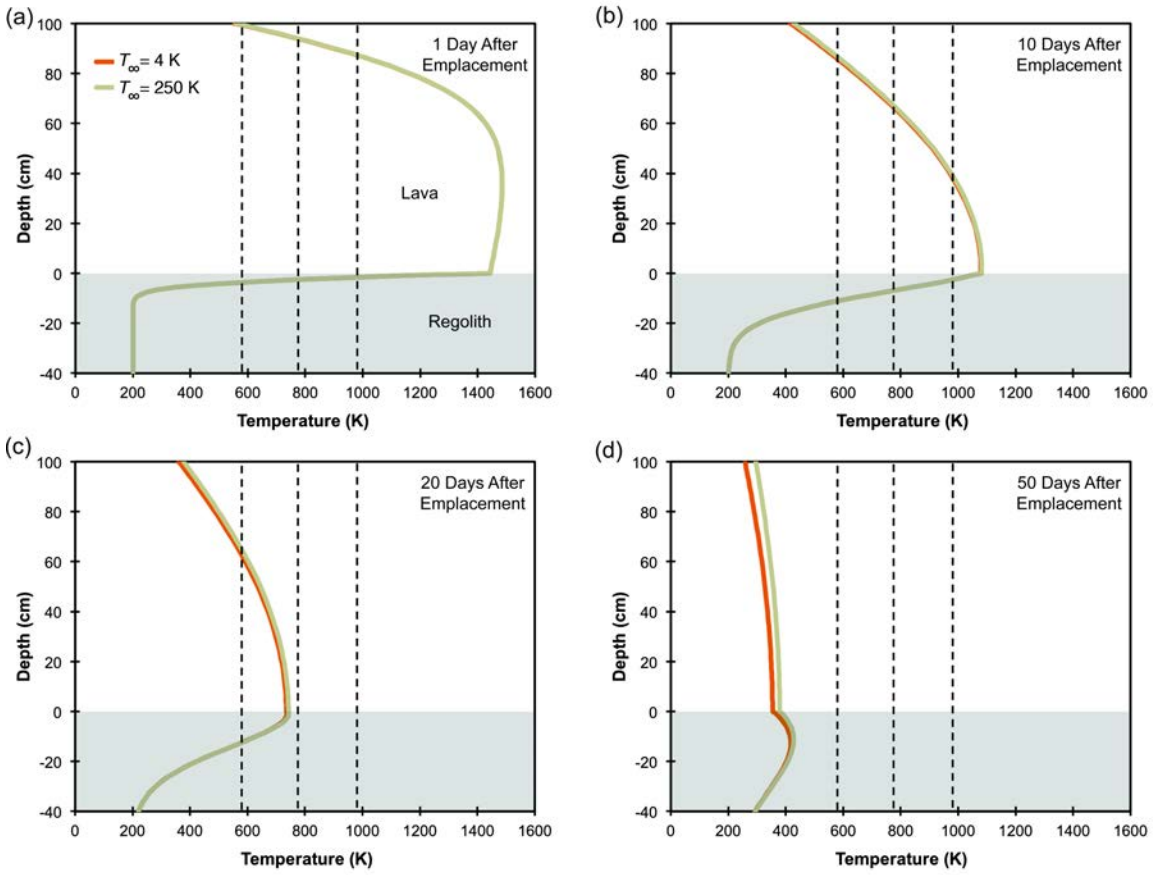

Figure 2.7 Temperature profiles with varying ambient temperature.

Temperature profiles through lava and regolith at (a) 1 day, (b) 10 days, (c) 20 days, and (d) 50 days after emplacement of 1 m thick lava flow, with all thermophysical parameters held constant. Orange line represents an ambient temperature (T_∞) of 4 K. Tan line represents effective ambient temperature of 250 K. Initial lava and regolith temperatures are 1500 K and 200 K, respectively. Vertical dashed lines indicate temperatures at which specific particles will begin to volatilize (Table 2.1).

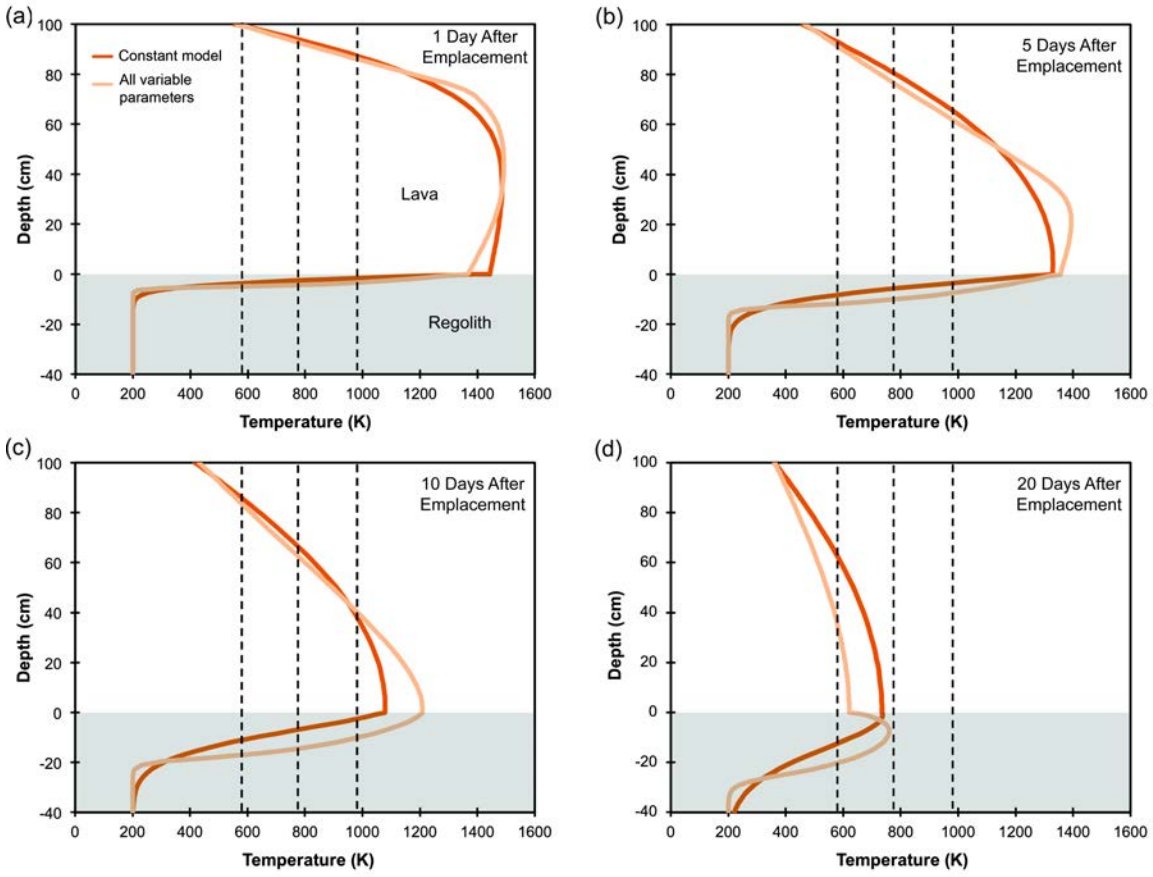

Figure 2.8 Comparison of models with constant and variable properties.

Temperature profiles through lava and regolith at (a) 1 day, (b) 5 days, (c) 10 days, and (d) 20 days after emplacement of 1 m thick lava flow, with all thermophysical parameters held constant (dark line) and with variable lava thermal conductivity, specific heat capacity, and latent heat and variable regolith thermal conductivity, specific heat capacity, and density (light line). Initial lava and regolith temperatures are 1500 K and 200 K, respectively. Vertical dashed lines indicate temperatures at which specific particles will begin to volatilize (Table 2.1).

K) will deviate; however, this deviation does not reach the substrate until well after the heat pulse has reached maximum depths in the regolith and therefore does not affect our results (Figure 2.7).

2.4.6 *Comparison of Full Model to Constant-Property Model*

When all variable thermophysical parameters are included in the simulation there is a significant difference in the cooling behavior of the system compared to the simulation with constant parameters (Figure 2.8). Initially, the lower specific heat of the lava allows surface radiation to more rapidly cool the upper portion of the lava flow (Figure 2.8 a,b). This cooling does not propagate to the center of the flow, as the release of latent heat and low thermal conductivity in the core act to maintain high temperatures. The increased thermal conductivity of the regolith at high temperatures transmits heat downward from the base of the flow leading to higher temperatures in the shallow regolith (Figure 2.8 b,c). As the lava cools below the solidus (~ 1200 K) and latent heat is no longer released, the lava conductivity increases, and lava specific heat decreases. These effects compound to cool the lava more quickly than in the constant-property case (Figure 2.8d). Temperatures remain elevated in the regolith; as the top of the regolith cools, thermal conductivity decreases, creating a buffer against the warmer regolith at depth and producing a bulge in the temperature profile (Figure 2.8d). The maximum depths of the 573, 773 and 973 K isotherms are factors of 1.6, 2.2, and 2.9, respectively, deeper than for the constant-property case (Table 2.2).

2.4.7 *Results for Solid vs. Particulate Substrates*

The variable-property model was modified to incorporate a solid basalt substrate of the same composition as the overlying lava, such that the substrate has a greater thermal conductivity, specific heat capacity, and density than if it were composed of regolith. Figure 2.9 shows a comparison of temperature profiles in regolith and solid basalt substrates. It can be seen that the differing substrate properties have a marked effect. The greater conductivity of the basalt substrate allows heat to be transported rapidly away from the lava–substrate interface to greater depths in the substrate. In addition, the greater specific heat capacity implies that the thermal energy delivered from the lava to the interface is unable to raise the substrate temperature to the same degree as would be the case for a regolith substrate. The sum effect of these two parameters is that solid substrate temperatures are in general elevated above ambient to lesser degrees, but to greater depths, than when the substrate consists of regolith (Figure 2.9). The regolith substrate is heated to higher temperatures but the overall extent of heating is confined to shallow depths. However, only the 573 K isotherm penetrates to greater depths in solid basalt than in regolith (by 10%); the 773 K isotherm penetrates just a few mm, and no portion of the substrate exceeds 973 K (Table 2.2).

2.4.8 *Influence of Lava Flow Thickness*

To assess the influence on regolith heating of lava flow thickness, we ran simulations of 10 m lava flows with variable thermophysical properties for comparison with the 1 m case. *Fagents et al.* (2010) showed that, when constant properties are used, the depth of heating scales with lava flow thickness, i.e., isotherms beneath a 10 m thick lava flow

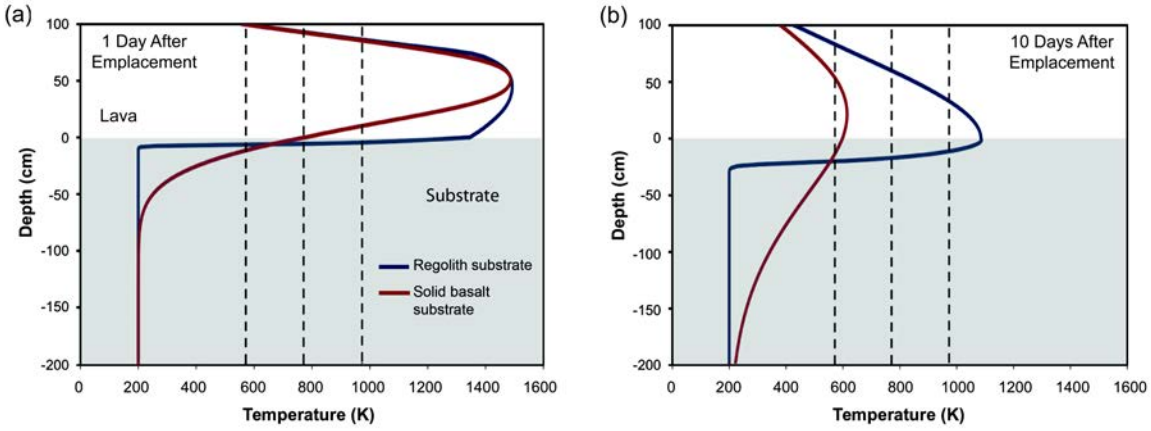

Figure 2.9 Temperature profiles with varying substrate materials.

Temperature profiles through lava and regolith at (a) 1 day and (b) 10 days for solid basalt (purple) and regolith (orange) substrates. Both cases include variable thermophysical properties and latent heat release. Initial lava and regolith temperatures are 1500 K and 200 K, respectively. Vertical dashed lines indicate temperatures at which specific particles will begin to volatilize (Table 2.1).

would penetrate 10 times deeper than those beneath a 1 m thick lava flow. When latent heat release and temperature-dependent properties are included in the 10 m simulations, the maximum depths of the 573, 773, and 973 K isotherms are only 9.5, 9.1, and 8.4 times the equivalent 1 m simulations. Thus, isotherm penetration depths scale close to but not quite linearly with flow thickness, as for the constant-property case. This can be attributed to the significant nonlinearities introduced into the model by incorporating variable thermophysical properties.

2.5 DISCUSSION

2.5.1 *Importance of Variable Material Properties*

The inclusion of temperature-dependent material properties is critical for adequately treating lava–substrate heat transfer, and for the accurate assessment of the depths to which exogenous particles will be lost from the lunar regolith. Penetration of the key volatilization isotherms (Table 2.1) depends in a complex way on the variation with temperature of thermal conductivity, specific heat capacity, and the release of latent heat due to crystallization (Figure 2.10). Simulations including variable properties, as described by Equations (5)–(12), predict that implanted solar wind ions will be disturbed and/or lost to depths 1.6 times greater than for the case in which all model parameters are kept constant (Table 2.2).

In general, temperature-dependent thermal conductivity and specific heat capacity have competing influences on the temperature distribution in the regolith (Figure 2.10). However, the regolith thermal conductivity is the greatest single influence on heating

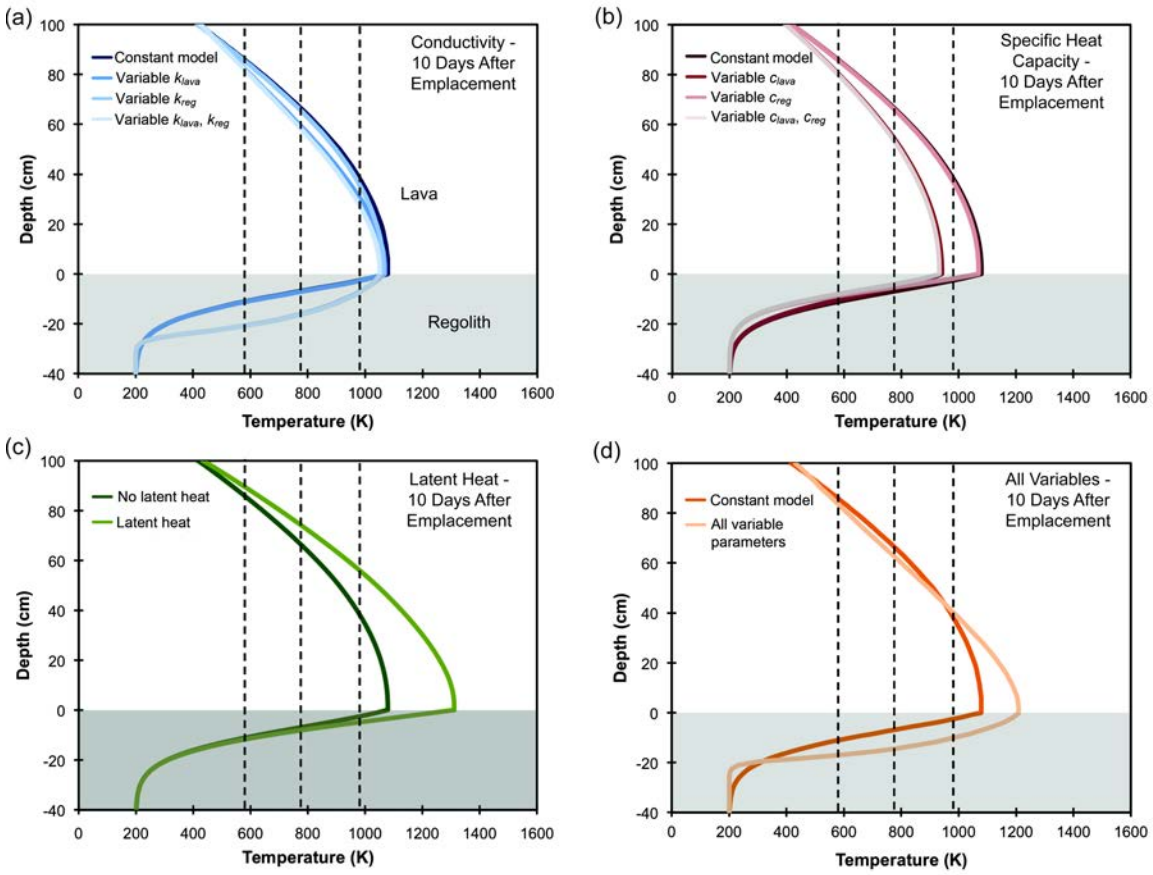

Figure 2.10 Summary of results at 10 days after emplacement.

Temperature profiles with depth at 10 days after emplacement of 1 m thick lava flow for (a) variations of thermal conductivities, (b) variations of specific heat capacities, (c) variations of latent heat release, and (d) comparison of constant parameter model and variable parameter model. Initial lava and regolith temperatures are 1500 K and 200 K, respectively. Vertical dashed lines indicate temperatures at which specific particles will begin to volatilize (Table 2.1).

depths, especially when one considers the effect of the T^3 dependence (expressing radiative heat transfer across intergranular voids; Equation 10) over the temperature range of interest (200–1500 K). At the contact with the lava, the high initial conductivity induced in the regolith allows for efficient transfer of heat into the substrate; then as the lava and the upper portion of the regolith cool, and regolith conductivity drops, it acts as an insulator, isolating the heat pulse in the regolith and allowing it to penetrate to greater depths. (Figure 2.4d and Figure 2.8d). Our results concur with those of *Fagents and Greeley* [2001], who found that the influence of regolith properties (particularly thermal conductivity) was greater than the influence of lava properties in determining regolith temperatures at depth.

To adequately model the thermal budget of a solidifying lava flow, it is necessary to include treatment of latent heat due to crystallization. As described in section 2.2, the predecessor [*Fagents et al*., 2010] to our current model did not specifically treat latent heat release, but adopted two end member sets of constant lava properties in an attempt to place upper and lower limits on the expected range of heating depths. Simulations using the first set of properties, the constant-value results cited in this paper (Table 2.2), predicted maximum depths of 12.8, 7.0, and 3.7 cm for the 573, 773, and 973 K isotherms, respectively. The other end member simulation approximated latent heat release by modifying the lava specific heat capacity, but applying it over the entire cooling duration. The resulting isotherm depths of 28, 14, and 7.8 cm are therefore significantly overestimated. In the current model, with latent heat treated explicitly and released exclusively between the liquidus and solidus, maximum isotherm depths of 15.3, 8.9 and 5.0 cm are predicted when all other properties are held constant (Table 2.2).

These results fall predictably between those of the end member simulations of *Fagents et al.* [2010]; however, they are closer to those that did not account for latent heat in any way. Incorrect treatment of latent heat can therefore have a considerable effect on cooling simulations. Table 2.2 shows that maximum isotherm penetration depth increases by 28% (from 17.9 to 23 cm) when latent heat is included in the variable-property simulations.

We found no significant difference in the heating depths predicted by simulations in which latent heat was distributed uniformly (Equation 7), compared to those in which latent heat was released non-uniformly (Equation 8), based on the crystallization pattern predicted by MELTS for a representative lunar basalt composition. In contrast, other studies have emphasized the importance of including nonuniform latent heat distributions [*Lange et al.*, 1994; *Patrick et al.*, 2004]. Based on our results, we argue that the need to incorporate nonuniform vs. uniform latent heat release in a given lava flow thermal model will depend on the purpose of the model and the specific scenario being treated. Because we are interested in finding maximum isotherm depths after a significant period of heat transfer, the exact details of the temperature distribution on the shorter time scale of solidification are not relevant. Depending on the nature of the problem under investigation, we recommend that a range of latent heat distributions be explored to optimize the trade off between accuracy and computational efficiency.

2.5.2 *Specification of Substrate Material*

Our simulations produce significant differences in temperature profiles within a lava–substrate system when that substrate consists of solid basalt rather than particulate

regolith. While the solid basalt scenario is not directly relevant to the search for paleoregoliths containing solar wind particles, the model results for different substrate types imply a need to specify the substrate material in models of terrestrial lava emplacement and cooling. The low thermal conductivity of particulate materials means that they insulate the base of the flow, allowing the lava core to retain heat for significantly longer than for solid substrates, thereby enhancing flow mobility. These effects will not be as extreme under terrestrial conditions because gas conduction by air in regolith pore spaces contributes a significant component to the effective conductivity of a particulate material [e.g., *Wechsler and Glaser*, 1965]. Nevertheless, the effective conductivity will generally be less than that of a solid substrate. During effusive eruptions on Earth, it is common for lava to flow over material other than solid basalt. For example, at Kīlauea and Mauna Loa Volcanoes, Hawai‘i, there are many locations where lava has been emplaced on top of basaltic or reef-derived sand, soil, or explosive basaltic deposits (e.g., pyroclastic fragments). This range of compositions, water and organic contents, grain size, etc., may have a significant influence on lava–substrate heat transfer, flow mobility, and hence the length and areal coverage of the flow. It is prudent, therefore, to consider specification of a substrate material to treat conductive cooling from the flow base in models of lava flow emplacement and hazard prediction.

2.5.3 *Limitations of Model*

We have conducted a study of the sensitivity of our model of lava–substrate heat transfer to the incorporation of variable thermophysical properties, and have shown that they have important influences on lunar regolith heating. However, by opting to treat an

instantaneously-emplaced, stationary lava flow, we have not addressed the period of emplacement of the flow, which could significantly enhance substrate heating because of the additional heat advected by the moving lava, thus increasing the regolith depths required to retain implanted volatiles. Our choice not to treat the lava flow emplacement phase is in part based on an incomplete understanding of lunar lava flow emplacement mechanisms. Lunar flow units are areally extensive and produce individual lobes on the order of meters to tens of meters thick [e.g., *Gifford and El-Baz*, 1981; *Wilhelms*, 1987; *Vaniman et al.*, 1991; *Hiesinger et al.,* 2002; *Hiesinger and Head*, 2006; *Robinson et al.*, 2012]. However, the long interval that has elapsed since volcanism was prevalent on the Moon means that flow morphologies and textures have become difficult to discern. It is therefore hard to determine the style(s) of emplacement of lunar mare lavas. While it is accepted that they are typically of large volume and low viscosity [e.g., *Murase and McBirney*, 1970; *Taylor et al*., 1991], it remains unclear whether they were emplaced as high effusion rate, turbulent sheet flows, or rather more modest, inflationary (pāhoehoe-like) compound flow fields, or even perhaps some combination of the two mechanisms. Regardless of emplacement style, our model results are most relevant to the distal margins of flow lobes that would have had limited period of flow before coming to rest and solidifying; these areas would also be the most favorable for retrieving regolith samples.

The results of our simulations are only as good as the underlying assumptions and information provided to the model in the form of the definitions of thermophysical properties. The model exhibits a particular sensitivity to the characterization of substrate thermal conductivity. Thermal conductivity of particulate materials varies in a complex

way with temperature, particle size (and size distribution), bulk density (porosity), packing, composition, and the presence and pressure of any interstitial gas phase [e.g., *Presley and Christensen,* 1997a]. Past studies have investigated limited ranges of conductivity dependence for particulate materials [*Cremers et al.*, 1970; *Fountain and West*, 1970; *Wechsler et al.,* 1972; *Langseth et al.,* 1976; *Presley and Christensen,* 1997a,b; *Huetter et al.,* 2008; *Yuan and Kleinhenz,* 2011], and data sets produced by different methods have different degrees of accuracy and reliability [*Presley and Christensen*, 1997a]. For example, experimental data are commonly derived for packed glass beads of uniform size, and over very limited temperature ranges. This makes it particularly difficult to define a generally applicable conductivity function for the lunar regolith, given that regolith is a complex mixture whose physical properties (e.g., particle components and size distribution, porosity, etc.) will naturally vary from site to site [*Carrier et al.*, 1991]. Furthermore, while there are theoretical approaches to understanding thermal conductivity of particulate materials [e.g., *Schotte*, 1960; *Watson*, 1964; *Wechsler et al.,* 1972; *Blumberg and Schlünder*, 1995], a thorough validation with physical data for natural particulate mixtures is lacking, particularly at the elevated temperatures relevant to our model scenario. The model's sensitivity to substrate thermal conductivity means that, while we have attempted to define a realistic temperature-dependent conductivity based on theory, it is unclear whether this approach adequately treats natural particulate mixtures over all ranges of conditions. The validity of this treatment therefore requires further exploration, and would benefit from additional theoretical and experimental investigations, as well as physical validation. Nevertheless, we have established a robust methodology for modeling variable properties, and this is

amenable to modification as better conductivity treatments are developed.

2.5.4 *Implications for Lunar Exploration*

The majority of charged particles that impact the lunar surface are ions emitted by the Sun, primarily hydrogen, but also helium and small amounts of carbon, nitrogen, oxygen and heavier elements [*Haskin and Warren,* 1991; *McKay et al*., 1991; *Vaniman et al.,* 1991]. Because of their relatively low energies, these are usually implanted to depths of microns to millimeters within mineral grains [*Haskin and Warren*, 1991]. High-energy particles from more distant sources (e.g., GCRs) penetrate to meter-scale depths in solid material, producing a cascade of nuclear reactions and leaving linear tracks of crystal damage in the target rock [*McKay et al*., 1991; *Vaniman et al.,* 1991; *Goswami*, 2001; *Eugster,* 2003; *Lucey et al.,* 2006]; molecules of CO, CO_2, H_2O, and N_2 are commonly created when the kinetic energy of the incoming particles is greater than the energy of reaction. Because of their greater penetration depths, the absence or presence of a regolith is not critical to the preservation of the GCR products. Thus, penetration into, and heating of, solid basalt (either a pristine surface or underlying a regolith veneer) is perhaps more relevant to preservation of GCR records. The relatively restricted depth of the high-temperature domain within a solid basalt substrate (Figure 2.9) implies that GCR records would have remained undisturbed by the emplacement of the overlying flow without the need for an insulating regolith to assist preservation. Isolation of the particle tracks and daughter nuclei to individual flows within a vertical succession would allow dating of the GCR record in successive flows, thereby significantly improving the time resolution of GCR records.

In the case of implanted solar wind materials and surviving fragments of hydrous-mineral bearing projectiles [e.g., *Zolensky*, 1996], the simulations presented in this contribution determines the depths to which 1–10 m thick lava flows will heat the underlying regolith to temperatures at which volatiles may be released. These depths represent the minimum thickness of regolith deposit needed for the particles to survive heating by a lava flow. When constant material properties are used in the model, a minimum of 12.8 cm of regolith (maximum heating depth of the 573 K isotherm) is needed to preserve a complete record of all implanted volatiles beneath a flow lobe 1 m thick. When temperature-dependent properties are included, at least a 20.4 cm thickness is needed for complete preservation. Simulations of 10 m thick lava flows show that maximum isotherm depths do not scale linearly with the thickness of the overlying flow; rather the relative depth of heat pulse penetration decreases; a thickness of 194 cm is required, rather than 204 cm based on scaling up from the 1 m simulations.

During the peak period of lunar mare volcanism, regolith is thought to have developed on fresh surfaces at a rate of 5 mm/Ma [*Hörz et al.*, 1991] and may have reached 20 mm/Ma prior to 4 Ga [*Crozaz et al.*, 1970; *Duraud et al.*, 1975], although these production rates depend critically on our understanding of small impact crater formation [*McEwen et al.,* 2005]. At such rates, it would take tens to hundreds of millions of years to accumulate enough regolith to preserve a complete record of extralunar volatiles beneath 1 m thick lavas. The thicknesses of lunar lava flows vary considerably, leading to a wide range in minimum regolith depths required to preserve exogenous materials, and hence time intervals required for sufficient regolith to develop. Our model can provide estimates of the range of depths within a regolith that must be sampled to

extract a pristine suite of implanted volatiles, based on the thickness of the overlying flow. These depths can provide estimates of the interval that must elapse between successive flow field emplacement.

Hiesinger et al. [2000, 2002, 2003] used Clementine multispectral imagery of several lunar maria to map boundaries between flow fields and to estimate emplacement ages. Intervals of over a billion years between emplacement of successive flow fields were found in most of the maria studied. In Oceanus Procellarum, a total age range of ~ 2.7 Ga was found, and adjacent and overlapping flows commonly exhibit several hundred Ma between emplacement. The age gaps between successive flow fields are sufficiently large that individual flow units would have developed significant regolith cover [*Hiesinger et al.,* 2000, 2002, 2003]. Clementine multispectral data were also used to define the thicknesses of spectrally distinct flow units excavated by small impact craters [*Kramer,* 2010; *Weider et al*., 2010]. More recently, high-resolution image data acquired by the Lunar Reconnaissance Orbiter Camera [LROC; *Robinson et al.,* 2010] have revealed details of lava flow characteristics that were previously undetectable with lower-resolution data. Features such as impact craters, pit craters, and layered boulders exhibit tens of stratified units, on the order of 1 to 10 m in thickness, that are interpreted to be lava flow successions [e.g., *Zanetti et al.,* 2011; *Ashley et al.*, 2012; *Robinson et al.*, 2012]. Although buried regoliths have not been directly observed in the image data, the LROC observations of thin, layered flow units and Clementine-based assessment of mare flow field ages imply that subsurface paleoregoliths should be present in the lunar maria. This may have been confirmed by the Lunar Radar Sounder instrument on Kaguya, which appears to have detected buried regolith layers [*Ono et al.*, 2009]. As the new

remote sensing data sets allow refinement of lava flow thicknesses, flow unit ages, and potentially, regolith layer thicknesses, our model will allow determination of the preservation potential of implanted volatiles at given sites within the lunar mare. These assessments can therefore be used to make recommendations for sites of future manned exploration of the lunar surface. As outlined by *Crawford et al.* [2007], locating and sampling buried paleoregolith deposits would be greatly facilitated in the context of future human "sortie-class" missions to the lunar surface. These missions would preferably have the capacity for surface mobility of tens to hundreds of kilometers to reach proposed sample sites, and drilling to depths of at least tens of meters to obtain a useful succession of paleoregolith deposits and lava units. Sample analysis *in situ* or upon return to Earth could potentially yield valuable new information on, for example, the temporal variability in composition and strength of the solar wind and the changing galactic environment of the Solar System.

2.6 CONCLUSIONS

The inclusion of temperature-dependent material properties is a crucial element in simulations describing the physics of cooling lava flows, as demonstrated by our comparisons of simulations of lava–substrate heat transfer using both constant and variable thermophysical properties. In our simulations, the use of temperature-dependent properties implies that solar wind volatiles would be disturbed at depths in the regolith that are 60% greater than the case in which constant properties are used. This increase in depth is driven by the inclusion of latent heat of crystallization, and by the effects of a

substrate thermal conductivity that is elevated at temperatures near eruption temperatures, and then decreases as the regolith cools to ambient conditions.

Substrate properties, particularly thermal conductivity, most strongly control the depth of penetration of key volatile-release isotherms into the substrate. This is especially marked for regolith materials, because of the T^3 dependence of thermal conductivity due to radiation across the pore spaces within packed particulates. However, in addition to temperature, thermal conductivity is sensitive to many variables, including particle size, compaction, pore size, and the presence of any interstitial gas; any future modeling would therefore benefit from theoretical and experimental work that would lead to a more thorough characterization of thermal conductivity of regolith materials, particularly at elevated temperatures.

The lunar regolith potentially holds important information about the history of our Solar System [*NRC*, 2007]. Solar wind particles, cosmic ray products, and other exogenous materials (e.g., debris from planets, asteroids and comets) have great potential for advancing our understanding of the history of the Solar System, including that of the early Earth. Retrieving regolith deposits that have been protected from contemporary bombardment by overlying lava flows could be a key activity during future missions to the Moon. The work presented here provides the basis for identifying sites where such records might be preserved, which could, therefore, be targeted by future exploration activities.

2.7 NOTATION

A, B	Empirical constants in Eq. (10) (W m^{-1} K^{-1}, W m^{-1} K^{-4})
c, c_{lava}, c_{reg}	Specific heat capacity, of lava, of regolith (J kg^{-1} K^{-1})
c'_{lava}	Effective specific heat capacity of lava (J kg^{-1} K^{-1})
f_{sol}	Fraction of crystallized lava (-)
h	Enthalpy (J kg^{-1})
k, k_{lava}, k_{reg}, k_{sub}	Thermal conductivity, of lava, of regolith, of substrate (W m^{-1} K^{-1})
l	Length (m)
L	Latent heat of crystallization (J kg^{-1})
q_{rad}	Radiative heat flux (W m^{-2})
S_h	Source term in energy equation (W m^{-3})
t	Time (s)
T	Temperature (K)
T_∞	Radiative far-field temperature (~4 K)
T_{amb}	Ambient temperature of lunar surface (200 K)
T_{liq}	Lava liquidus temperature (K)
T_{sol}	Lava solidus temperature (K)
T_{surf}	Temperature at the lava flow surface (K)
z	Depth (m)
ε	Emissivity of lava (0.99 -)
κ	Thermal diffusivity (m^2 s^{-1})
r, r_{reg}	Density, regolith density (kg m^{-3})
σ	Stefan-Boltzmann constant (5.7×10^{-8} W m^{-2} K^{-4})

2.8 ACKNOWLEDGEMENTS

This paper greatly benefitted from comments by C. Dundas, M. Wieczorek, and an anonymous reviewer. This work was funded in part by the NASA Lunar Advanced Science and Exploration Research Program Grant NNX08AY75G. Financial support for M.E.R through the NSF Graduate Research Fellowship Program. This is HIGP Publication 2002, SOEST Publication 8874, and LPI publication 1722.

CHAPTER 3.

EXPERIMENTAL MEASUREMENTS OF LAVA–SUBSTRATE HEAT TRANSFER

3.1 ABSTRACT

The direct heating of a particulate substrate by molten basalt was measured in a laboratory setting to verify a numerical model of lava–regolith heat transfer. Molten basalt from Kīlauea Volcano, Hawai‘i was poured directly onto lunar regolith simulant GSC-1 and temperatures were monitored as the system cooled. The experimental results provide an upper limit on the depths to which ancient implanted exogenous particles would have been destroyed in lunar paleoregoliths overlain by lava flows, thereby constraining the depths from which pristine samples could be retrieved during future lunar exploration. When heated by an ~8–10 cm thick melt layer, the regolith simulant was heated to 300 ˚C to depths between 5.6 and 7.2 cm. Heat transfer in a particulate substrate will be less efficient in the vacuum environment on the Moon than on Earth, suggesting that volatiles buried in lunar paleoregoliths will have a higher preservation potential, given similar flow thicknesses and initial temperatures. A second objective of the experiments was to examine the temperature-dependence of the thermal conductivity of lunar regolith simulant GSC-1. Thermal models rely critically on adequate description of thermophysical properties, and thermal conductivity is poorly known for particulate materials at high temperatures. Through numerical simulations, we determined the effective thermal conductivity of GSC-1 to increase linearly from 0.35–0.45 to 0.6–0.8 W m^{-1} K^{-1} between 23 and 1227 ˚C, and verified that the model appropriately treats the system physics.

3.2 INTRODUCTION

The motivation for this work lies in developing a quantitative understanding of lava–substrate heat transfer under a range of planetary conditions. For example, on the Moon, ancient basaltic flows likely overlie paleoregolith deposits containing records of implanted exogenous particles such as the solar wind and cosmic rays [*Wieler et al*., 1996; *NRC*, 2007]. These particles hold clues to the history of the early Solar System that are not preserved on Earth because the atmosphere and magnetosphere block surface interactions with many exogenous particles, and plate tectonic recycling of the crust erases ancient records. Exogenous particles could be extracted from buried paleoregolith deposits during future manned missions to the lunar surface [*Spudis,* 1996; *Armstrong et al*., 2002; *Crawford et al.*, 2008; *Ozima et al.*, 2008], provided adequate constraints are provided on sampling locations and depths. A protective lava flow would shield the regolith deposit from continued bombardment and supply solid rock for isotopic dating to constrain the age of the underlying paleoregolith [*McKay et al*., 1989; *Spudis*, 1996; *McKay*, 2009; *Spudis and Taylor*, 2009]. Multiple intercalated layers of lava and paleoregolith would therefore provide a time-series of the implanted particles, providing information on their variability with time. However, in addition to offering protection from continued bombardment, a lava flow will also heat the underlying regolith and volatilize the implanted volatiles to some finite depth in the regolith beneath the flow [*Crawford et al*., 2007, 2008, 2010]. *Fagents et al.* [2010] and *Rumpf et al.* [2013] developed a numerical model to determine the conditions under which regolith volatiles would be preserved, and noted the strong dependence of the resulting temperature distribution on the substrate thermal conductivity. In particular, the low thermal conductivity of the particulate regolith acts to restrict elevated temperatures to relatively

shallow layers in the substrate, in comparison with a solid substrate material. However, it is crucial to establish the validity of the physics used in the simulations, in order to make accurate assessments of volatile preservation depths. In particular, the use of extrapolations of thermal conductivity treatments for particulate materials (i.e., lunar regolith) to very high temperatures merits close examination because of scarcity of empirical data under such conditions.

In this study, we use experimental measurements to constrain the effective thermal conductivity of GSC-1, a lunar regolith simulant, and to attain a better understanding of lava–substrate thermal interactions. We begin by describing a series of experiments in which basalt from Kīlauea Volcano, Hawai‘i was melted and poured into experimental devices filled with GSC-1. Thermocouples monitored internal temperatures of both the melt and regolith simulant, while an infrared thermographic camera monitored external temperatures. System temperatures were analyzed to establish heating and cooling behavior and to identify the effects of latent heat within the system. Temperatures at the melt–simulant boundary and within the simulant were used to establish numerical simulations to derive the temperature-dependent effective thermal conductivity of the regolith simulant. Effective thermal conductivities of particulate materials will be lower on the Moon than on Earth because the contribution of gas movement will be minor, lowering rates of heat transfer into a regolith substrate. Therefore the maximum penetration depths of isotherms representing the minimum temperatures needed to volatilize key exogenous particles (summarized in Table 3.1) in the experiments were determined to further understanding of the preservation potential of exogenous particles on the Moon.

Table 3.1 Volatilization temperatures in lunar regolith

Species	Minimum Volatilization Temperature
H_2, He	300 °C (573 K)
CH_4, Ne, Ar	500 °C (773 K)
CO, CO_2, N_2, Xe	700 °C (973 K)

From *Simoneit et al*. [1973]

3.3 BACKGROUND

The thermal conductivity of particulate materials is not well defined, particularly at high temperatures. *Fountain and West* [1970] measured the thermal conductivity, k_{reg}, of a tholeiitic terrestrial basalt with a composition similar to returned lunar regolith samples. The basalt was crushed and sieved to 37–62 microns to simulate the grain size of the upper few centimeters of the of lunar regolith. Experiments were performed under vacuum conditions at temperatures up to 97 ˚C (370 K), finding that thermal conductivity varies with temperature and density, or compaction of the particulate material, as

$$k_{reg} = A + BT^3 \tag{1}$$

where

$$A = (2.019\rho_{reg} - 1.388) \times 10^{-3}$$

and

$$B = (0.1788\rho^3_{reg} - 0.1289\,\rho^2_{reg} - 0.1856\,\rho_{reg} + 0.3082)\times 10^{-10}$$

T is temperature, and ρ_{reg} is the density of the regolith (in g cm^{-3}) (Figure 3.1). The first

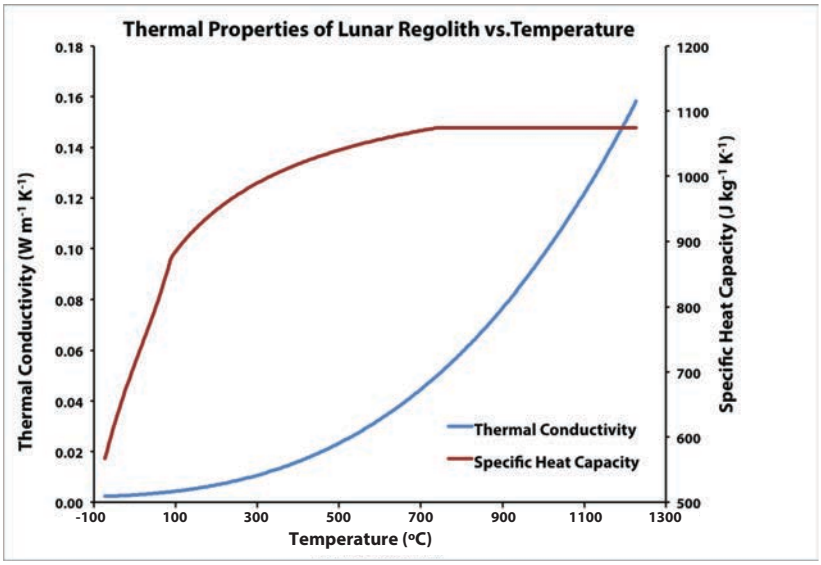

Figure 3.1 Regolith properties versus temperature.

Lunar regolith thermal conductivity versus temperature (blue line, left axis), extrapolated from *Fountain and West* [1970], and regolith specific heat capacity versus temperature (red line, right axis) adapted from *Hemingway et al.* [1973] and *Touloukian et al.* [1989]. Regolith conductivity relationship describes conductivity via grain-to-grain contacts and due to radiation across void spaces. The specific heat capacity definition is also used in numerical simulations in this study.

term in Equation (1) describes the solid conduction between grains in the material; the second term describes conduction due to radiation across interstitial pour spaces. Theoretically, this equation should hold at lava eruptions temperatures (>1100 °C) [*Patankar*, 1980], however it has not been empirically verified. *Botterill et al.* [1989a] measured the effective thermal conductivities of packed beds of alumina with a mean particle size of 376 μm (range, 150 – 743 μm) and of silica particles with mean particle sizes of 410 μm (range, 150 – 853 μm) and 590 μm (range, 353 – 1040 μm). Each sample was heated to ~ 900 ˚C under atmospheric conditions and temperatures monitored as they cooled. Effective thermal conductivities were found to rise linearly with temperature. The effective thermal conductivity of the alumina particulate was found to increase from ~ 0.4 ± 0.03 W m^{-1} K^{-1} near 400 ˚C to ~ 0.76 ± 0.03 W m^{-1} K^{-1} near 975 ˚C. The effective conductivity of the 410 μm silica increased between 0.32 and 0.66 ± 0.05 W m^{-1} K^{-1} over ~ 350 to 880 ˚C, and increased between 0.35 and 0.87 ± 0.05 W m^{-1} K^{-1} over ~ 380 to 930 ˚C for the 590 μm silica. They attribute the increase in effective thermal conductivity with temperature entirely to the effects of radiative heat transfer [*Botterill et al.*, 1989b].

Heat flow measurements made on the lunar surface during the Apollo missions found regolith thermal conductivities ranging between 0.011 and 0.0295 W m^{-1} K^{-1} (± 15% uncertainty), varying by the depth and bulk density of the regolith, at temperatures at or below 100 °C [*Langseth et al*., 1976; *Vaniman et al.*, 1991, and references therein]. Recently, *Grott et al.* [2010] refined the methods used to derive thermal conductivity from Apollo heat flow experiments, finding values that range from 0.0146 ± 0.0022 to 0.0264 ± 0.0040 W m^{-1} K^{-1} at lunar surface temperatures.

For our purposes, we seek to constrain the effective thermal conductivity, k_e, of

regolith simulant GSC-1, given by

$$k_e = k_c + k_r + k_g \quad (2)$$

which combines the effects of particulate thermal conductivity via solid conduction within individual grains and across grain-to-grain contacts, k_c, radiation across pore spaces, k_r, and conduction by interstitial gas within the system, k_g [*Woodside and Messmer*, 1961]. k_c and k_r are represented as terms A and B, respectively, in Equation (1).

Woodside and Messmer [1961] found that effective thermal conductivity of particulate materials varies according to the kinetic theory of gasses, which states that gas conductivity, k_g, can be described by

$$k_g = D\rho_g c_g v\lambda \,, \quad (3)$$

where D is a material-dependent constant, ρ_g is the density of the gas, c_g is the heat capacity of the gas, v is the mean molecular velocity, and λ is the mean free path of the gas. *Keszthelyi* [1994] and *Huetter et al.* [2008] define effective thermal conductivity as the sum of solid phase conductivity, radiation across void spaces, and convection of interstitial gases. However, pore spaces within simulant are much less than the ~ 1 cm limit needed for significant convection found by [*Keszthelyi*, 1994], rendering convection insignificant in our case. Movement of volatiles as heated interstitial gases expand and lightly bonded gases volatilize within the substrate can be accounted for as an increase in molecular velocity in Equation (3). Many experiments measuring the heat transfer in lunar regoliths and lunar regolith simulants are performed under vacuum condition and do not account for any contribution due to gas conduction.

Because of the inherent difficulties of working with molten lava in the field or laboratory, there have been relatively few controlled studies of lava flow heat

transfer problems at natural scales. *Keszthelyi* [1995] measured lava–substrate interface temperatures at active flows at Kīlauea Volcano by leaving thermocouples in the paths of oncoming pāhoehoe flows. Interface temperatures increased rapidly at contact, then plateaued until heating resumed 2 to 4 minutes after emplacement. A second phase of heating, beginning 2 – 4 minutes after lava emplacement, was inferred to be the expression of latent heat released during the crystallization of microlites in the basalt.

Lev et al. [2012] and *Edwards et al.* [2013] performed a series of large-scale lava pour experiments involving the melting of 70 – 450 kg of basalt. *Lev et al.* [2012] used video analysis to study flow dynamics and constrain flow rheology. In experiments by *Edwards et al.* [2013], melt was poured over substrates of ice or snow layered with sand to simulate lava–ice interaction observed on Earth and inferred on Mars. Measurements of substrate temperatures indicate delayed heating of underlying ice layer when buffered by a layer of sand directly below the advancing melt. Delayed heating is attributed to the high porosity of the sand and creation of an insulating boundary layer of the sand. Delayed heating of the substrate was also observed as energy was needed to vaporize water . Examination of oxygen and hydrogen isotopes in the glassy walls of lava bubbles formed during experiments indicated they were formed from the escape of vapor derived from the underlying ice layer, not from expansion of volatiles exsolved from the basalt [*Edwards et al.*, 2013]. The experimental investigation discussed in the present contribution is therefore the first to examine the details of lava thermal interactions with a particulate substrate, with the goal of establishing a robust numerical model for application to terrestrial and planetary environments.

3.4 METHODS

3.4.1 *Experimental Methods*

We performed a series of experiments to investigate the heating of regolith simulant by an overlying layer of molten basalt. Figure 3.2 shows our experimental set-up. For each experiment, a container having dimensions of 20 × 20 × 25 cm was constructed from 1-inch thick calcium silicate sheeting, using high-temperature ceramic adhesive. The container was filled with a 15-cm layer of lunar regolith simulant and fitted with an array of eight 1/16-inch K-type thermocouples. The regolith simulant, GSC-1, was milled from a Jurassic diabase, quarried from Leesburg, VA, and is composed of approximately 45% anorthosite and 45% clinopyroxene with minor opaques, quartz, and biotite [*Taylor et al.*, 2008]. The source rock was chosen as a lunar regolith simulant because it is similar to most mare basalts in bulk mineralogy, holocrystalline texture, dearth of hydrated minerals (biotite content, 2%), and diallage pyroxene structure [*Taylor et al.*, 2008]. The simulant was sieved to <1 mm, dried at 110 ˚C for 24–48 hours, and allowed to cool for at least 12 hours. The cooled, dried simulant was then packed into the experimental container, to a density of ~1600 kg m^{-3}, and dried at 110 ˚C for a further 24–48 hours before it was allowed to cool to ambient temperature in an airtight container. This procedure was designed to avoid resorption of atmospheric water vapor into the simulant prior to the experiment.

Basalt used in this experiment was collected from the glassy surfaces of the 2011 pāhoehoe flows fed from the Puʻu ʻŌʻō-Kūpaianaha eruption, Episode 58, at Kīlauea Volcano, Hawaiʻi. Lava was erupted in early 2011 and collected in April 2011 and May

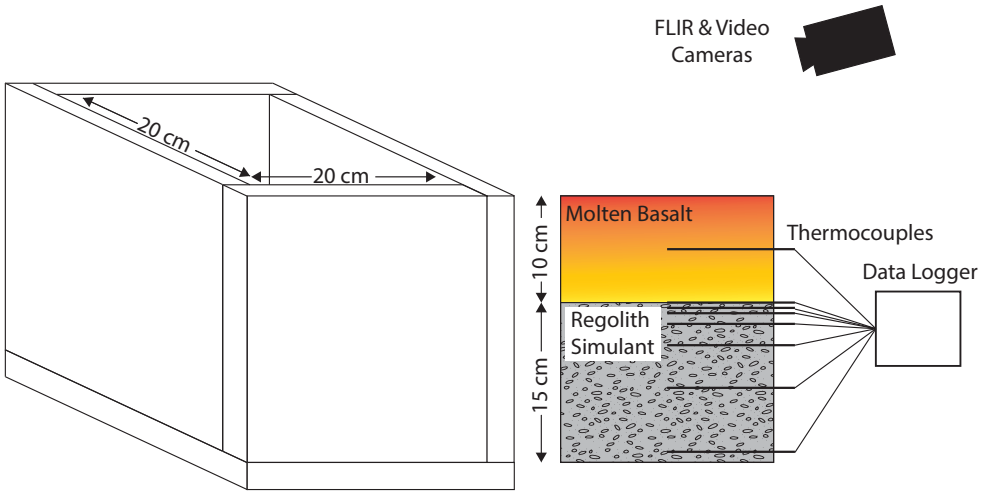

Figure 3.2 Schematic diagram of experimental set-up.

Schematic diagram of experimental set-up. Experimental containers were built using 1 inch thick calcium silicate sheeting. Internal dimensions measure 20 × 20 × 25 cm. The container was packed with lunar regolith simulant (GSC-1) to a depth of 15 cm and bulk density of ~1600 kg m^{-3}. Thermocouples were embedded within simulant at depths of 0, 0.5, 1, 2, 4, 8, and 14 cm-depth from the top of the simulant. The upper 10 cm of the container was filled with molten Kīlauea basalt and monitored with an additional thermocouple in the core of the melt, and with video and infrared thermographic cameras.

2012. For each experiment, approximately 10 kg of basalt was crushed and placed in a silicon carbide crucible and heated in a gas forge to a temperature ≥ 1100 ˚C. When the basalt was fully melted, the crucible was removed from the forge and basalt was poured onto the regolith simulant to a depth of ~8–10 cm within the container (Figure 3.3). The system was allowed to cool for ~24 hours, until ambient temperature was reached. The experiment was monitored by thermocouple data loggers (Omega® HH147U), an infrared thermographic camera (FLIR® SC620), and a high-definition video camera (Canon® VIXIA HF200). The results from three experiments are discussed below. The thermocouples sampled at 1 Hz. Depending on the pour, he infrared camera sampled between 1 and 10 Hz during the first hour of the experiment and between 0.01 and 1 Hz for the remainder of the experiment.

3.4.2 *Numerical Methods*

To assess the ability of our numerical model to adequately represent the physics of the thermal problem under consideration, we performed simulations of the experiments, using PHOENICS®, a computational fluid dynamics software program (www.cham.co.uk), which has previously been used to simulate a range of thermal and fluid dynamic problems [*Fagents and Greeley*, 2001; *Fagents et al.,* 2000, 2010; *Rumpf et al.*, 2013]. In this study, we focus on conductive heat transfer in the regolith simulant, with the objective of constraining the temperature-dependence of thermal conductivity. To do this, our model formulation neglects the thermal gradients within the melted basalt, and takes the temperature data captured by the thermocouple at the melt–simulant interface as the upper boundary condition on the regolith simulant to calculate

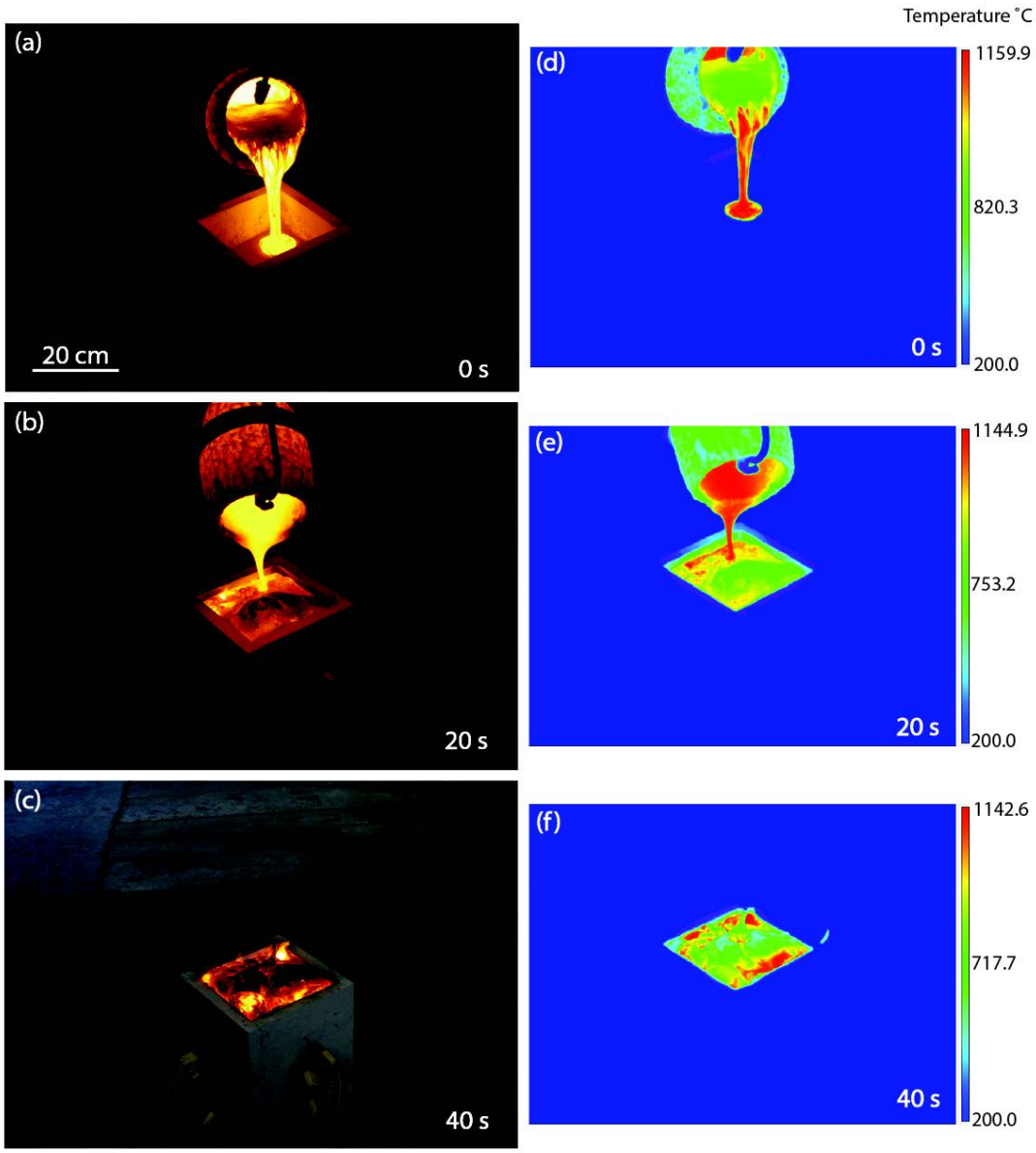

Figure 3.3 Photographs and thermal stills from Pour 6.

Photographs and infrared thermographic video stills from Pour 6 at (a) and (d) $t = 0$ s, (b) and (e) $t = 20$ s, and (c) and (f) $t = 40$ s. Temperatures in the thermal images are in represented in ˚C on the color scale bar.

the time evolution of the temperature distribution within the simulant.

A one-dimensional unsteady heat conduction equation forms the basis of the numerical simulations of experimental melt pours. The computational grid, representing the 15-cm depth of regolith simulant, contained 30 vertical cells, with finer cell size near the upper boundary to adequately resolve the thermal evolution in zones of high temperature gradients. Simulations were run with a 15 s time step; cell size and time step were optimized to ensure stability and convergence.

A temperature-dependent definition of specific heat capacity, c_{reg}, was used for the regolith simulant, as discussed in *Rumpf et al.* [2013] (Figure 3.1). *Hemingway et al.* [1973], who performed heating experiments on lunar soils at low temperatures, found that,

$$c_{reg} = 9.6552\times10^{-8}T^4 - 7.3699\times10^{-5}T^3 + 1.5009\times10^{-2}T^2 + 0.21270T - 23.173 \qquad \text{-183} < T \leq 87\ ^{\circ}\text{C}. \qquad (4)$$

Above 87 ˚C, c_{reg} rises unphysically when calculated by equation (4) and cannot be extrapolated to higher temperatures. As heat capacity is an intrinsic property, its value is determined by the composition of the material. Here, it can be approximated using the heat capacity for basalt, the dominant source material for mare regolith. Therefore, we adapt a regolith heat capacity,

$$c_{reg} = 1185 - (1.12\times10^5/T) \qquad 87 < T \leq 827\ ^{\circ}\text{C} \qquad (5)$$

from measurements of terrestrial basalts by *Touloukian et al.* [1989], adjusted to match the value of Equation (3) at 87 ˚C. The specific heat plateaus to 1074 J kg^{-1} K^{-1} at a Debye transition temperature of 827 ˚C. This transition temperature represents the high

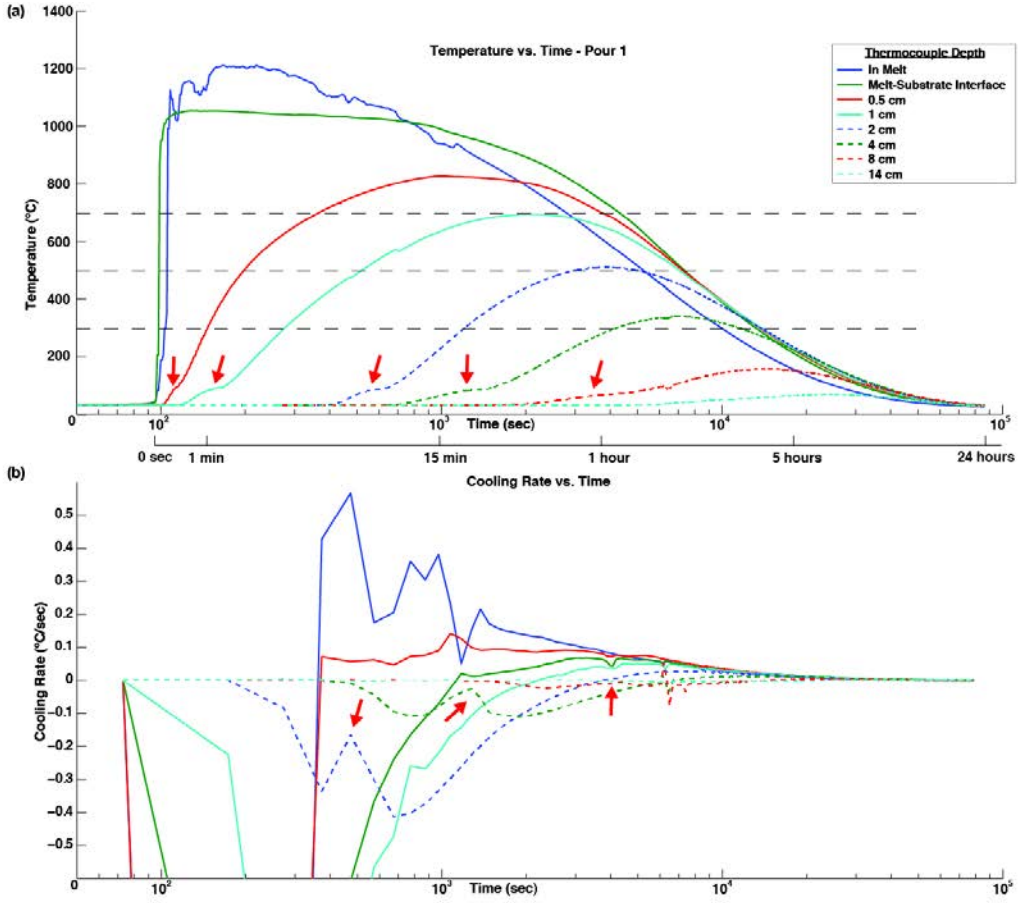

Figure 3.4 Temperature data from Pour 1.

Temperature data from Pour 1. (a) Temperatures as a function of time measured by each thermocouple. (b) Cooling rates measured by thermocouples in °C s^{-1} averaged over 100 s intervals and plotted against time. Negative cooling rates indicate heating at a given location. The top two thermocouples were located in the melt core and at the melt–simulant interface, respectively. Other thermocouples were located at the depths in the simulant indicated in the legend. Red arrows indicate effects of water vaporization from simulant.

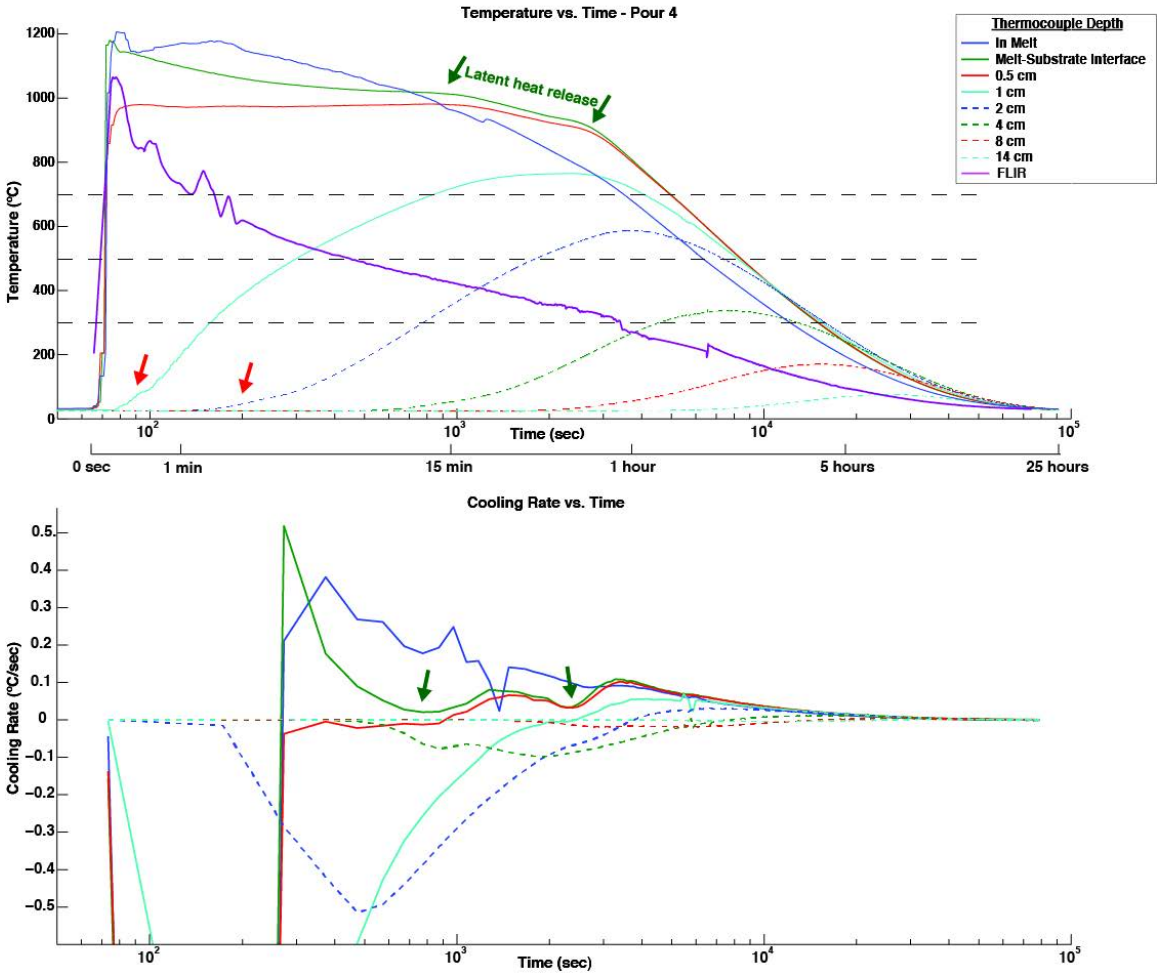

Figure 3.5 Temperature data from Pour 4.

Temperature data from Pour 4. (a) Temperatures as a function of time measured by each thermocouple and by the infrared thermographic camera at the center of the lava surface. (b) Cooling rates measured by thermocouples in ˚C s^{-1} averaged over 100 s intervals and plotted against time. Negative cooling rates indicate heating at a given location. The top two thermocouples were located in the melt core and at the melt–simulant interface, respectively. Other thermocouples were located at the depths in the simulant indicated in the legend. Green arrows indicate effects of inferred latent heat release due to crystallization of microlites. Red arrows indicate effects of water vaporization from simulant.

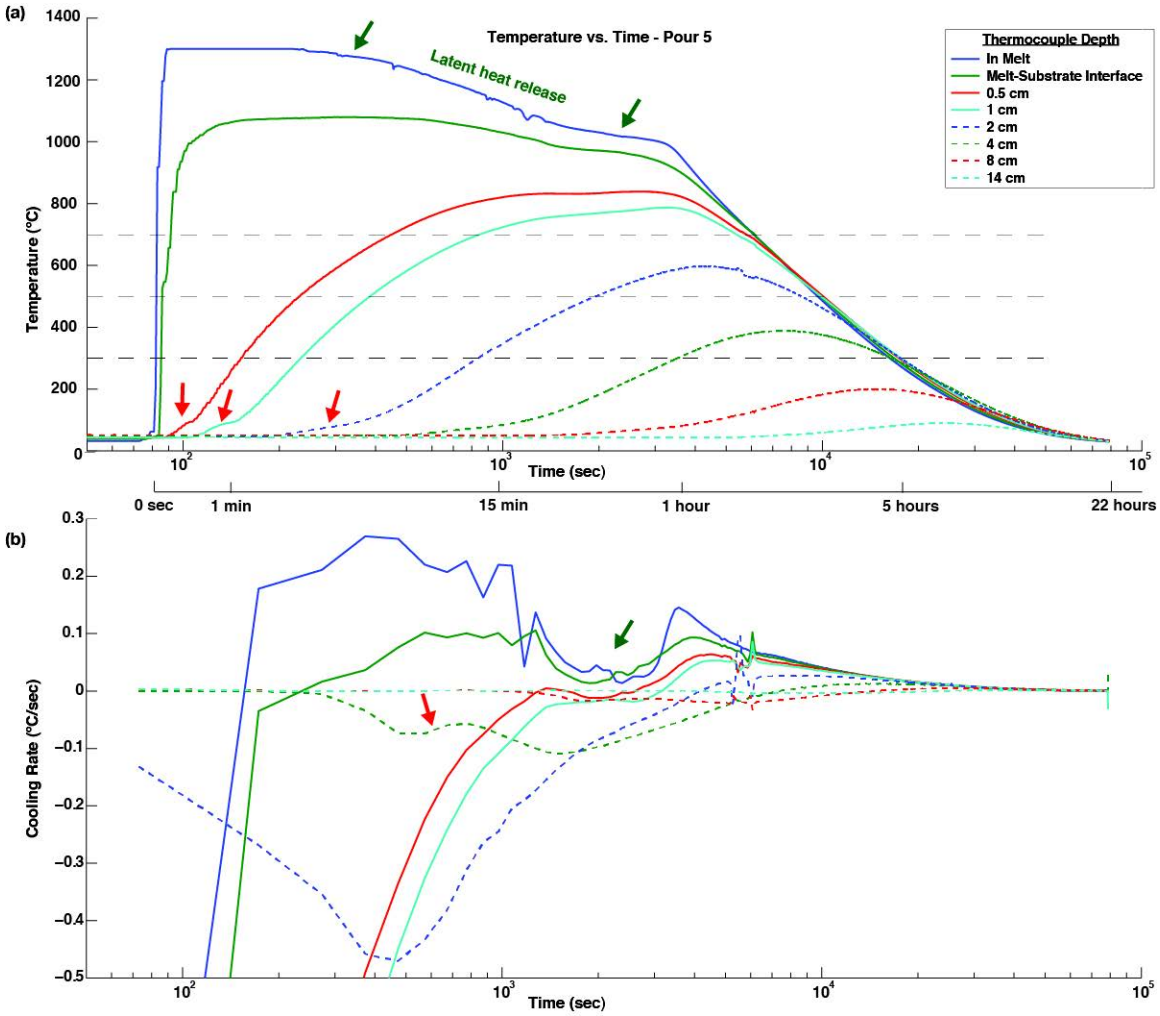

Figure 3.6 Temperature data from Pour 5.

Temperature data from Pour 5. (a) Temperatures as a function of time measured by each thermocouple (b) Cooling rates measured by thermocouples in ˚C s^{-1} averaged over 100 s intervals and plotted against time. Negative cooling rates indicate heating at a given location. The top two thermocouples were located in the melt core and at the melt–simulant interface, respectively. Other thermocouples were located at the depths in the simulant indicated in the legend. Green arrows indicate effects of inferred latent heat release due to crystallization of microlites. Red arrows indicate effects of water vaporization from simulant.

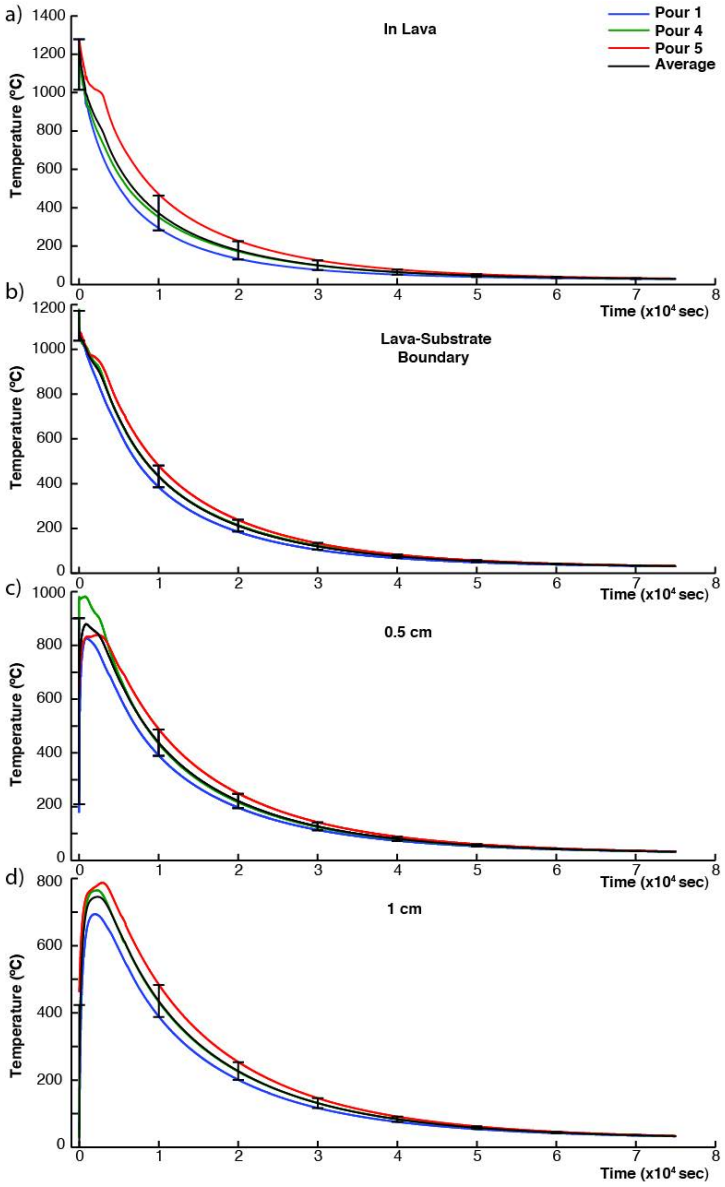

Figure 3.7 Experimental temperatures at depth.

Temperature as a function of time (a) within the lava block, (b) at the melt-simulant interface, (c) at 0.5 cm depth, and (d) at 1 cm depth for Pours 1, 4, and 5, and the average of the experiment temperatures. Error bars represent standard deviation of the average experiment temperatures at given times.

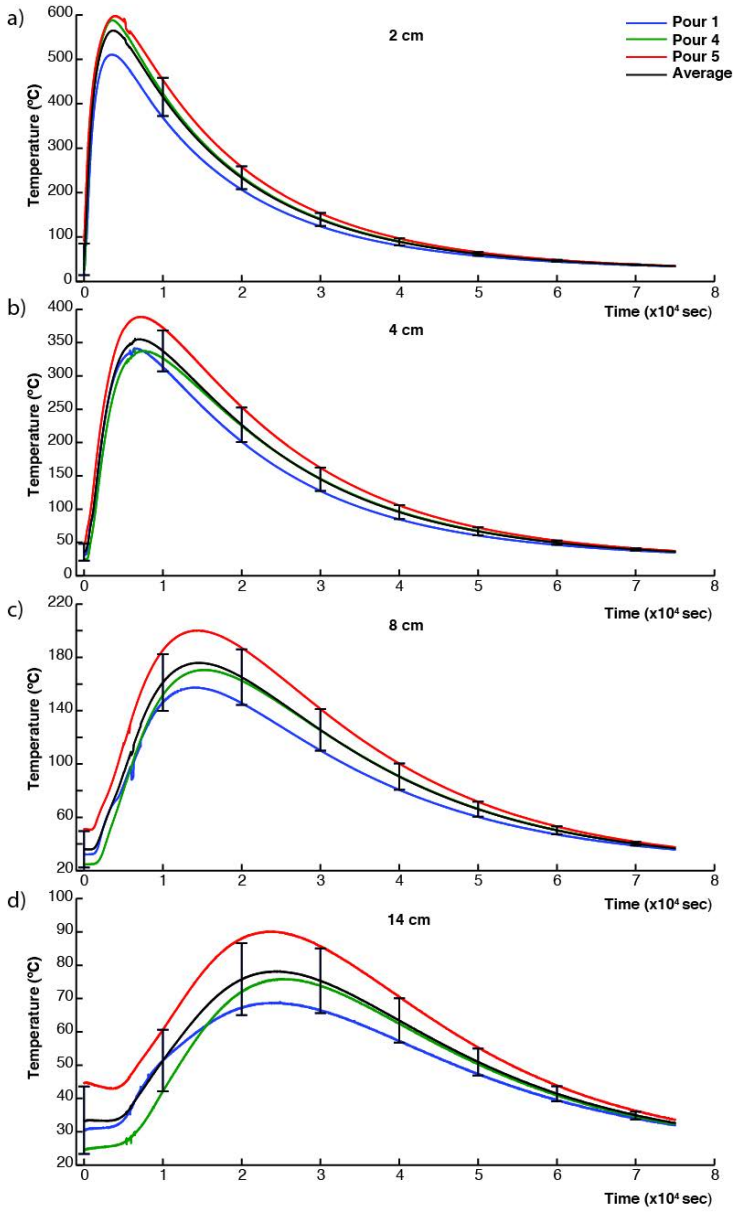

Figure 3.8 Experimental temperatures at depth.

Temperature vs. time at (a) 2 cm, (b) 4 cm, (c) 8 cm, and (d) 14 cm depth for Pours 1, 4, and 5, and the average of the experiment temperatures with time. Error bars represent standard deviation of the average experiment temperatures.

temperature limit of specific heat capacity based on the crystal lattice structure of the material. Similar definitions were adopted by *Rumpf et al.* [2013] and *Patrick et al.* [2004].

The simulant bulk density was set to 1600 kg m^{-3}, as determined from the regolith packing density of the experimental containers. Initial simulant temperatures were set to match experimental values. The temperature boundary condition at the surface of the modeled regolith simulant was described by a time-variant cooling rate using the measured melt–simulant interface temperatures (Figure 3.4, 3.5, 3.6, 3.7b). The modeled regolith effective thermal conductivity was adjusted in increments of 0.05 W m^{-1} K^{-1} through a range of constant and temperature-dependent values to find values returning minimum relative error between numerical results and experimental data.

3.5 RESULTS

3.5.1 *General Results*

A total of seven experiments were performed. Below, the results from three are discussed as representative of the full range of experimental results. During each experiment, bubbling was minimal in crucible after removal from furnace, then immediately upon contact of the melt with the regolith simulant, volatile movement was evident in bubbling at and/or inflation of the surface of the melt layer (Figure 3.3, Auxiliary Videos 1 and 2). The bubbling is similar to, but less extensive than, that seen in experiments by *Edwards et al.* [2013], in which lava was poured over wet or icy substrates and isotope analysis of glassy bubble walls indicated the volatiles were derived from the substrate, not degassed

from the lava. However, the lava used in experiments by *Edwards et al.* [2013] was kept at high temperatures for several hours to ensure degassing of volatiles. In experiments presented here, lava was poured soon after becoming fully molten, potentially allowing for residual volatiles to remain in the melt. Therefore, volatile movement in our experiments may be the expression of the degassing of volatiles from the melt, the expansion of interstitial air in the simulant, and/or degassing of water in the simulant.

Figure 3.7 and Figure 3.8 show plots of temperature vs. time for Pours 1, 4, and 5 at each thermocouple with error bars representing the standard deviation in temperatures at a specific time. The temperature curves differ slightly for the three experiments as a result of differences in the initial temperatures of melt and substrate, and in the exact location of thermocouples. The differences in temperature variation with time between Pours 1, 4, and 5 are relatively small, with a maximum standard deviation of 66.5 ˚C (6.0 %) at the melt–substrate interface immediately after the melt is poured (Figure 3.7a). The substantial variabilities observed in the surface and "in-melt" temperatures for each experiment (Figures 3.4a, 3.5a, and 3.6a) are due to volatile movement within the system and the resulting movement of the surface crust. Deeper parts of the simulant achieved successively lower temperatures than upper portions, as a result of the insulating nature of the particulate material, which suppresses the downward propagation of the heat pulse (Figure 3.8). Delayed cooling in the initial hour of the experiments (green arrows in Figures 3.5a and 3.6a) is similar to expressions of latent heat of crystallization release predicted by *Brandeis et al.* [1984] and *Brandeis and Jaupart* [1987], and observed by *Keszthelyi* [1995] at the base of cooling pāhoehoe flows at Kīlauea Volcano, Hawai‘i.

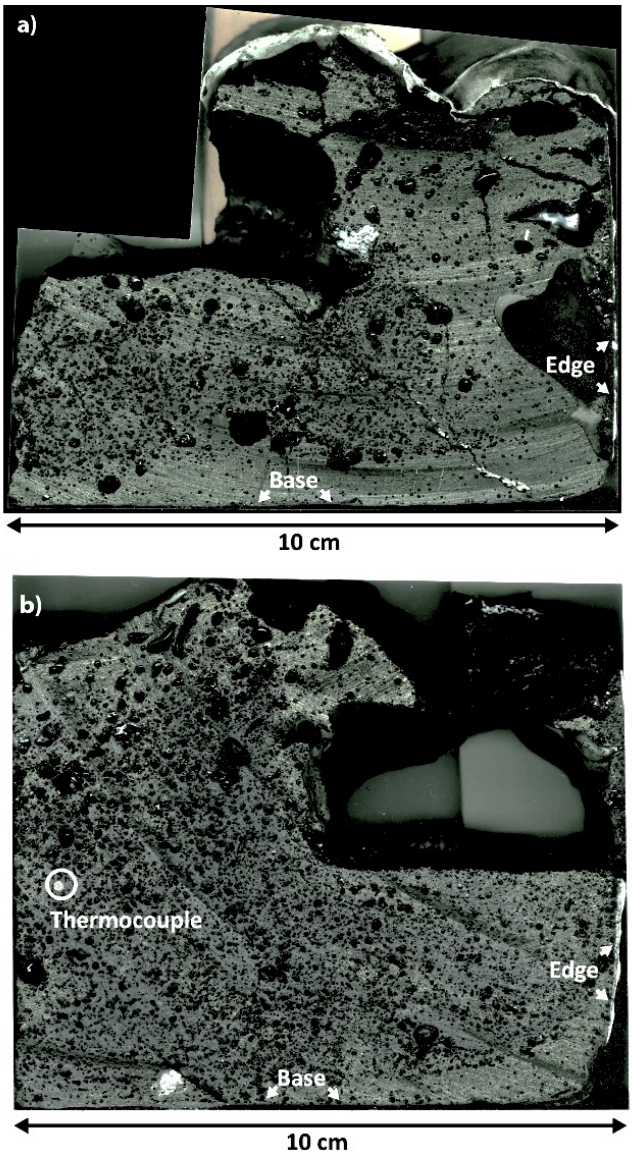

Figure 3.9 Cut lava blocks.

Lava blocks from (a) Pour 1 and (b) Pour 2 cut to view internal features. Blocks are 10 cm wide and 7–8 cm high. The cuts on left side were made at the center of block. The right sides show white calcium silicate material that adhered to the basalt during the experiment. A thin layer of sintered regolith simulant is visible at the bases, and a cut thermocouple is visible (circled) on the left side in (b).

The blocks of solidified melt resulting from the experiments are moderately vesicular (Figure 3.9), with vesicles ranging from <1 to 5 mm in diameter, and increasing in size toward the surface of the blocks, where large voids (~2–5 cm) are present. We infer that the vesicles result from volatile movement observed as bubbling at the melt surface. A very fine layer (<1 mm) of regolith is sintered to the base of each block. Upon dismantling of the experimental containers, red baked regolith was observed to depths of 3–4 cm beneath the solidified blocks.

3.5.2 *Pour 1*

Temperature data for Pour 1 are shown in Figure 3.4. The initial temperature of the melt was 1211±9 ˚C, as measured by thermocouple embedded in the melt. Ambient temperature was ~ 29 ˚C and the initial temperature of the regolith simulant was 32 ˚C. Lava surface temperature was not measured in this experiment. Temperatures within the melt (dark blue line in Figure 3.4a) were higher than those at the melt–substrate interface (solid blue line in Figure 3.4a) for the first 10 min. after the pour. The heat pulse from the molten basalt is seen at the 1-cm thermocouple within 30 s. A subtle shoulder between 70 and 94 °C is evident in several temperature curves, which we infer to be the result of delayed heating as energy is expended vaporizing water from the simulant (depression shown by red arrows in Figure 3.4). This effect is expressed as decreases in the cooling rates in Figure 3.4b. The temperatures at which the shoulder is present decrease with increasing depth in the regolith simulant. After approximately 90 min. (5400 sec.), the heat pulse is seen at 14 cm (Figures 3.4a and 3.8d). A maximum temperature of 69 ˚C is

Table 3.2 Maximum depths of key volatilization isotherms.

		Maximum Isotherm Depth (cm)		
		300 °C	**500 °C**	**700 °C**
Experimental	**Pour 1**	4 – 8	2 – 4	0.5 – 1
Range	**Pour 4**	4 – 8	2 – 4	1 – 2
	Pour 5	4 – 8	2 – 4	1 – 2
Numerical	**Pour 1**	5.6	2.5	1.0
Constant k_e	**Pour 4**	5.7	2.7	1.1
	Pour 5	7.2	3.4	1.4
Numerical	**Pour 1**	5.8	2.7	1.1
Variable k_e	**Pour 4**	5.9	2.9	1.3
	Pour 5	7.2	2.9	1.6

reached after about 7 hours at this location (blue curve in Figure 3.8d). Latent heat signatures resulting from microlite crystallization are not evident in the temperature data of Pour 1.

3.5.3 *Pour 4*

Temperature data for Pour 4 are shown in Figure 3.1. The temperature curves for Pour 4 are close to the average temperatures of the three experiments discussed here (Figures 3.7 and 3.8). The initial temperature of the melt in Pour 4 was 1200±9 ˚C, and the initial temperature of the simulant was at the ambient temperature of 27 ˚C. Lava surface temperatures, as measured by infrared thermographic camera, dropped below 1000 ˚C within 20 s after exposure to the ambient environment (purple curve in Figure 3.5a). Temperatures within the melt were initially higher than those at the melt–simulant boundary and within the regolith, and then declined rapidly as crust formed at the surface within 1–2 minutes (dark blue solid curve in Figure 3.5a). The heat pulse from the molten basalt was recorded nearly immediately (within 10 s) in the upper 0.5 cm of the regolith simulant. Temperatures at the melt–simulant boundary (green solid curve in Figure 3.5a) initially decreased and then leveled off temporarily between ~5 and 60 min. (green arrows in Figure 3.5a), which we infer to be the consequence of crystallization of microlites and the propagation of the resulting latent heat pulse downward into the regolith simulant. Latent heat signatures are seen clearly between ~5 and 60 min. at 0.5 cm depth (red solid curve in Figure 3.5a), where cooling rates drop to <0.1 ˚C s^{-1} during the period of latent heat release (Figure 3.5b), and to a lesser extent in the cooling rates at 1 cm depth (light blue solid curve in Figure 3.5b). A small shoulder, likely the

result of water vaporization in the simulant, between 70 and 94 ˚C is evident in several temperature curves (red arrows in Figure 3.5). At 14 cm depth, significant heating did not occur until ~1.5 hours after the melt was emplaced, and the temperature achieves a maximum of only ~76 ˚C (green curve in Figure 3.8d).

3.5.4 *Pour 5*

Figure 3.6 shows thermocouple data for Pour 5. This experiment had the highest melt temperature, with the initial temperature exceeding 1300 ˚C, the maximum temperature that can be read by the data logger (Figure 3.6a). The maximum temperature detected by the infrared thermographic camera was 1284 ˚C. Ambient temperature was 30 ˚C and the initial regolith temperature was slightly elevated at 40–52 ˚C, increasing with depth, as a result of incomplete cooling after removal from the drying oven (apparent in red curve in Figure 3.8 c and d). Melt temperature dropped below 1300 ˚C at 2.6 mins. after the pour. The "in-melt" temperature remained elevated above the lava–substrate boundary temperature for the first 1.8 hours (Figure 3.6a). Clear plateaus are seen in the cooling curves between ~1 min. and ~1 hour for the melt, melt–substrate boundary, 0.5 cm, and 1 cm thermocouples (green arrows in Figure 3.6a), which we again attribute to latent heat released during the crystallization of microlites. Corresponding dips in the cooling rates to below 0.05 ˚C s^{-1} confirm the suppressed heating of the system (Figure 3.6b). At 0.5 cm, the cooling rate dropped below 0 ˚C s^{-1} at ~25 mins., demonstrating a temporary net heating of the regolith at that location. Shoulders in the 0.5 cm, 1 cm, and 2 cm curves appear between 83 and 94 °C, indicating delayed heating due to water vaporization (red arrows in Figure 3.6). Though not apparent in temperature data (Figure 3.6a), a

decrease in the cooling rate at ~ 10 min. (Figure 3.6b) after the pour indicates delayed heating at the 4 cm thermocouple, likely due to vaporization of water from the simulant. Heating at the lowermost thermocouple (14 cm) becomes apparent at ~ 1.2 hours. This location reached a maximum temperature of 90 ˚C (red curve in Figure 3.8d).

3.5.5 *Isotherm Penetration Depths*

Rumpf et al. [2013] utilized 300, 500, and 700 ˚C as defining temperatures at which specific extra-lunar particles will begin to volatilize out of the lunar regolith [Simoneit et al., 1973]. The maximum penetration depths of these isotherms for this study are summarized in slightly deeper than the 4 cm thermocouple and to 500 ˚C to a depth just below 2 cm. The simulant is heated to 700 ˚C to a depth slightly above the 1 cm thermocouple (Figure 3.4, Table 3.2). For Pour 4, the simulant was heated to 300 ˚C to a depth slightly below the 4 cm thermocouple, and to 500 ˚C to a depth between 2 and 4 cm. The simulant was heated to 700 ˚C to a depth between 1 and 2 cm (Figure 3.5,Table 3.2). For Pour 5, the simulant was heated to 300 ˚C to a depth between 4 cm and 8 cm, and to 500 ˚C to a depth between 2 and 4 cm. The simulant was heated to 700 ˚C to a depth between 1 and 2 cm (Figure 3.6, Table 3.2).

3.5.6 *Numerical Analysis*

Figures 3.10, 3.11, and 3.12 show the time evolution of the regolith simulant temperature profiles, comparing experimental data (symbols) with the best-fit numerical simulation results (curves) for Pours 1, 4, and 5, respectively. The effective thermal conductivities used to produce the best-fit simulations, together with the relative error, are shown in

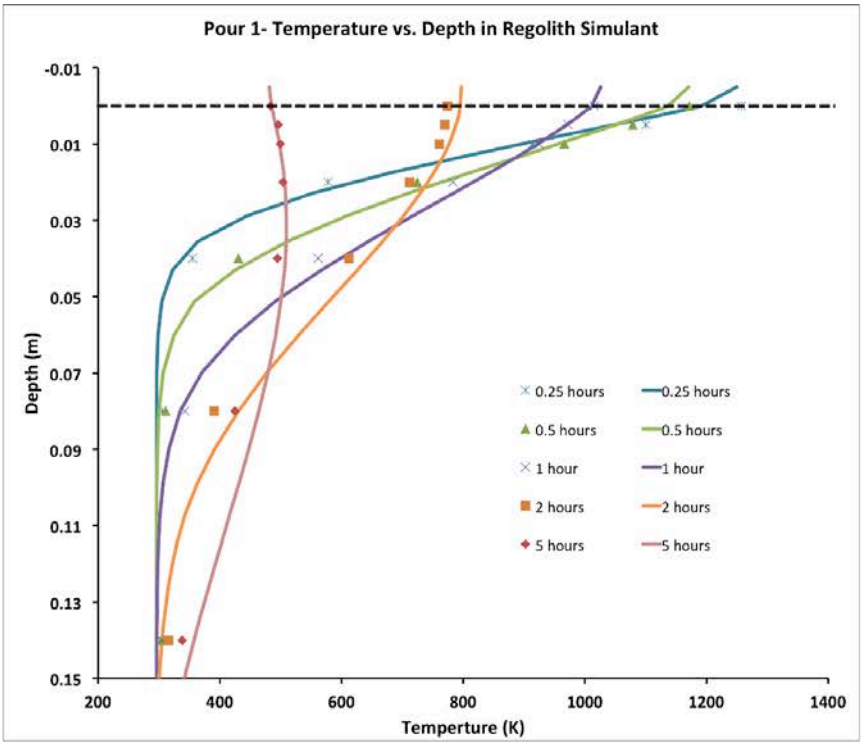

Figure 3.10 Pour 1 – Experimental Data vs. Numerical Model.

Temperature plotted as a function of depth and time for Pour 1. Numerical results are represented by solid lines, and experimental data are represented by symbols. The derived temperature-dependent effective thermal conductivity, k_e, varies linearly from 0.40 W m^{-1} K^{-1} at 23 ˚C to 0.65 W m^{-1} K^{-1} at 1227 ˚C.

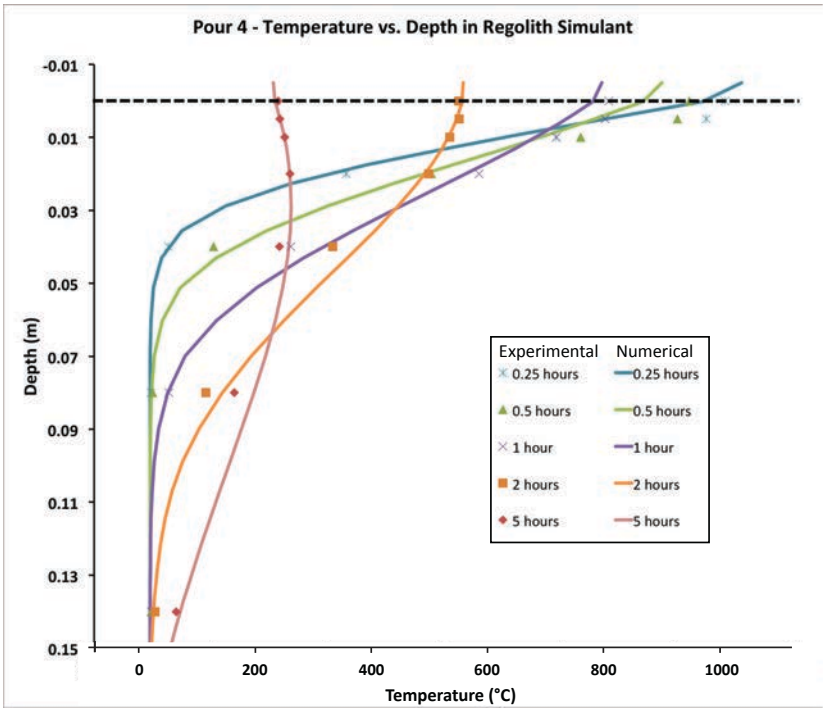

Figure 3.11 Pour 4 – Experimental Data vs. Numerical Model.

Temperature plotted as a function of depth and time for Pour 4 Numerical results are represented by solid lines, experimental data are represented by symbols. The derived temperature-dependent effective thermal conductivity, k_e, varies linearly from 0.35 W m^{-1} K^{-1} at 23 °C to 0.60 W m^{-1} K^{-1} at 1227 °C.

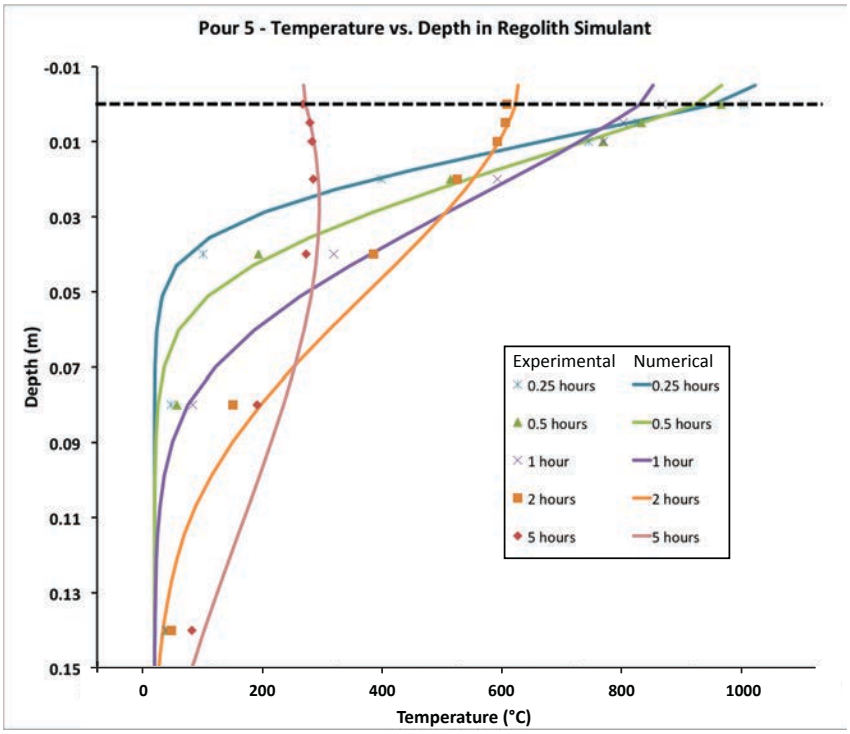

Figure 3.12 Pour 5 – Experimental Data vs. Numerical Model.

Temperature plotted as a function of depth and time for Pour 5. Numerical results are represented by solid lines, experimental data are represented by symbols. The derived temperature-dependent effective thermal conductivity, k_e, varies linearly from 0.45 W m^{-1} K^{-1} at 23 °C to 0.80 W m^{-1} K^{-1} at 1227 °C.

Table 3.3 Model effective thermal conductivity values for GSC-1.

	Effective Conductivity, k_e (W m^{-1} K^{-1})			Relative Error (%)
	Variable k_e	**Max k_e at 1227 °C**	**Min k_e at 23 °C**	**Variable k_e**
Pour 1	$k_e = 2.076\times10^{-4}T + 0.339$	0.65	0.40	2.78
Pour 4	$k_e = 2.076\times10^{-4}T + 0.288$	0.60	0.35	3.80
Pour 5	$k_e = 2.907\times10^{-4}T + 0.364$	0.80	0.45	3.86
	Constant k_e			**Constant k_e**
Pour 1		0.50		2.84
Pour 4		0.45		4.24
Pour 5		0.60		4.22

Table 3.3. We use a linear fit to describe the temperature dependency of effective thermal conductivity because the complexities of the contributing factors (Equation 2) cannot be differentiated in the scope of this experiment. A linearly increasing fit will allow for first-order validation of temperature dependence, however more detailed fit is not a useful improvement unless the effects of each term in Equation (2) can be resolved. We find that the effective conductivities derived for the regolith simulant were similar among the three experiments. The optimized temperature-dependent conductivities increase from 0.35–0.45 W m^{-1} K^{-1} at 23 ˚C to 0.60–0.80 W m^{-1} K^{-1} at 1227 ˚C (Table 3.3). When constant thermal conductivities were used to fit the experimental data, values ranged from 0.45–0.60 W m^{-1} K^{-1}, which represent averaged effective conductivities over the temperature range of interest. Relative errors between experimental and numerical values at depth were lower for simulations using temperature-dependent thermal conductivity definitions.

Maximum penetration depths of the 300, 500, and 700 ˚C isotherms (Table 3.1) are summarized in Table 3.2. The experimental depths are given as ranges between thermocouple depths. The numerical depths are derived from PHOENICS simulations. Each numerical model value falls within the range prescribed by experimental data. Simulations that include variable definitions of effective thermal conductivities have larger isotherm penetration depths than simulations with constant effective conductivities. Pour 5, which had the highest initial melt temperature (>1300 ˚C) consistently has the highest maximum penetration depths, with the 300, 500, and 700 ˚C isotherms reaching maximum depths of 7.2, 2.9, and 1.6 cm, respectively, for simulations with variable conductivities. Pours 1 and 4 had maximum depths of 5.8, 2.7, and 1.1 cm and 5.9, 2.9, and 1.8 cm, respectively, for the 300, 500, and 700 ˚C isotherms.

An analytical model was also compared to experimental values for Pour 4. The model simulated unsteady heat conduction from a surface into regolith with constant properties (k_s = 0.45 W m^{-1} K^{-1}, c_{reg} = 900 J kg^{-1} K^{-1}) using the one-dimensional, time-dependent heat conduction equation [*Mills* 1999]. The surface temperature was defined to match experimental values. The analytical model of conduction into regolith gave a fair first-order approximation of the heat conduction in the experiment (Figure 3.13), but did not fully represent heat transfer in the experiment because the simplification overestimated temperatures early in the simulation and underestimated temperatures at later time.

An analytical model of the cooling of the melt block was less successful (Figure 3.14). Heat loss was approximated from the top of the melt by a general solution for the convective cooling of the surface of a slab [*Mills*, 1999]. Lava was defined with constant properties (k_s = 1.5 W m^{-1} K^{-1}, c = 1000 J kg^{-1} K^{-1}) with a convective heat transfer coefficient of 25 W m^{-2} K^{-1}. This method underestimated initial heat loss from the melt surface (Figure 3.14a) as it lacked heat loss due to radiation. Surface heat loss is overestimated at later times, possibly due to latent heat release in the experimental data contributing additional heat to the system. At depth in the melt, the analytical model underestimates heat loss at 4 cm below the surface (Figure 3.14b) and at the melt–substrate boundary (Figure 3.14c), as the lower thermal boundary with the substrate is not included in the analytical model. Future analytical models should include radiative heat transfer from the surface, a condition describing the melt-substrate thermal boundary, and latent heat release within the melt block The difficulty involved in including such

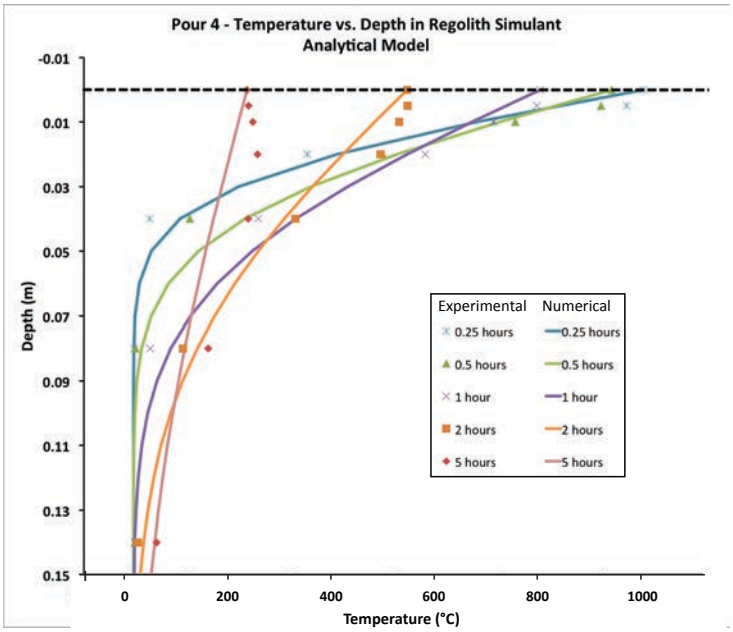

Figure 3.13 Pour 4 – Experimental Data vs. Analytical Model - Regolith.

Temperature plotted as a function of depth and time for Pour 4. Experimental data are represented by symbols, analytical results are represented by solid lines. Analytical solution uses constant regolith properties (k_s = 0.45 W m^{-1} K^{-1}, c_{reg} = 900 J kg^{-1} K^{-1}) and experimental temperatures with time as upper boundary condition.

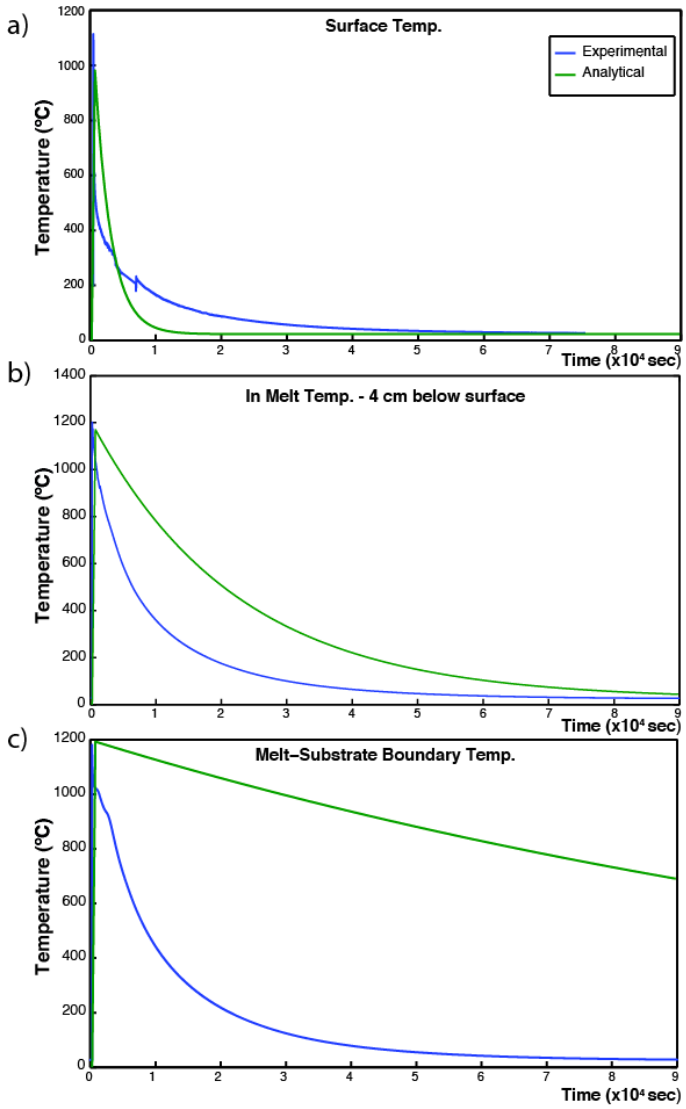

Figure 3.14 Pour 4 – Experimental Data vs. Analytical Model - Lava.

Temperature as a function of time (a) at melt surface, (b) 4 cm below melt surface, and (c) at the melt-simulant interface, for Pour 4 and for an analytical model approximating convective cooling from the melt surface.

.complexities in an analytical model support the use of numerical finite-volume or finite-element models to simulate lava–substrate heat transfer.

3.6 DISCUSSION

We have used numerical simulations to constrain the temperature-dependence of the effective thermal conductivity of a lunar regolith simulant, GSC-1, up to 1227 ˚C, adding to a small set of measurements of lunar regoliths and lunar regolith simulants at high temperatures.

3.6.1 *Thermal Conductivity*

Thermal conductivity measurements of particulate materials to elevated temperatures were previously sparse. Thermal conductivity has a greater influence on lava–substrate heat transfer than other thermophysical properties [*Fagents and Greeley,* 2001; *Rumpf et al.*, 2013], so it is crucial that substrate conductivity be properly defined in thermophysical models. In the context of these experiments, we present an effective thermal conductivity (Equation 2) instead of the individual components comprising thermal conductivity, because we are unable to distinguish between the effects of gas conduction and those of solid and radiative conductivity. In addition, it is difficult to theoretically derive the thermal conductivity of the lunar regolith. Thermal conductivity is a complex property that depends on a number of factors including composition, grain size, crystallinity, and porosity. The lunar regolith is unsorted and highly variable on small scales, laterally and with depth [*McKay et al.*, 1991]. Attempts to define the solid

portion of thermal conductivity of the lunar regolith need not be specified beyond the expected variability of the surface regolith. However, the model presented here relies on the effective thermal conductivity and adequately reproduces the physics of the experiment; it is not necessary to present each conductivity factor as a separate component.

This study constrains an effective thermal conductivity, k_e, that combines the conductivity of grain-to-grain contacts, k_c, radiation across pore spaces, k_r, and gas conductivity, k_g (Equation 2). Effective thermal conductivities on the Moon will be lower than those on the Earth for the same particulate material. Under hard vacuum conditions, the gas term k_g is a negligible contribution to k_e (Equation 2), leading to thermal conductivities with a strong temperature dependence: k_e will be very low at low temperatures, due to the porosity of lunar regolith, and k_e will be high at high temperatures, because radiation across pore spaces (k_r, with a T^3 dependence, Figure 3.1) dominates over grain-to-grain conduction (k_c). However, the heating of a regolith substrate would have released hundreds of ppm of implanted volatiles [*Simoneit et al.*, 1973; *Haskin and Warren*, 1991], temporarily introducing gases into the pore spaces. The presence of interstitial gas would have increased the contribution of the k_g term in Equation (1) and temporarily raised the effective thermal conductivity of the regolith [*Woodside and Messmer*, 1961; *Presley and Christensen*, 1997]. Although the contribution of k_g due to several hundreds of ppm of volatiles toward the total effective thermal conductivity would be minor compared to the atmospheric conditions of our experiments, the increase in k_e would have led to an increase in the rate of heat transfer into the substrate and an increase in the depths to which pertinent isotherms (Table 3.1)

penetrate beneath a lava flow. Therefore, the depths to which the simulant in our experiments was heated to volatilizing temperatures (see Table 3.2) can be considered generous maximum depths of potential heating of the lunar regolith by an overlying lava flow. It is unrealistic that pressures from volatilized particles in the lunar regolith would exceed atmospheric pressures on Earth.

Rumpf et al. [2013] found that the maximum penetration depths of the 300 ˚C, 500 ˚C, and 700 ˚C isotherms in a lunar regolith deposits heated by a 1-meter thick lava flow will be 20.4, 15.1, and 10.4 cm, representing heating depth to lava thickness proportions of 20.4%, 15.1 %, and 10.4%, respectively. The experiments described here found that a ~9 cm basalt melt heated lunar regolith simulant to 300 ˚C, 500 ˚C, and 700 ˚C to maximum depths of 7.2, 3.4, and 1.6 cm, representing heating proportions of 80%, 37%, and 18%, respectively. The large difference in heating depth proportions is primarily due to the contribution of gas conduction in the substrate. Additionally, *Rumpf et al.* [2013] demonstrated that relative heating depths decrease with increased flow thicknesses, further supporting the hypothesis that flows thicker than our ~9 cm basalt blocks will heat to depths proportionally less than those in this study.

Yuan and Kleinhenz [2011] measured the apparent thermal conductivity (k_a) of a different lunar regolith simulant, JSC-1A. This simulant showed a linear increase in k_a with temperature, giving values of $k_a = 0.2183$ W m^{-1} K^{-1} at 62.65 ˚C to $k_a = 0.2878$ W m^{-1} K^{-1} at 204.1 ˚C under ambient pressure conditions. The linear increase was explained as a dependence on thermal stresses within the particulate bed increasing contact areas between grains, thereby increasing conduction across the bed. Detection of thermal stresses is beyond the scope of the present experiment and any such effects would be

accounted for within our determination of effective thermal conductivity, k_e. The higher values of k_e found in this study compared to k_a found by *Yuan and Kleinhenz* [2011] at equivalent temperatures could be explained by differing experimental methods or conditions, or inherent differences in the physical properties of GSC-1 and JSC-1A. Our values are a closer fit to values of effective thermal conductivity at high temperatures for packed beds of particulate alumina and silica measured by *Botterill et al.* [1989 a and b].

3.6.2 *Study Limitations*

Limitations in experimental procedure, instrumentation, and model formulation contributed to residual differences between our numerical and experimental results (Figures 3.10, 3.11, and 3.12), and between effective thermal conductivity definitions among individual experiments. Some variations in cooling curves among the experiments are likely due to disturbance of the thermocouples prior to and during the course of the experiments, which makes their precise depths uncertain (Figures 3.10, 3.11, and 3.12). Furthermore, K-type thermocouples have a 0.75% measurement error (www.omega.com) resulting in a maximum possible error of ±10 ˚C at high temperatures. Differences in the exposure time of regolith to the ambient environment during container packing and immediately before the lava pours may have affected the water content of regolith, despite extensive drying. Energy needed as latent heat to vaporize water resorbed into the simulant temporarily suppressed heating of the regolith (red arrows in Figures 3.5 and 3.6). Furthermore, the presence of vapor in the simulant would have increased the contribution of gas conductivity to effective thermal conductivity, thereby increasing conduction within the regolith. While these latter two effects may have acted in

opposition to one another in influencing the temperature distribution, effects of water vaporization in the simulant were not explicitly included in the model formulation. These subtleties may therefore have created residual mismatches between the model results and experimental data, particularly in the first hour after the pour when most volatile movement occurred.

3.6.3 *Lunar Applications*

Experiments involving regolith simulant are an important contribution toward understanding the history of the Moon and toward future exploration of our Solar System. The lunar surface has been passively recording events in the neighborhood of the Earth since soon after its formation. Exogenous particles, including solar wind and solar flare particles, the cosmogenic products of galactic cosmic rays [*Wieler et al*., 1996; *NRC*, 2007], and material ejected from the rocky planets [*Spudis,* 1996; *Armstrong et al*., 2002; *Ozima et al.*, 2005, 2008; *Armstrong*, 2010; *Crawford et al.*, 2008; *Joy et al.,* 2011], has been implanted in the surface regolith. Discovery of regolith deposits containing ancient exogenous particles would reveal information about Solar System history not available on Earth. Surface regolith deposits returned during the Apollo missions were oversaturated and did not contribute toward a concise record of past Solar System activity [*McKay et al.*, 1991; *Joy et al.,* 2011]. Coverage by a lava flow would have protected exogenous particle records in paleoregolith deposits and provide solid rock for radiometric dating of exposure period [*McKay et al*., 1989; *Spudis*, 1996; *Crawford et al*., 2007, 2010; *McKay*, 2009; *Spudis and Taylor*, 2009]. However, the overlying lava flow would heat the regolith, volatilizing particles and damaging the ancient record to

some extent. *Rumpf et al*. [2013] found that a 1-meter lava flow will have heated the underlying regolith to temperatures of 300 ˚C, 500 ˚C, and 700 ˚C to maximum depths of 20.4, 15.1, and 10.4 cm, respectively. These depths represent minimum heating depths by an overlying flow, as they do not account for added conductivity due to volatilized gases in the lunar regolith as it is heated. Additional gas conductivity will increase the rate of heat transfer into the substrate, thereby increasing the penetration depths of relevant isotherms. Here, we find that a ~ 9 cm thick block of molten basalt will heat the underlying regolith simulant to temperatures of 300 ˚C, 500 ˚C, and 700 ˚C to maximum depths of 7.2, 3.4, and 1.6 cm. The experimental depths represent the maximum penetration depths of pertinent isotherms in regoliths on the lunar surface because temporary gas pressures caused by volatilization of particles are unlikely to reach levels comparable to atmospheric pressures on Earth.

Heat flow experiments were conducted on the lunar surface during the Apollo 15 and 17 missions [*Langseth et al.*, 1973]. Experiments used two one meter long probes buried ten meters apart and connected by thermocouples. Temperatures were monitored to capture planetary heat flux and to measure response to heating of the surrounding regolith by small heaters [*Langseth et al.*, 1972]. Heat flow values of 0.031 and 0.022 W m^{-2} (± 20%) were found at Apollo 15 and 17 sites, respectively [*Vaniman et al.*, 1991 and references therein]. Regolith thermal conductivities were found to range between 0.011 and 0.0295 W m^{-1} K^{-1}, (refined to 0.0146 to 0.0264 W m^{-1} K^{-1} by *Grott et al.* [2010]) at temperatures at or below 100 °C [*Langseth et al.*, 1976; *Vaniman et al.*, 1991 and references therein]. Variance is attributed to local variability in bulk density of the regolith. In constrast, low-temperature effective thermal conductivity was determined to

be 0.35 – 0.45 W m^{-1} K^{-1} at 27 °C in this study. These values are 14 – 31 times the *in situ* lunar values presented by *Grott et al.* [2010]. The difference between the two thermal conductivity ranges is caused by the presence of a gas phase in our experiments, displaying that under terrestrial conditions, gas conductivity, k_g, dominates effective thermal conductivity of particulate materials at low temperatures.

We have not explicitly derived the different components of effective thermal conductivity, k_e, (Equation 2) for the lunar regolith simulant used in this study, but it is theoretically possible to predict gas conductivity, k_g, radiative conductivity, k_r, and the grain-to-grain conductivity, k_c, of the regolith under lunar conditions. Each factor can be presented within a range of theoretical values to match varying conditions at the lunar surface. Gas conduction depends on the composition and concentration of volatiles available and on temperature via two processes, 1) as implanted solar wind and solar ray particles volatilize (Table 3.1) they will affect substrate gas pressures, and 2) gas temperature will affect the heat capacity, mean molecular velocity, and mean free path of a gas (Equation 3). Radiative conductivity depends on material emissivity and porosity and the temperature gradient within a system. The solid conductivity of the regolith depends on temperature, composition, grain size, crystallinity, and porosity at a given location. Close examination of the above factors would allow for the distinction between contributing components in regolith effective conductivity leading to a more accurate definition of regolith conductivity on the Moon.

Our experiments are also of relevance to terrestrial volcanology. Active lava flows commonly flow over a variety of substrates, including solid lava, sands, soils, and volcanic tephra. Each of these materials have effective thermal conductivities that vary

based on composition, grain size, moisture content, porosity, and organic content. Substrate conductivity will determine the rate of heat transfer from the flow base, which will affect temperatures within the flow and influence the mobility of the flow. Rates of basal cooling will be lower for lavas that flow over particulate substrates potentially prolonging the duration the flow is active. In addition, heat transfer into wet or icy substrates or into organic matter beneath a lava flow can volatilize substrate materials leading to locally explosive activity. Lava–substrate heat transfer should be carefully considered in lava flow path prediction modeling and in other models involving thermophysical treatments of lava.

3.7 CONCLUSIONS

Experiments measuring the heat transfer from molten basalt into the underlying substrate have verified the underlying physics of previous numerical models that examine the survivability of extra-lunar particles implanted in paleoregoliths covered by mare basalt flows [*Rumpf et al*., 2013; *Fagents et al.*, 2010]. *Rumpf et al.* [2013], posited that solar wind and solar flare particles and the cosmogenic products of galactic cosmic rays will be best preserved at locations on the lunar surface where thin flows overlie substantial regolith deposits. Flow margins provide favorable conditions for volatile preservation as flows will likely be thinner than at proximal locations and because flows tend to stagnate at the margins, where they are unlikely to form channels or tubes that provide continuous heating. Here, regolith simulant was heated by ~ 9 cm of overlying molten basalt to particle-volatilizing temperatures of 300 ˚C, 500 ˚C, and 700 ˚C to maximum depths of

7.2, 3.4, and 1.6 cm. These depths could be scaled to lava flow thickness to provide an upper limit to the depths to which paleoregoliths will be heated on the Moon because regolith effective thermal conductivity will be several times less under vacuum conditions on the Moon than on Earth, where the effects of gas conductivity dominate heat transfer within particulate materials. Our experiments also help to constrain the temperature dependence of the effective thermal conductivity of lunar regolith simulant (GSC-1), k_e increases linearly from 0.35–0.45 W m^{-1} K^{-1} under ambient conditions to 0.6–0.8 W m^{-1} K^{-1} at basaltic eruption temperatures (~1227 ˚C). These values are greater than previous measurements of the thermal conductivity of JSC-1a [*Yuan and Kleinhenz*, 2011], a different lunar regolith simulant, but are comparable to effective thermal conductivity measurements of particulate alumina and silica by *Botterill et al.* [1989 a and b].

An understanding of lava–regolith heat transfer can aid in the identification of ancient exogenous particles in intercalated layers of lava and regolith on the lunar surface. Discovery and extraction of solar flare and solar wind particles and the products of galactic cosmic rays during future missions to the lunar surface would yield insight into the histories of solar and galactic activity since soon after formation of the Moon.

3.8 ACKNOWLDEGEMENTS

Financial support for M.E.R through the NSF Graduate Research Fellowship Program and a Kleinman Grant for Volcano Research. Many thanks to the University of Hawai‘i Department of Art and Art History, F. Roster, J. Rubin, and G. Gertl for their time and

the use of their foundry. The authors wish to thank P. Lucey for valuable comments and G. Moore and the UH Department of Geology and Geophysics for additional financial support.

CHAPTER 4.

THICKNESSES OF LUNAR MARE LAVA FLOWS: COMPARISON OF LAYERED MARE UNITS WITH TERRESTRIAL ANALOGS

4.1 ABSTRACT

Recent advances in satellite imaging technology have greatly improved our observations of planetary surfaces. The Lunar Reconnaissance Orbiter (LRO) Narrow Angle Camera (NAC) records images with resolutions better than 0.5 m per pixel, resolving meter scale features on the surface of the Moon. NAC images have revealed layered deposits, interpreted to be sequences of mare basalt flows, in the walls of impact craters on the lunar nearside. However, caution must be exercised in the interpretation of surface processes from morphologies of features that are unresolvable or close to the limits of detectability as our knowledge of surface processes, including lava flow emplacement, on the Moon is not fully developed.

Here we conduct a terrestrial analog study to better constrain limitations in the measurements of thicknesses of lava flows observed in high-resolution lunar imagery. Using WorldView-2 satellite imagery, we mapped layered basalt flows in the Waiʻanae and Koʻolau Ranges of Oʻahu, Hawaiʻi. Fieldwork at these sites allowed for validation of image interpretations. Of eight transects investigated at three sites on Oʻahu, WorldView-2 imagery provided overestimates of flow thicknesses measured at seven of these sites when compared to field observations, with average image-derived to field-observed thickness ratios between 0.9 and 6.3. Only one location provided a ratio less than 1.0. A primary reason for this overestimation by remote sensing analysis is that many outcropping "layers" within a transect contain more than one individual flow, a distinction that is not visible in satellite imagery. Furthermore, it is likely that many lunar outcrops similarly contain more than one individual flow, suggesting that estimates of lunar flow thicknesses exposed in crater walls are greater than actual flow thicknesses.

Hence, measurements of layered lunar mare lava units in LRO image provided flow thicknesses 2–5 times greater than those derived from images of the O‘ahu study sites. In addition, varying image quality and incidence angles can lead to significant differences in the numbers of flow units identified within lava sequences. We infer that interpretations of lava flows in high-resolution lunar imagery will underestimate the number of flows present in a layered sequence and consequently overestimate the flow thickness. Current interpretations of lava flow thicknesses derived from planetary images are likely inaccurate.

4.2 INTRODUCTION

Characterization of mare basalt thicknesses can provide important insights into the emplacement, dynamics, and history of mare volcanism. Mare lava flows are thought to have been intermittent, flood-like events, which produced high-effusion-rate, high-volume eruptions [e.g., *BVSP* 1981; *Head and Wilson*, 1992]. Estimates of average magma flux over periods of active mare volcanism are determined using age estimates and assessment of the volumes of basalt erupted into mare-filled basins, a measurement reliant on comprehension of mare thicknesses [*Head and Wilson*, 1992; *Hiesinger et al.*, 2002]. While long-duration average flux rates can be calculated using total thicknesses of mare-filled basins, the specifics of individual flow events are more difficult to determine. Observations of the thicknesses of individual flow units and stratigraphic sequences of flows provide parameters for use in models of emplacement dynamics, as well as revealing the time-progression of flow morphologies and effusion rates. Changes in mare basalt flow thicknesses with time would indicate a thermal evolution of the

region, with implications for the overall thermal history of the Moon [*Head and Wilson*, 1992]. In addition, thicknesses of lunar lava flows have implications for the survivability of exogenous particles implanted in regolith deposits preserved between lava flows [*Spudis* 1996; *Fagents et al.*, 2010; *Rumpf et al.*, 2013].

In this study, Lunar Reconnaissance Orbiter (LRO) data are used to constrain the thicknesses of layered lava flows exposed in the walls of impact craters within the lunar mare. Stratigraphy revealed by impact craters is an important tool in understanding lunar surface processes, as surface features (e.g., lava flow margins, volcanic vents) have been degraded through the development of surface regolith, making interpretations of original morphologies difficult. Our comparison study using terrestrial analogs serves to test the accuracy of LRO image interpretations. We begin with a study of 52 locations within four impact craters that display layered sequences of mare basalts. Units are counted at each site and average flow thicknesses are determined using elevation data acquired by the Lunar Orbiter Laser Altimeter (LOLA). The same methods are applied using WorldView-2 (WV2) [*DigitalGlobal*] images and Digital Elevation Models (DEM) of layered basalt flow sequences exposed in valley walls at eight locations on O‘ahu, Hawai‘i. Fieldwork at the terrestrial locations allows for the measurement of *in situ* lava flow sequences to ground-truth remote sensing interpretations. Comparison of average flow thicknesses measured in the field with those derived from the images constrains the accuracy of interpretations of layered deposits using remote sensing data. Inaccuracies in interpretations of terrestrial flow thicknesses imply the possibility of inaccuracies of similar magnitude associated with lava flows observed in lunar images.

4.3 BACKGROUND

4.3.1 *Lunar mare volcanism*

The eruption of basaltic lavas into large impact basins on the near side of the Moon (Figure 4.1) was the last of several stages of lunar volcanism. Mare volcanism peaked at ~ 3.3 to 3.5 Ga and may have lasted until as recently as 1.2 Ga [*Schultz and Spudis*, 1983; *Horz et al*., 1991; *Hiesinger et al*., 2003; *Hiesinger and Head*, 2006]. A range of theories exist about the emplacement mechanism of mare lavas, which are predicted to have been erupted at high temperatures (≥1200 °C) and low viscosities (~10 Pa s) compared to typical terrestrial basalts [e.g., *Murase and McBirney*, 1970; *Taylor et al.*, 1991]. Interpretations of mare volcanic features suggest that eruptions had high effusion rates and large volumes, emplacing broad (hundreds of kilometers) flows, tens of meters thick, similar to terrestrial flood basalts [*BVSP* 1981; *Head and Wilson*, 1992].

Estimates of the thicknesses of mare flows have been made since the Apollo era. Astronauts on the Apollo 15 mission observed and photographed layers in the wall of Hadley Rille, finding thin (< 1 m) lava flows interspersed with massive flows having thicknesses 10–20 m and greater [*Howard and Head*, 1972; *Howard et al.*, 1972; *Swann et al.*, 1972; *Spudis et al.*, 1988; *Vaniman et al.*, 1991]. Orbital photography from the Apollo missions revealed lava flow margin thicknesses ranging between 10 and 60 m [*Schaber*, 1973]. *Gifford and El-Baz* [1981] found thicknesses of 1–96 m using shadow measurements of lava flow front scarps observed in a Lunar Orbiter images and Apollo orbital photographs. These early data sets provided unprecedented views of the lunar surface, however, the data lacked the resolution to resolve features less than several

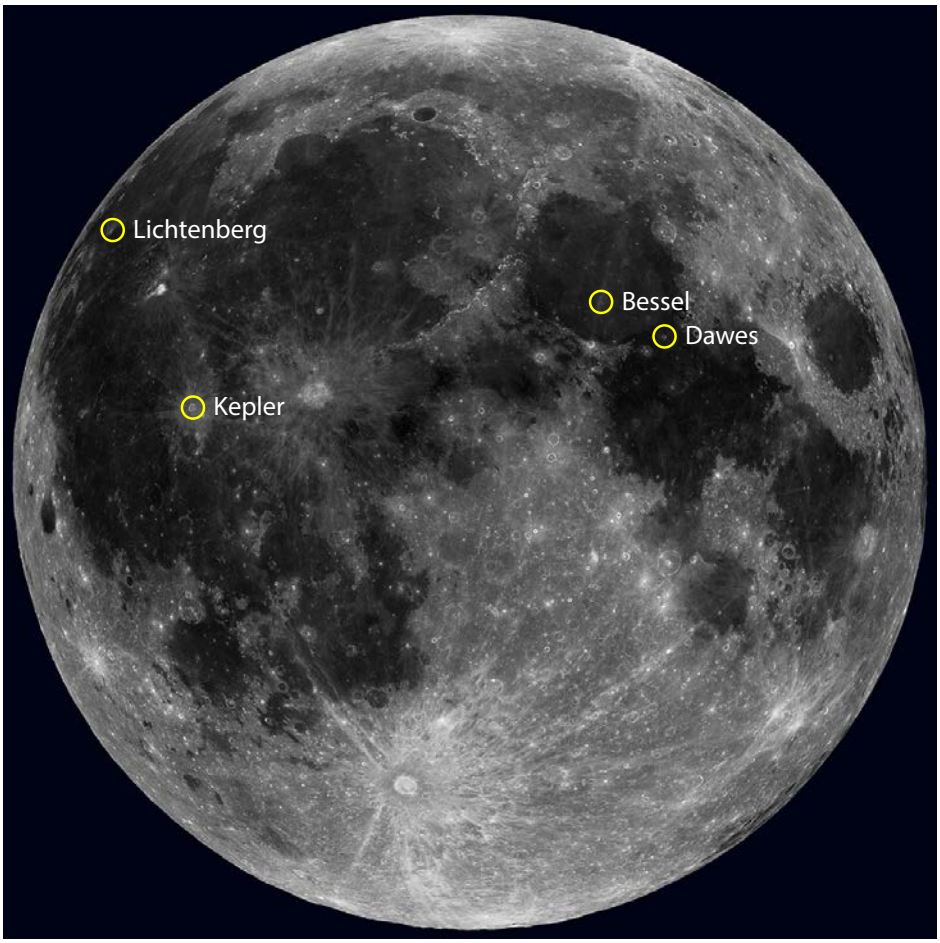

Figure 4.1 LROC WAC mosaic of the lunar nearside.

LROC WAC mosaic of the lunar nearside. Yellow circles indicate location of impact craters in this study [*NASA/GSFC/Arizona State University*].

meters. Additionally, shadow measurements provide only thicknesses of the flow edge from where the shadow is cast, and may not be representative of the full thicknesses of the flow unit. *Hiesinger et al.* [2002] used crater size-frequency distributions to determine flow thicknesses averaging ~30–60 m within several nearside lunar basins. Crater size-frequency distributions are useful for discerning a lava flow unit that is temporally distinct from the surrounding units but cannot discern between individual flows within a complex unit or between flow units that were emplaced within a short time frame. Several studies using Clementine multispectral data revealed compositionally distinct mare basalt flow units with thicknesses from ~80–600 m thick [e.g., *Campbell and Hawke*, 2006; *Weider et al*., 2010]. However, these thicknesses are likely representative of compound flow units, composed of many compositionally similar flows [*Weider et al.*, 2010]. Recent LROC imagery has revealed lava flows with thicknesses < 5 m [*Robinson et al.*, 2012], suggesting regional emplacement of thin flows. Identification of thin flows does not preclude flood-like emplacement when one considers the lower inferred viscosities [*Murase and McBirney*, 1970]. Furthermore, mare basalt emplacement rates likely fluctuated regionally and temporally, producing flows of varying thicknesses depending on effusion rates and proximity to source.

Recently, the high quality of Lunar Reconnaissance Orbiter data has substantially improved our understanding of the lunar surface [*Robinson et al.*, 2010; *Vondrak et al.*, 2010]. LROC imagery has revealed meter-scale layered features in pit craters [*Robinson et al.*, 2012; *Xiao et al.*, 2014], ejecta blocks [e.g., *Kickapoo and Cramer*, 2014], and in the walls of impact craters [e.g., *Robinson et al.*, 2012]. Thicknesses of individual layers measured by *Robinson et al.* [2012] using LROC NAC imagery of both pit craters and

impact craters ranged from 2–14 m. These layered features, interpreted as sequences of mare basalt flow units, have thicknesses comparable to basalt flows erupted at the Hawaiian Islands, USA, suggesting similar morphologies and emplacement processes.

4.3.2 *Hawaiian flow sequences as planetary analogs*

The island of O‘ahu (Figure 4.2) is characterized by two mountain ranges, the Wai‘anae and Ko‘olau Ranges, which are the eroded remains of the Wai‘anae and Ko‘olau basaltic shield volcanoes. Wai‘anae Volcano was active from about 4.0 Ma to 2.9 Ma [*Sherrod et al.*, 2007 and references therein]. Ko‘olau lavas range in age from about 3.0 to 1.8 Ma and were followed by a late stage of predominantly explosive rejuvenated volcanics less than 1.0 Ma ago [*Sherrod et al.*, 2007]. Hawaiian basalt flows are erupted from central vents or fissures and are typically emplaced as ≤ 10 m thick ‘a‘ā or pāhoehoe flows and commonly form channels or tubes. [*Macdonald*, 1953; *Wentworth and Macdonald*, 1953; *Griffiths*, 2000]. Hawaiian basalts are typically erupted at temperatures less than 1200 °C and have viscosities ranging between ~ 10^2 and 10^3 Pa s [*McBirney and Murase*, 1984], 10 – 100 times the viscosity expected for lunar basalts [*Papike et al.*, 1991]. Hawaiian and mare basalts may therefore differ in both rheology and eruption dynamics. However, for this study, we are primarily concerned with the characteristics of outcropped lava sequences and believe Hawaiian basalts provide an adequate analog for this purpose. Specific emplacement mechanisms are a secondary concern and are addressed later in this paper.

Hawaiian localities are commonly used as analogs for flows on planetary surfaces. *Mouginis-Mark and Rowland* [2008] compared images of layered lava

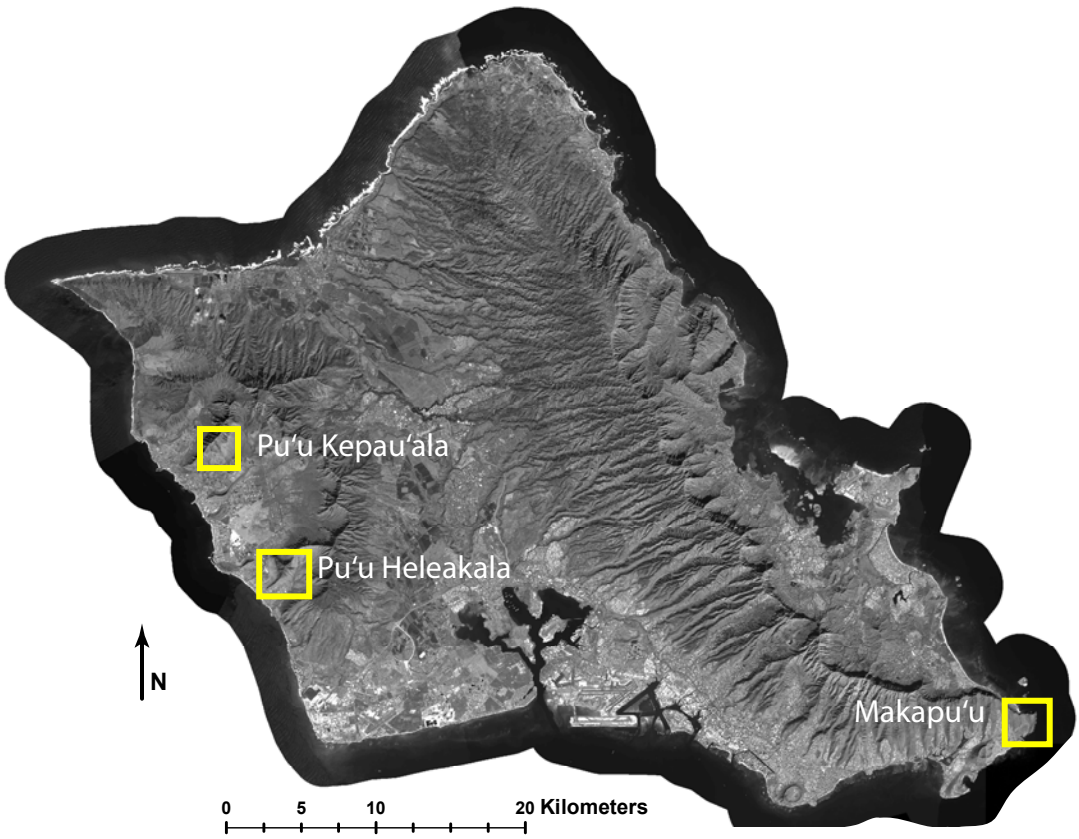

Figure 4.2 WorldView-2 composite image of O‘ahu, Hawai‘i.

WorldView-2 composite image of O‘ahu, Hawai‘i. Yellow boxes indicate fieldwork locations [*DigitalGlobe*].

flows collected by the Mars Reconnaissance Orbiter (MRO) High Resolution Imaging Science Experiment (HiRISE) camera [*McEwen et al., 2007*] to images of layered Hawaiian lava flows collected by IKONOS, concluding that the Martian layers were lava flows because outcrop textures and weathering expressions were similar to the terrestrial analog location. Here we use similar techniques to study lunar lava flows through analogs on O‘ahu, Hawai‘i. *Greeley* [1974a] recommended the use of terrestrial aerial images combined with ground-truthing fieldwork as an exercise for planetary scientists to improve their interpretations of planetary features. Emphasis was placed on the Island of Hawai‘i, where features of both active and past volcanism can be observed. *Rowland et al.* [2011] and *Mouginnis-Mark et al.* [2011] use the Island of Hawai‘i to teach a comparative planetary geology field course for early-career scientists. The course uses lava tubes and channels, collapse pits, and lava fountain deposits as analogs to basaltic features on the Moon and other planets. In addition, the origin and dynamics of lunar rilles, thought to be lava channels or collapsed lava tubes, have been investigated through comparative studies of these features in Hawai‘i [e.g., *Greeley*, 1971, 1974b; *Cruikshank and Wood*, 1972].

4.3.3 *Remote Sensing Data*

The Lunar Reconnaissance Orbiter (LRO) was launched on 23 June 2009 with the goal of orbiting the lunar surface and taking measurements that will aid in the return of humans to the Moon [*Vondrak et al.*, 2010]. LRO is equipped with seven instruments, including the Lunar Reconnaissance Orbiter Camera (LROC) and the Lunar Orbiter Laser Altimeter (LOLA). LROC consists of three cameras: two Narrow Angle Cameras (NAC)

and a Wide Angle Camera (WAC) for context imaging [*Robinson et al.*, 2010]. NAC cameras acquire high-resolution, panchromatic images at resolutions of ~ 0.5 m per pixel. The WAC camera acquires images in seven color bands at a scale of at about 100 meters per pixel. LOLA measures the elevation and roughness of the lunar surface at high resolution, with vertical accuracy of 10 cm and a horizontal accuracy of < 50 m [*Smith et al.*, 2010].

WorldView-2 (WV2), also launched in 2009, is a commercial Earth-observing satellite owned and operated by Digital Global that acquires panchromatic images at 0.5 m resolution and multispectral data in eight bands at 1.84 m resolution for use in terrestrial mapping and monitoring applications (http://www.satimagingcorp.com/). WV2 coverage of O‘ahu has similar emission angles (angle of the instrument boresight from the surface normal) and incidence angles (angle of solar vector from the surface normal) to those of the LROC images (see Tables 4.1, 4.2, and 4.3). For this study, we used panchromatic images as a terrestrial analog to the LROC NAC imagery as they provide data at similar resolutions. For topography, we used a DEM derived from USGS 7.5’ Quadrangles.

4.4 METHODS

4.4.1 *Definitions*

In the remote sensing images, a *layer* is defined as a natural, near-horizontal linear, curvilinear or sinuous feature in plan view, that can be traced laterally for some distance, and is roughly aligned with the contour of the local topography exposed along steep slopes. The identification of layers may be based on a change in the tone or texture

Crater	Location	Transect Number	NAC Image	Incidence Angle	Emission Angle	Elevation Change (meter)	Minimum Flow Count	Maximum Flow Count	Maximum Flow Thickness (meter)	Minium Flow Thickness
Kepler	S1	1	M193203725RC	74.41	9.21	57.0	3	6	19.01	9.50
		2	M193203725RC	74.41	9.21	59.0	2	6	29.48	9.83
		3	M193203725RC	74.41	9.21	100.2	12	16	8.35	6.26
		4	M193203725RC	74.41	9.21	42.2	2	4	21.08	10.54
		5	M193203725RC	74.41	9.21	30.2	2	7	15.08	4.31
		6	M188493098LC	20.96	1.75	88.6	8	17	11.08	5.21
		7	M188493098LC	20.96	1.75	120.3	7	19	17.18	6.33
		8	M188493098LC	20.96	1.75	59.8	4	8	14.95	7.48
		9b	M188493098LC	20.96	1.75	337.3	22	51	15.33	6.61
		9e	M111843702RC	32.61	1.16	337.3	14	41	24.09	8.23
		10	M155485087LC	6.74	1.67	24.0	6	9	4.00	2.67
		11	M155485087LC	6.74	1.67	138.2	10	27	13.82	5.12
		12	M129540425LC	57.34	1.68	31.0	5	11	6.19	2.81
		AVERAGE							**15.36**	**6.53**
	S3	1	M183775312LC	35.83	1.75	50.9	4	10	12.74	5.09
		2	M188493098LC	20.96	1.75	116.0	7	19	16.57	6.11
		3	M183775312LC	35.83	1.75	183.0	8	24	22.87	7.62
		AVERAGE							**17.39**	**6.27**
	N	1	M166093770RC	62.51	7.28	20.8	2	7	10.38	2.96
	NW	1	M107128381LC	24.62	1.76	38.8	3	9	12.95	4.32
		2	M107128381LC	24.62	1.76	41.9	3	8	13.98	5.24
		AVERAGE							**13.47**	**4.78**
	NNE	1	M173165404RC	20.76	1.16	220.0	10	32	22.00	6.87
	NEbN	1	M173165404LC	20.7	1.67	35.8	3	13	11.94	2.76
		2	M173165404LC	20.7	1.67	38.8	3	10	12.93	3.88
		3	M173165404LC	20.7	1.67	40.0	3	11	13.32	3.63
		AVERAGE							**12.73**	**3.42**
	NE	1	M173165404LC	20.7	1.67	16.8	2	4	8.38	4.19
		2	M173165404LC	20.7	1.67	22.9	4	6	5.72	3.81
		3	M173165404LC	20.7	1.67	29.8	3	10	9.95	2.98
		4	M173165404LC	20.7	1.67	16.5	2	7	8.26	2.36
		5	M173165404LC	20.7	1.67	32.7	5	15	6.53	2.18
		AVERAGE							**7.77**	**3.10**
	AVERAGE								**13.97**	**5.31**
	St. Deviation								**5.75**	**2.25**

Table 4.1 Summary of mapped layered deposits in LROC data.

Crater	Location	Transect Number	NAC Image	Incidence Angle	Emission Angle	Elevation Change (meter)	Minimum Flow Count	Maximum Flow Count	Maximum Flow Thickness (meter)	Minium Flow Thickness
Dawes	S	1	M190423336LC	45.54	8.03	157.257	6	15	26.21	10.48
		2a	M190423336LC	45.54	8.03	181.786	7	18	25.97	10.10
		2b	M113785646LC	55.67	1.68	181.786	7	43	25.97	4.23
		AVERAGE							**26.05**	**8.27**
	NNE	1	M175104387RC	44.18	1.15	37.238	6	12	6.21	3.10
		2	M157418698RC	25.11	1.16	47.065	4	12	11.77	3.92
		3	M157418698RC	25.11	1.16	108.18	4	7	27.05	15.45
		AVERAGE							**15.01**	**7.49**
	WWN	1	M168034554RC	44.15	1.15	19.189	5	16	3.84	1.20
	SWS	1	M142095883LC	25.98	1.68	68.518	5	13	13.70	5.27
	SSW	1a	M190423336LC	45.54	8.03	102.402	4	10	25.60	10.24
		1b	M113785646LC	55.67	1.68	102.402	7	17	14.63	6.02
		AVERAGE							**20.11**	**8.13**
	SE1	1	M157418698RC	25.11	1.16	147.7	13	37	11.36	3.99
		2	M175104387RC	44.18	1.15	116.87	11	38	10.62	3.08
		AVERAGE							**10.99**	**3.53**
	AVERAGE								**17.61**	**6.73**
	St. Deviation								**8.09**	**3.78**
Bessel	SSE	1a	M113839834RC	57.48	1.16	99.063	5	13	19.81	7.62
		1b	M135073175LC	63.79	1.68	99.063	8	21	12.38	4.72
		AVERAGE							**16.10**	**6.17**
	NE	1	M113839834RC	57.48	1.16	253.933	11	20	23.08	12.70
		2	M113839834RC	57.48	1.16	200.138	7	21	28.59	9.53
		3	M113839834RC	57.48	1.16	57.654	4	12	14.41	4.80
		AVERAGE							**22.03**	**9.01**
	AVERAGE								**19.06**	**7.59**
	St. Deviation								**6.04**	**3.09**
Lichtenberg	SSW	1	M1104002104RC	36.8	1.22	167.461	7	19	23.92	8.81
		2	M1104002104RC	36.8	1.22	82.732	4	11	20.68	7.52
		AVERAGE							**22.30**	**8.17**
	SSE	1	M1101644913RC	34.43	1.22	57.948	7	14	8.28	4.14
		2	M1104002104LC	36.7	1.77	58.247	4	11	14.56	5.30
		AVERAGE							**11.42**	**4.72**
	AVERAGE								**17.95**	**6.79**
	St. Deviation								**6.46**	**1.99**

Table 4.2 Summary of mapped layered deposits in LROC data, cont.

Table 4.3 Summary of mapped layered deposits in WorldView-2 data.

Location	WorldView-2 Image	Incidence Angle	Emission Angle	Transect	Elevation Change (meter)	Minimum Flow Count	Maximum Flow Count	Maximum Flow Thickness (meter)	Minium Flow Thickness
Pu'u Heleakalā	11JAN11213026-P3DM_R5C3-052390565220_01_P001	46.2	8.5	1	47	12	26	3.9	1.8
				2	161	16	32	10.1	5.0
	AVERAGE							**7.0**	**3.4**
	St. Deviation							**4.3**	**2.3**
Pu'u Kepau'ala	11JAN11213026-P3DM_R4C2-052390565220_01_P001	46.2	8.5	1	103	12	22	8.5	4.7
				2	52	6	13	8.7	4.0
				3	22	5	8	4.4	2.8
	AVERAGE							**7.2**	**3.8**
	St. Deviation							**2.4**	**1.0**
Makapu'u	11JAN11213026-P3DM_R6C9-052390565220_01_P001	46.2	8.5	Beach 1	17	6	11	2.8	1.5
				Beach 2	29	9	13	3.2	2.2
				Gorge	15	4	6	3.8	2.5
	AVERAGE							**3.3**	**2.1**
	St. Deviation							**0.5**	**0.5**

of surface with height in a transect, which may be the result of differences in the surface material, or the changing inclination of the surface with respect to the incident solar illumination. Alternately, the presence of shadows may define a layer, depending on emission angle (angle of the instrument boresight from the surface normal), incidence angle (angle of solar vector from the surface normal), and topography. Commonly, multiple layers form a *packet*, which is defined as a discrete group of layers that are laterally continuous for at least several meters and display a vertical succession in the imagery.

In a field setting, we use the term *outcrop* to describe a discrete vertical or near vertical succession of exposed rock, having no, or only minor, breaks in slope. An outcrop may contain one or more individual units. A *flow* or *flow unit* is used to describe an individual, distinguishable lava flow unit in the field. A flow unit is composed of one ʻaʻā flow, one pāhoehoe flow, or a series of overlapping pāhoehoe flows, likely emplaced in a single event, referred to as a complex pāhoehoe unit. A *trace unit* describes an *in situ* exposure, generally of a pāhoehoe flow, that does not have a measurable thickness. A trace unit is either found at the base of an outcrop, with no clear upper contact, or along low-sloping terrain between outcrops with no clear contacts. A *transect* refers to a profile ascending one or more packets or outcrops, perpendicular to slope contours, along which flows are counted in remote sensing data or measured in the field. In terrestrial data, these transects follow the uphill succession of lava flow units and are carefully matched between field and remote observations.

Figure 4.3 Step-like structure of Pu‘u Heleakalā.

Ridge at Pu‘u Heleakalā (PH2), O‘ahu, displaying step-like structure of outcrops. Arrows point to exposed outcrops. Layers are horizontal to subhorizontal with minor dipping due to emplacement slope. Visible peak is ~ 450 m above sea level. Photograph taken at ~ 50 m above sea level, 1 km from peak. Photograph courtesy of David Trang.

4.4.2 *Identifying Flows in Remote Sensing Data*

Terrestrial study sites were chosen primarily based on accessibility in the field, considering property ownership and navigability of steep ridge slopes. Transects were selected that had sufficiently shallow slopes for safe ascent, but also sufficiently steep to exhibit 'step-like' outcrop exposure created by breaks in slope (Figure 4.3). Transect slopes in both terrestrial and lunar data varied between 20° and 40°. Additionally, localities were sought that were clearly visible in satellite images and not obscured by shadows or vegetation. Flow layers were mapped in images by the identification of linear to sinuous features marked by a change in tone or texture, or a steep slope indicated by a shadow. In WorldView-2 images, dark layers were interpreted to be basalt flows exposed in sub-vertical cross-section; the dark outcrops stand in contrast against the lighter-toned vegetation growing on the shallower slopes between outcrops. Many areas do not show extensive continuous lateral layers or consistent vertical sequences, adding difficulty to the identification of layers. Flow morphology (i.e., 'a'ā vs. pāhoehoe) cannot be distinguished in remote sensing images. Height measurements for terrestrial images were made using a USGS 7.5' Quad-derived DEM.

In NAC images of layered sequences exposed in impact crater walls, the layers are identified by their steep slopes and knobby textures, and are generally indicated by laterally continuous zones of shadowing or a change in tone or texture. Transects were analyzed in ArcGIS (www.esri.com) in areas where LOLA tracks overlapped clear, layered packets in NAC images. LOLA shot points were selected at the top and bottom of the transect. The elevation difference between two shots defining the height of the transect was divided by the number of layers identified within the packet to determine

average flow thickness for a given packet.

For both lunar and terrestrial data sets, given that identifying individual layers is a rather subjective method, two investigators mapped the flows independently to increase precision and to ensure a thorough survey of possible flow layers. Investigators mapped 'clear' layers and, in most locations, 'uncertain' layers, the latter constituting features that were not laterally continuous or displayed only minor changes in tone or texture. The numbers of 'clear' layers identified in the maps of both investigators, referred to as *coincident layers*, give the minimum number of layers in a transect (Tables 4.1, 4.2, and 4.3). Coincident, non-coincident, and layers marked as 'uncertain' were used to derive the maximum possible number of layers in a given packet.

4.4.3 *Identification of Flows in the Field*

'A'ā and pāhoehoe flows erode in different ways and to different extents, producing variations in outcrop expression. Whereas it is difficult to determine flow type in spaceraft images, the distinction between different flow types observed in the field was made based on vesicle size and density, and textural features (Figure 4.4). Pāhoehoe flows are vesicle-rich with relatively evenly distributed spherical vesicles. 'A'ā flows have fewer, larger vesicles that are commonly sheared in the direction of flow. These two populations of vesicles are easy to distinguish in the field. The identification of 'a'ā versus pāhoehoe was confirmed by exposed contacts between flows. 'A'ā contacts show clear clinker/rubble layers, though the unconsolidated layers erode more quickly than the core, which leads to recessive layers versus resistant cores. Pāhoehoe contacts tend to have thin, glassy upper crusts and commonly have 'baked' material directly beneath the

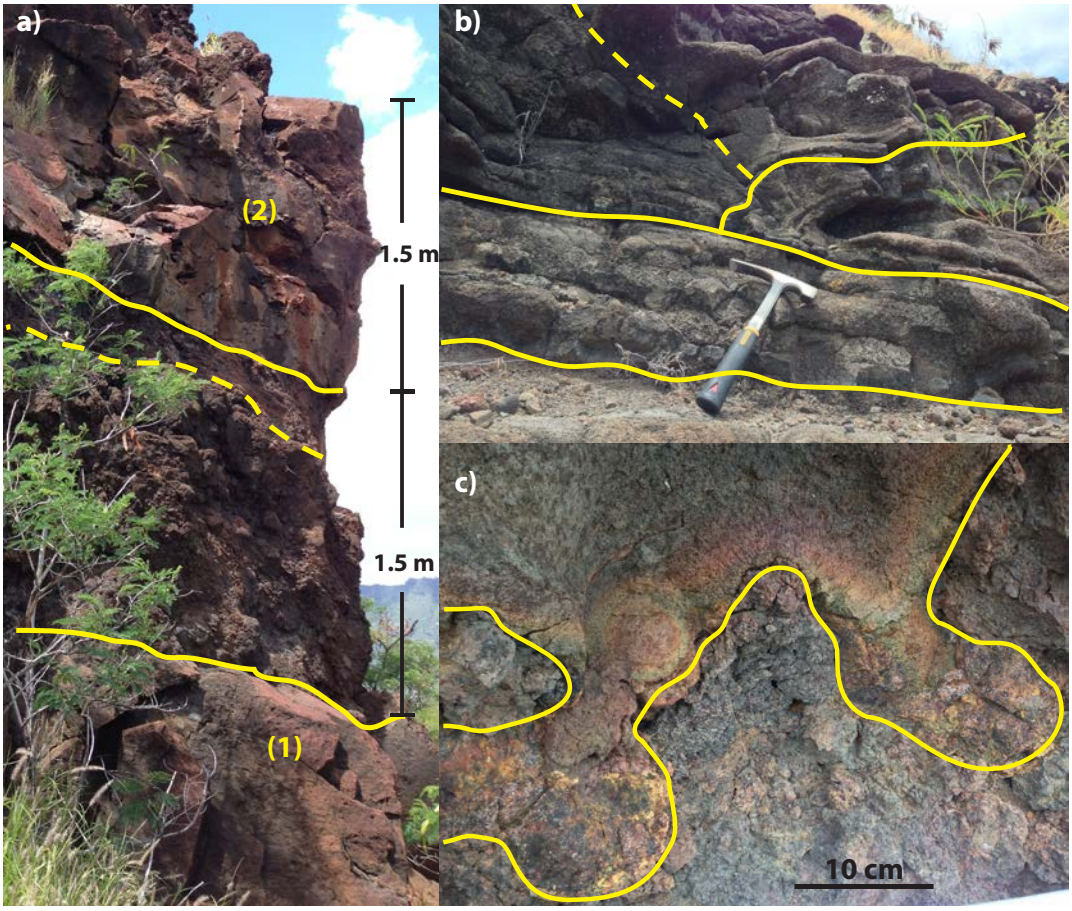

Figure 4.4 Selection of field photographs.

Selection of field photographs. a) Two ʻaʻā layers at Puʻu Heleakalā. Cores of flows (1) and (2) display knobby texture and low vesicularity. Contacts between cores and clinker layer are marked with solid yellow line. Likely contact between upper clinker layer of (1) and lower clinker layer of (2) marked with dashed yellow line. b) Complex pāhoehoe unit at Makapuʻu Beach Transect. Small pāhoehoe lobes commonly overlap at sub-meter scales. These lobes were likely emplaced during a single flow event and are counted as a single flow unit. c) Pāhoehoe toes protruding into ʻaʻā clinker at Makapuʻu Gully. Contact marked by solid red line.

flow, as indicated by discolored or sintered rims on the underlying deposits.

Non-channelized pāhoehoe flows are generally emplaced as a series of small, overlapping flow lobes that inflate after emplacement [e.g. *Hon et al.*, 1994] and, as a result, individual flow lobes were difficult to distinguish in exposed outcrops of pāhoehoe units (Figure 4.4). The numbers and thicknesses of individual pāhoehoe flow lobes varied greatly within individual outcrops. These units are defined as complex pāhoehoe units and counted as one flow unit. Individual pāhoehoe flows are distinguishable by clear upper and lower contacts or crusts.

In the classification of ʻaʻā flows, each discrete core was counted as one flow. The total thickness of each flow was reported as the sum of the ʻaʻā core and any visible upper and lower clinker. When two ʻaʻā flows were stacked in a vertical succession, the two clinker layers in between the two flow cores were typically indistinguishable, so one half of the total thickness of the intervening clinker was added to each flow measurement to derive the respective total thicknesses. Total thicknesses of an individual ʻaʻā flow may vary by up to tens of cm at the outcrop level, however the thickness of the clinker layers can vary by tens of cm to ~1 m in an outcrop, displacing some of the core material and changing the ratio of core to clinker within a single unit. However, these variations do not greatly affect the total thickness of the flow unit. Thickness measurements were taken with a 50 m measuring tape and contain an uncertainty of approximately ± 0.1 m due to local variability in flow thickness. A handheld Global Positioning System (GPS) unit was used to record the location of each flow mapped and to correlate field location with locations in images.

4.5 RESULTS

4.5.1 *Lunar Image Analysis*

For this investigation we selected fresh impact craters within the nearside mare basins with well-exposed layering in the walls observable in NAC images (Figures 4.5 – 4.8). Lunar image observations are summarized in Table 4.1.

Kepler Crater (32 km diameter, 2.6 km deep; Figure 4.5) is a young crater [*Wilhelms and McCauley*, 1971] located in Oceanus Procellarum (8.12° N, 38.01° W, Figure 4.1). Layers were mapped in LROC NAC images along 27 transects in seven regions (see Table 4.1) along the crater wall, revealing an average layer thickness (transect elevation change divided by number of flows identified along transect) for all 27 transects within Kepler Crater ranging between 5.2 m (standard deviation σ = 2.4) and 13.9 m (σ = 6.1m). At each transect, minimum and maximum average layer thicknesses were calculated by dividing the height of a transect by the maximum and minimum, respectively, flow counts (see Table 4.1). For example, the elevation change over Kepler transect S1-1a is 57 m, this elevation is divided by 3 (the minimum number of interpreted flows) to get a maximum average flow thickness of 19.0 m and then divided by 6 (the maximum number of interpreted flows) to get a minimum average flow thickness of 9.5 m. Layers at Transect 9 in the Kepler S-1 area were mapped twice, using two images having different illumination conditions and viewing geometries (NAC M188493098LC (S1-9b) and NAC M111843702RC (S1-9e)). The derived average thicknesses varied significantly between the two images, resulting in minimum and maximum flow thickness measurements varying by factors of 1.2 and 1.6, respectively, indicating that

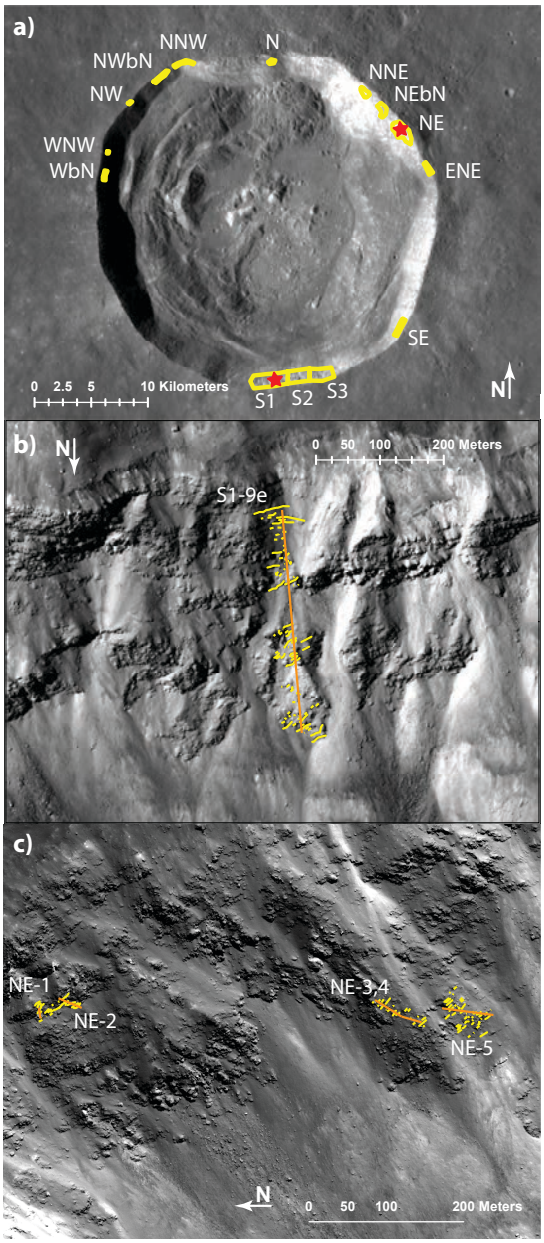

Figure 4.5 Mosaic of Kepler Crater.

a) LROC WAC mosaic of Kepler Crater. Yellow boxes indicate regions where layered lava sequences appear in LROC NAC images (Table 4.1). Red stars show locations of insets. b) Portion of LROC NAC image M111843702RC. Image is of Transect 9e in Location S1. Average layer thicknesses range from 2.7 to 29.5 m thick in this location. Solid lines map 'clear' layers, dashed lines map 'uncertain' layers. c) Portion of LROC NAC image M173165404LC, displaying layered basalt sequences. Image shows the NE Location, Transects 1–5 . Average layer thicknesses in this region range from 2.2 to 10.0 m thick [*NASA/GSFC/Arizona State University*].

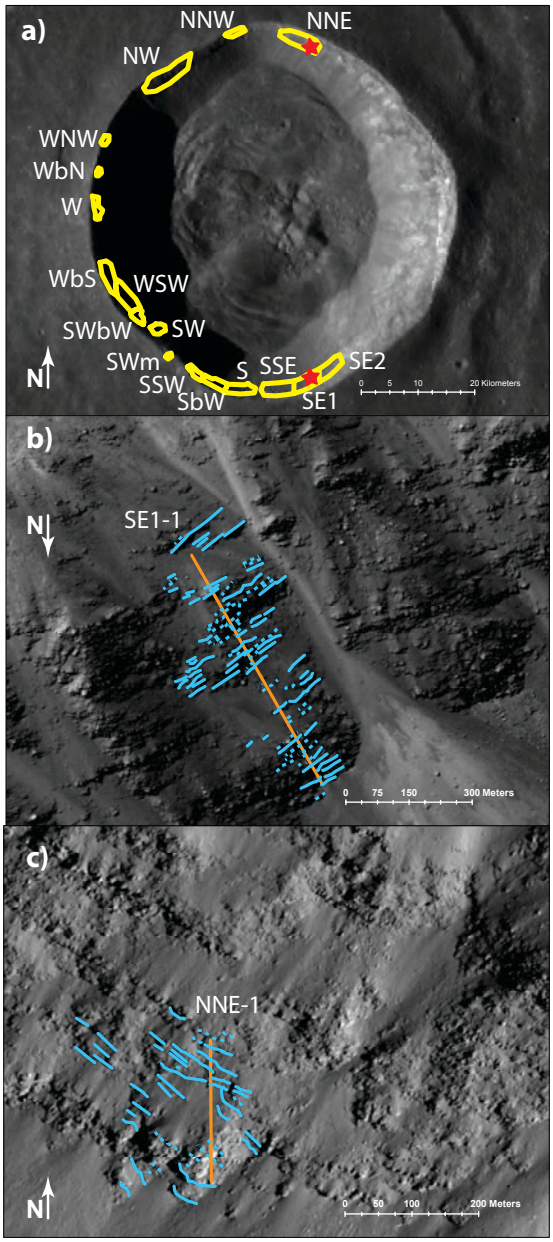

Figure 4.6 Mosaic of Dawes Crater.

a) LROC NAC and WAC mosaic of Dawes Crater. Yellow boxes indicate regions where layered lava packets appear in LROC NAC images (Table 4.2). Red stars mark locations of (b) and (c). b) Portion of LROC NAC image M157418698RC. Image shows Location SE1, Transect 1. Average layer thicknesses in this region range from 3.1 to 11.4 m. Solid lines mark 'clear' layers, dashed lines mark 'uncertain' layers. c) Portion of LROC NAC image M175104387RC, displaying layered basalt packets. Image shows Location NNE, Transect 1. Average layer thicknesses range from 3.1 to 27.1 m in this location [*NASA/GSFC/Arizona State University*].

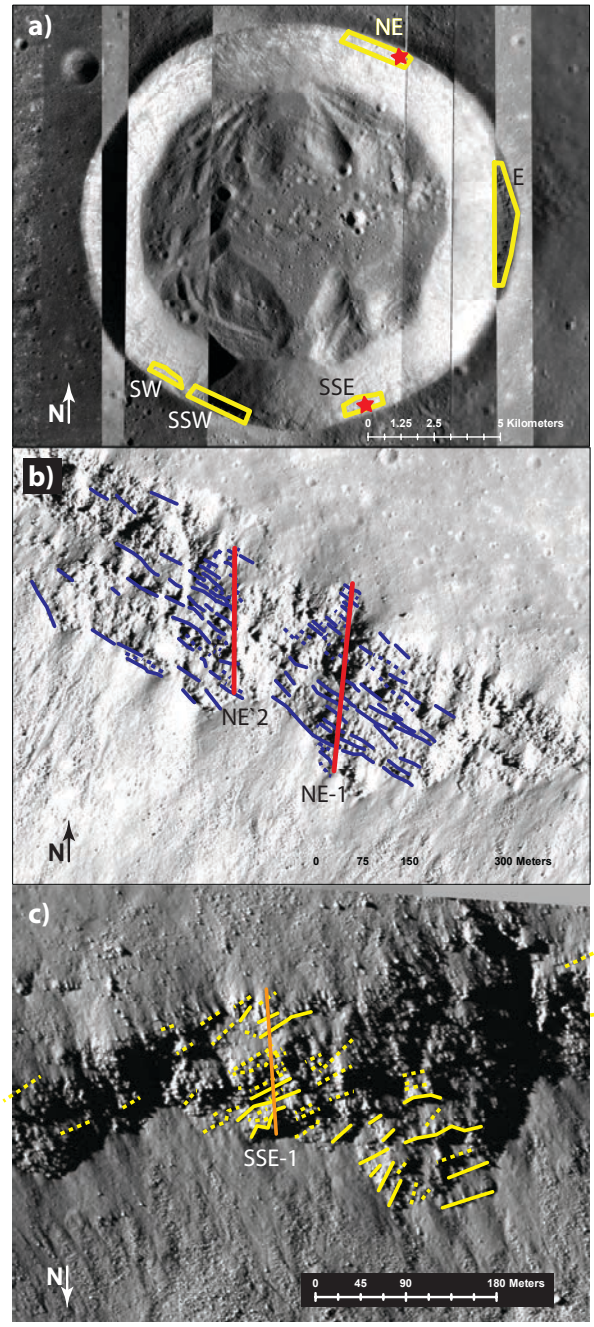

Figure 4.7 Mosaic of Bessel Crater.

a) LROC NAC and WAC mosaic of Bessel Crater. Yellow boxes indicate regions where layered lava packets appear in LROC NAC images (Table 4.2). Red stars mark locations of (b) and (c). b) Portion of LROC NAC image M113839834RC, showing the NE Location, Transects 1 and 2. Average layer thicknesses in this region range from 4.8 to 28.6 m. Solid lines mark 'clear' layers, dashed lines mark 'uncertain' layers. c) Portion of LROC NAC image M113839834RC, showing the SSE Location, Transect 2. Average layer thicknesses range from 4.7 to 19.8 m in location [*NASA/GSFC/Arizona State University*].

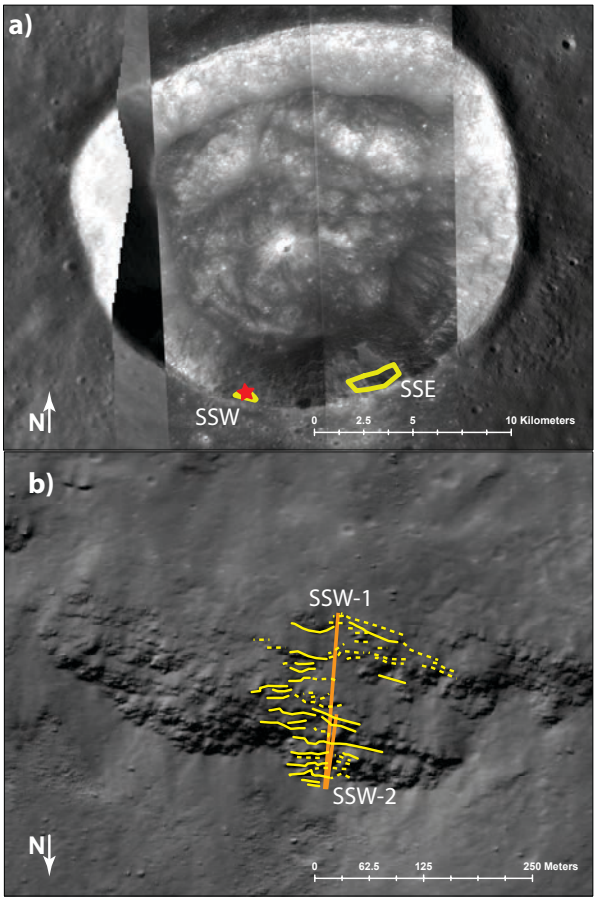

Figure 4.8 Mosaic of Lichtenberg Crater.

a) LROC NAC and WAC mosaic of Lichtenberg Crater. Yellow boxes indicate regions where layered lava packets appear in LROC NAC images (Table 4.2). Red star marks location of (b). b) Portion of LROC NAC image M1104002104RC, showing the SSW transects. Average layer thicknesses in this region range from 7.5 m and 23.9 m [*NASA/GSFC/Arizona State University*].

mapping flow thicknesses accurately is a function of viewing geometry and lighting.

Dawes Crater (18 km diameter, 2.3 km deep; Figure 4.6), is located between Maria Serenitatis and Tranquillitatis at 17.6° N, 26.34° E (Figure 4.1). LOLA profiles overlapped NAC images of layered packets along ten transects in six areas, displaying an average layer thickness between 6.4 m (σ = 4.2 m) and 16.9 m (σ = 8.7 m) (Table 4.2). Two transects, S-2 and SSW-1 were each mapped twice using different NAC images (M190423336LC (S-2a) and M113785646LC (S-2b), and M190423336LC (SSW-1a) and M113785646LC (SSW-1b), respectively). Details are given in Table 4.2. At transect S-2, the maximum average thickness does not change and minimum average thickness varies by a factor of 2.4 between the two images. At SSW-1, maximum and minimum average thicknesses change by a factors of 1.75 and 1.7, respectively.

Bessel Crater (16 km diameter, 1.7 km deep; Figure 4.7) is located in Mare Serenitatis at 21.73° N, 17.92° E (Table 4.2). At Bessel, layered packets were counted along four transects at two locations, with an average layer thickness ranging from 7.9 m (σ = 3.4 m) to 19.7 m (σ = 6.6 m) (Table 4.2). Repeated flow counts at the same location using two images (NAC M113839834RC (SSE-1a) and NAC M113839834RC (SSE-1b)) reveal maximum and minimum thicknesses differing by factors of 1.6 (Table 4.2).

Lichtenberg Crater (20 km diameter, 1.2 km deep; Figure 4.8) is a young crater with high albedo located in Oceanus Procellarum (31.85°N, 67.72°W; Figure 4.1). At Lichtenberg, LOLA imagery overlapped with clear NAC images in four transects within two regions, with an average layer thickness between 6.4 m (σ = 2.1 m) and 16.9 m (σ = 6.9 m) (Table 4.2). Transects SSW-1 and SSW-2 follow two near vertical sections within the same flow packet, and were mapped in the same NAC image

(M1104002104RC). Similar average flow thicknesses were calculated for the two transects, implying lateral continuity of layering (Table 4.2).

4.5.2 *Terrestrial Image Analysis*

Pu‘u Heleakalā (Figure 4.9) is composed primarily of lava flows with an exposed cinder cone from the main shield stage of Wai‘anae Volcano [*Sherrod et al.*, 2007]. It is characterized by thin (< 5 m) ‘a‘ā and pāhoehoe flows. It is located just to the south of the southern edge of the inferred caldera and displays shallow southward sloping flows with dikes intruded from the caldera complex [*Sherrod et al.*, 2007]. Layers were mapped over wide regions at proposed field sites prior to fieldwork and exact transect paths were determined upon arrival at the location. We classified flow units along two transects at different locations on Pu‘u Heleakalā. Transects will be referred to as Pu‘u Heleakalā 1 (PH1) and Pu‘u Heleakalā 2 (PH2). Results are summarized in Table 4.3. At PH1, a minimum of 12 layers and a maximum of 26 layers were identified independently by two of the authors along a transect covering an elevation range of 47 m in WorldView-2 images, revealing minimum and maximum average thicknesses of 1.8 and 3.9 m, respectively. At PH2, image analysis by two mappers revealed 16–32 layers over a 161 m vertical transect, with average thicknesses between 5.03 and 10.06 m.

Pu‘u Kepau‘ala (Figure 4.10) lavas were emplaced during the late-shield caldera-filling stage of Wai‘anae Volcano, encompassing ponded inter-caldera flows and adjacent flank flows [*Sherrod et al.*, 2007]. The geologic unit comprising this ridge is characterized by pāhoehoe and ‘a‘ā flows containing plagioclase phenocrysts [*Sherrod et*

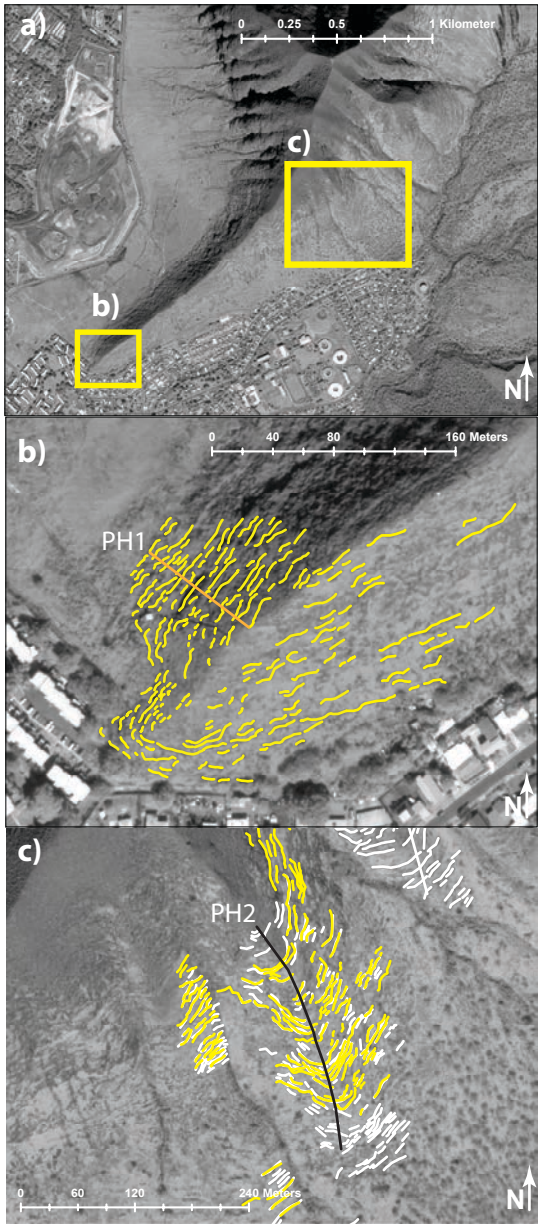

Figure 4.9 WorldView-2 image of Pu‘u Heleakalā.

a) WorldView-2 image of Pu‘u Heleakalā located in the Wai‘anae Range, O‘ahu (Figure 4.2). Insets show b) transect PH1 and c) transect PH2 where lava flow units were mapped (Table 4.3). The mean thickness of flows measured in the field at Pu‘u Heleakalā was 1.6 m (σ = 0.8 m) (Table 4.4). Image interpretations provided minimum and maximum average flow thicknesses of 3.9 m (σ = 1.6 m) and 7.0 m (σ = 4.4 m) [Image credit: *DigitalGlobe*].

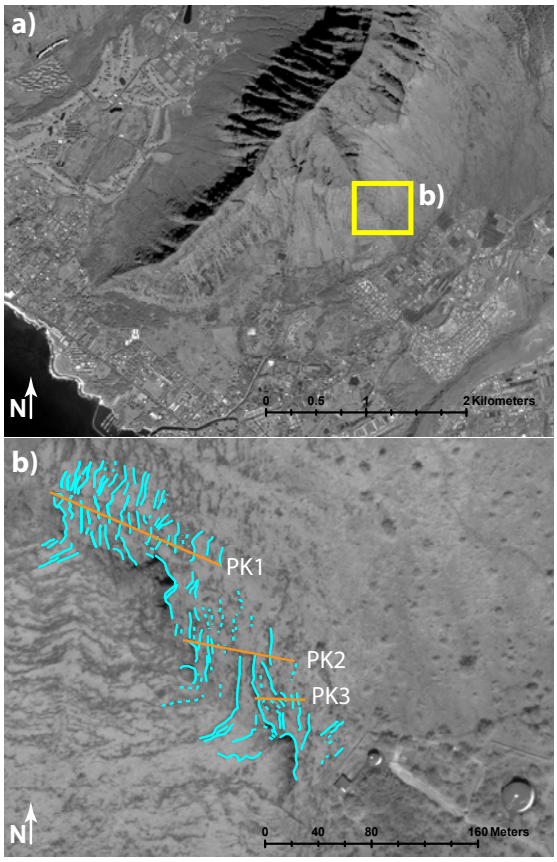

Figure 4.10 WorldView-2 image of Pu‘u Kepau‘ala.

a) WorldView-2 image of Pu‘u Kepau‘ala located in the Wai‘anae Range, O‘ahu (Figure 4.2). Pu‘u Kepau‘ala marks the northern extent of ancient caldera of Wai‘anae Volcano. Box marks location of (b). (b) Lava flow units were mapped in the field along three transects on the northeast side of the ridge revealing a mean flow thickness of 1.8 m (σ = 1.0 m) (Table 4.4). Image interpretations revealed minimum and maximum average flow thicknesses of 3.8 m (σ = 1.0 m) and 7.2 m (σ = 2.4 m) m (Table 4.3). Solid lines mark ‘certain’ layers, dashed lines mark ‘uncertain’ layers [Image credit: *DigitalGlobe*].

al., 2007]. Flow units were classified along three transects at Puʻu Kepauʻala, referred toas Puʻu Kepauʻala 1 (PK1), Puʻu Kepauʻala 2 (PK2), and Puʻu Kepauʻala 3 (PK3) (Table 4.3). Along PK1, a minimum of 12 and a maximum of 22 layers were identified by two mappers along a vertical elevation of 102.5 m in WorldView-2 (WV2) imagery, giving minimum and maximum average layer thicknesses of 4.7 and 8.5 m, respectively. At PK2, between 6 and 13 layers were mapped over 52 m vertically, with minimum and maximum average thicknesses of 4.0 and 8.7 m. Mapping of PK3 revealed average thicknesses ranging from 2.8 to 4.4 m for the 5 – 8 flows identified over an elevation change of 22 m.

Makapuʻu Point, in Eastern Oʻahu (Figure 4.11), displays clear outcrops of distal shield-stage flows from Koʻolau Volcano, dipping generally south [*Sherrod et al.*, 2007]. We classified flow units along three short transects in this area, referred to as Makapuʻu Gully (MG), Makapuʻu Beach 1 (MB1), and Makapuʻu Beach 2 (MB2) (Table 4.3). At MG, WV2 imagery revealed 4–6 layers over an elevation change of 15 m, with minimum and maximum average thicknesses of 2.50 and 3.75 m. At MB1, 6–11 layers were mapped over an elevation change of 17 m, with an average thickness ranging between 1.55 and 2.83 m. Mapping of MB2 revealed 9–13 layers over an elevation change of 29 m, giving average thicknesses of 2.23 and 3.22 m (Table 4.3).

4.5.3 *Field Observations*

Lava flow outcrops were investigated along nine transects at three field locations on Oʻahu (Table 4.4). In general, near vertical outcrops are separated by < 1 to 5 m of gently sloping vegetation-covered talus. Gently sloping areas are the result of erosion of

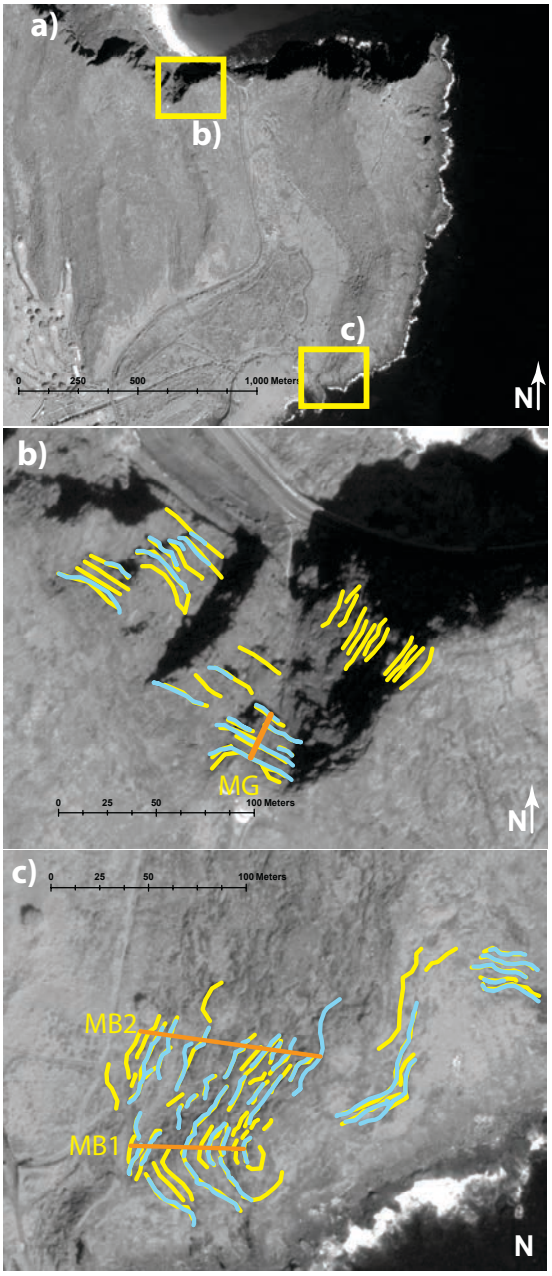

Figure 4.11 WorldView-2 image of Makapu‘u Point.

a) WorldView-2 image of Makapu‘u Point located in Eastern O‘ahu (Figure 4.2). Boxes show b) Makapu‘u Gully transect, and c) Makapu‘u Beach transect 1 and 2, where lava flow units were mapped. Mean thickness of *in situ* flows measured in the field was 2.0 m (σ = 1.2 m) (Table 4.4). Image interpretations provided minimum and maximum average flow thicknesses of 2.1 m (σ = 0.5 m) and 3.3 m (σ = 0.5 m) (Table 4.3) [Image credit: *DigitalGlobe*].

Location	Transect Number	Outcrop Count	Flow Count	Number Pāhoehoe, ʻAʻā, Other	Mean Flow Thickness (meter)	Ratio Max. Satellite/Field Flow Thickness	Ratio Min. Satellite/Field Flow Thickness
Puʻu Heleakalā	1	8	12	7,5,0	1.5	2.7	1.2
	2	39	64	25,34,3 (cinder)	1.6	6.3	3.1
	AVERAGE				**1.6**	**4.5**	**2.2**
	St. Deviation				**0.8**	**2.5**	**1.3**
Puʻu Kepauʻala	1	18	29	16,13,0	1.7	5.1	2.8
	2	13	24	18,6,0	1.9	4.5	2.1
	3	8	10	7,3,0	2.7	1.6	1.0
	AVERAGE				**1.8**	**3.8**	**2.0**
	St. Deviation				**1.0**	**1.9**	**0.9**
Makapuʻu	Beach 1	6	12	8,4,0	1.4	2.0	1.1
	Beach 2	7	10	6,3,1 (cinder?)	2.6	1.3	0.9
	Gully	5	7	5,2	2.4	1.5	1.023
	AVERAGE				**2.0**	**1.6**	**1.0**
	St. Deviation				**1.2**	**0.4**	**0.1**

Table 4.4 Summary of field observations.

more readily weathered materials within the flow unit sequence, commonly exhibiting exposures of flow surfaces, discontinuous basalt rubble, or are featureless. Dense ʻaʻā cores tend to weather slowly, producing prominent outcrops. Roughly half of the outcrops visited contain more than one flow unit. Upper clinker layers are commonly completely eroded while lower clinker layers and clinker layers between two sequential ʻaʻā cores remain *in situ*. In general, individual pāhoehoe flows thicker than ~ 0.5 m are resistant to erosion and form vertical outcrops. Complex pāhoehoe units (i.e., several overlapping flow lobes each tens of centimeters thick) erode readily, commonly forming low-relief rubbly surfaces that may not be obviously *in situ*. Talus and vegetation commonly cover the lower portion of outcrops, obscuring the lower contacts. The lack of identification of lower contacts, together with erosion of upper clinker layers, may have led to underestimation of the thickness of the originally emplaced lava flow.

Lava flow units were mapped in the field along the same three transects mapped in WV2 imagery at Puʻu Heleakalā (Figure 4.9). At PH1, 12 flows were counted, 11 with measurable thicknesses and one trace unit within eight outcrops, with a mean flow thickness of 1.5 m (σ = 1.2 m) (Table 4.4). Minimum and maximum thicknesses derived from image interpretations at PH1 were 1.2 and 2.7 times as thick as the mean field measurement. Exact correlation between field and image transects was not possible at this location due to inherent GPS inaccuracies, resulting in an image transect that covered a larger vertical succession and a higher layer count than in the field transect. At PH2, 64 flow units were counted, including three cinder deposits, in 39 outcrops. A maximum of 32 layers were identified along this transect in WV2 images (Table 4.3). We found a mean thickness of 1.6 m (σ = 0.7 m) among 55 units with measurable thicknesses. Nine

units were trace units in outcrops or *in situ* pāhoehoe exposures on low sloping terrain lacking clear contacts. The ratio of the average thicknesses interpreted using WV2 images to mean field measurements is 3.1 to 6.3 at PH2 (Table 4.4).

Flow units were mapped at three transects in the field at Puʻu Kepauʻala (Figure 4.10). Along Transect 1 (PK1), 29 flow units, 27 of which had measurable thicknesses, were classified in 18 outcrops revealing a mean flow thickness of 1.7 m (σ = 0.6 m) (Table 4.4). Minimum and maximum thicknesses derived from WV2 image interpretations at PK1 were 2.8 and 5.1 times as thick as the mean field measurement. Within 13 outcrops, 24 lava flow units were counted, and 22 were measured along transect PK2. The resulting mean unit thickness of 1.9 m (σ = 1.3 m) reveals image interpretation to field measurement thickness ratios of 2.1 to 4.5. At PK3, ten flow units were counted within eight outcrops. The seven measurable units had a mean flow thickness of 2.7 m (σ = 2.0 m). The ratio of the average thicknesses interpreted using WV2 images to mean field measurements is 1.0 to 1.6 at PK3.

We classified lava flow units along three transects at two locations near Makapuʻu Point (Figure 4.11). At Makapuʻu Gully (MG), seven flows, with a mean unit thickness of 2.44 m (σ = 1.1 m) were counted in five outcrops (Table 4.4). Average thicknesses measured in WV2 images are 1.0 to 1.5 times as thick as the mean field measurement at MG. Along MB1, 12 lava flow units were counted. A mean thickness of 1.39 m (σ = 0.8 m) was measured for 11 flow units within six outcrops. The ratio of the average thicknesses interpreted using WV2 images to mean field measurements is 1.1 to 2.0 at MB1. Seven outcrops revealed eight flow units, including two trace units, at MB2, with a mean flow thickness of 2.56 m (σ = 1.4 m) for the six flows identified. Average

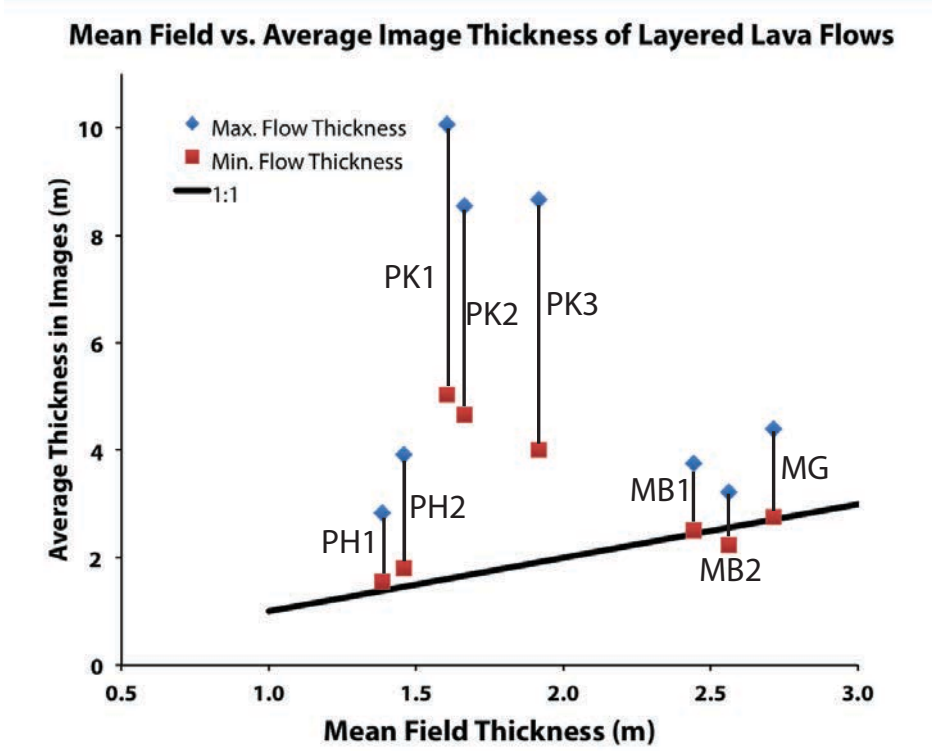

Figure 4.12 Mean field vs. average image thicknesses.

Mean field thicknesses plotted versus average thicknesses derived from image interpretations for each terrestrial transect (Tables 4.3 and 4.4). For each transect, maximum (blue diamonds) and minimum (red squares) average flow thicknesses are connected. Most of the thicknesses determined from WV2 images lie above the one-to-one line, representing overestimates in flow thicknesses. Symbols lying on the line indicate correct image-based interpretation of flow thicknesses.

thicknesses measured in WV2 images are 0.9 to 1.3 times as thick as the mean field measurement at MG. MB2 is the only site measured with more (thinner) layers interpreted from WV2 images than measured in the field.

4.6 DISCUSSION

4.6.1 *Image interpretation vs. field observations*

In this study, we find that lava flow thickness estimates derived from terrestrial satellite images are generally greater than thicknesses measured in the field (Table 4.4, Figure 4.12). The overestimated thicknesses result from an inability to identify many of the individual flow contacts in the remote sensing data. One third to one half of the outcrops measured in the field contained more than one lava flow unit, which were not discernable in the images. At the O‘ahu field sites, changes in slope along a lava flow sequence occur at layers that are more easily weathered, such as ‘a‘ā clinker layers and thin pāhoehoe flows. Dense ‘a‘ā cores and thick pāhoehoe flows are more resistant to weathering, creating stepped, sub-vertical outcrops. Pāhoehoe and clinker layers between or below ‘a‘ā cores tend to be protected by the dense layers and are often found in outcrop with the denser layers. Additionally, given that thin pāhoehoe flows are easily weathered, they can be mistaken for rubble in low-slope terrain between vertical outcrops, and are only identified in the field upon close inspection. These flows were commonly not distinguishable in satellite images. In the image interpretations, each missed pāhoehoe flow, and each outcrop containing multiple flows that is counted as one flow, will both increase the interpreted average flow thickness for a given transect because the total

elevation change will be divided by a number smaller than the true flow count. Therefore, measurements of layered basalt flows interpreted from remote sensing data provide a minimum count of the number of lava flows in a transect, and consequently, a maximum thickness for the flows. Actual mare flow thicknesses may be smaller than those observed in LROC images (between 1.2 and 29.5 m in this study and 3 – 14 m in Robinson et al. [2012]) by factors of up to 6.3.

The two locations with the largest overestimation of flow thickness in satellite image interpretations (PH2 and PK1,Table 4.3) also had the highest proportions of ʻaʻā flows (Table 4.4), further supporting our argument that the presence of ʻaʻā flows impedes accurate predictions of lava flow thickness in remote sensing images. Sequences of pāhoehoe flow units, including complex pahoehoe units, may result in more accurately predicted flow thicknesses in remote sensing imagery because they weather more readily at their contacts.

Sequences of exposed lunar lava flows may show erosional patterns similar to terrestrial flows. Although water and wind erosion do not degrade exposures on the Moon, gravitational forces and meteorite and micrometeorite impacts will erode the exposed surfaces of lava flows in outcrop, though at a much slower rate than weathering on the Earth. If present, the cores of ʻaʻā-like flows and thick pāhoehoe flows will be more resistant to weathering by impacts and gravitational erosion than unconsolidated clinker layers and thin or complex pāhoehoe units. Therefore, it can be inferred that shadowing created by changes in slope seen in LROC images of basalt sequences are the result of various responses to weathering and gravitational erosion by characteristic flow types. Improved knowledge of lava flow emplacement processes would allow for better

assessments of thickness measurement accuracies.

For our field measurements, the mean flow thicknesses are calculated as the mean of all the flow units measured across the transect. For PH3, the mean thickness of the 55 measurable flows in the field is 1.7 m (σ = 0.7 m). For comparison with this result, the average flow thickness can also be calculated by dividing the total elevation change over the transect (160 m, as measured by GPS and confirmed by topographic data) by the number of flows (including trace flows) counted (64 at PH3), the method used for the image data. This method gives an average flow thickness of 2.5 m. The difference between the two averages suggests that, in the field, some flow units within the section are missed and not counted. Missed flow units are likely flows that have eroded past the point of recognition or thin flows, which would further reduce the average flow thickness measurement. The variation between the averages may also be due, in part, to erosion of exposed outcrops and the natural variability of lava flow thickness within individual outcrops which will decrease the thickness of individual flows measured.

In the interpretation of lava flow thicknesses exposed in impact crater walls, three assumptions are made regarding impact crater morphology. (1) Flow sequences are not counted twice due to repetition of overturned strata. Commonly, during the formation of impact craters, the upper strata are ejected as a coherent 'flap' that overturns and is emplaced on top of the uplifted surface around the crater [*Shoemaker*, 1960, 1963; *Kring*, 2007]. At lunar study sites, overturned strata may expose lava packets that are repeated near the rim of the crater. Although such repetition could lead to bias toward thicknesses of double-counted strata, the overturned flap is only in the upper portion of the crater wall; transects in this study lie below the region where overturned strata might occur. In

addition, overturned strata is unlikely to be coherent and extensive collapse of the initial crater rim immediately after formation will likely reduce the prevalence of overturned strata [*Melosh*, 1989; *Sharpton*, 2014]. (2) We assume the layers we are counting are horizontal. Strata around an impact crater will be uplifted to some extent during the cratering process, leaving previously horizontal bedding dipping away from the crater center [*Melosh*, 1989]. Additionally, although likely producing less significant effects, beds may be tilted due to the original slope of emplaced flows or to regional tectonism. However, any bedding that is not horizontal or that is not intersected perpendicularly will exhibit a section with a vertical dimension greater than the thickness of the originally horizontal layer, further supporting the argument that mare basalt thickness measurements taken from exposures in the walls of impact craters are overestimates. (3) Flow units have not been significantly disrupted in the cratering process. Strata around an impact crater may be shocked and deformed from the high energy of the impact [*Shoemaker*, 1960, 1963; *Melosh*, 1989]. Here, we assume the shock of the impact has not significantly changed the original morphology of the observed layers. Additionally, material may be injected into existing strata during the excavation stage of crater formation. Injection of material will disrupt original stratigraphy and increase the rim height of the crater [*Sharpton*, 2014]. Injection may also increase the apparent thickness of a given packet measured in this study, thereby contributing toward overestimation of average lava flow thicknesses. For our purposes, we assume individual transects to not include injected layers cannot discern such layers from uplifted strata in crater walls.

In identifying individual lava flows in lunar and terrestrial imagery, different methods are used to distinguish individual layers depending on incidence angles and on

local slopes. Layered sequences observed in images acquired at high incidence angles (sun low in the sky) may be distinguished by shadows, indicating steep slopes. In contrast, layers seen in lower incidence-angle images (sun high in the sky) may be distinguished by change in tone or texture, resulting from a change in surface material type (e.g. rock vs. vegetation) or material properties (e.g. solid rock vs. rock talus), also reflecting changes in slope. Image clarity, resolution, and incidence angles should affect the number of discernible layers in a given packet. Transects S1-9 in Kepler Crater, S-2 and SWW-1 in Dawes Crater, and SSE-1 in Bessel Crater were each analyzed in more than one image. The counts for the same transects using different images were significantly different (Tables 4.1 and 4.2). For three of the four repeated counts, the image with the higher incidence angle produced higher layer counts. This implies that higher incidence angles are favorable for capturing the breaks in slope used to identify lava layers in NAC images because the sun is closer to the horizon and changes in orientation of surfaces with respect to solar illumination direction produce more dramatic changes in surface tone. The effect of emission angle was less consistent, the higher emission angle produced higher counts for two transects and lower counts for two transects. A larger data set might reveal a correlation between emission angle and clarity of features in remote sensing data. WorldView-2 images have incidence and emission angles similar to LROC images (Table 4.3). It is likely that higher incidence angles will also be favorable for accurately counting layered deposits in terrestrial imagery.

4.6.2 *Mapper experience*

This study used two mappers with different experience levels. At the beginning

of the field study, M. Elise Rumpf (MER) was an advanced Ph.D. student with ~8 years experience in planetary image interpretation and ~9 years experience in field geology, including an extensive undergraduate field mapping course in the Western USA and several graduate level volcanology field courses in Hawai‘i and New Zealand. Heidi Needham (HN) was an upper-level undergraduate student with no geologic fieldwork experience and limited experience in the processing of GIS data but no terrestrial or planetary mapping experience. MER and HN identified layers along the same transects in both imagery and during fieldwork throughout the implementation of this project. Each field site was mapped in ArcGIS, then visited by MER and HN before the next site was mapped and visited. Early in the project, MER consistently mapped more layers in terrestrial and field interpretations than HN for a given transect. As the project progressed, HN's counts more closely matched MER's counts. Higher counts and resulting lower average flow thicknesses are closer to values of flow thicknesses observed during fieldwork, implying that higher counts of layered flows in LROC images may also be more accurate. HN's increased accuracy throughout this study is a demonstration of the value of field experience, along with image interpretation experience, for planetary scientists. A variety of techniques can be used to study the Earth and planets from inside an office; however, there is no substitute for "boots on the ground" when seeking to understand the natural world.

4.6.3 *Terrestrial Study limitations*

A number of factors contribute to inaccuracies in the study results. Mapping layers of lava flows in imagery is not a precise quantitative process and judgment errors

may either lead to interpretations of layers that are not flows or to not identifying flow units altogether. Many layers in the imagery show neither continuous lateral extents nor consistent vertical sequences due to variability in the degree of erosion, coverage by talus or vegetation, or obscuration by shadows, making it difficult to determine the continuity of layers. Measurements of flow thickness in the field can also be ambiguous. At many outcrops, clinker layers have been eroded and the bottom portion of flows are covered by vegetation, soil, or talus, obscuring the extent of a flow unit, resulting in measured thicknesses that are less than the total thickness of the original flow. A succession of overlapping pāhoehoe lobes may be indistinguishable, so several events may get counted as one, giving a false thickness greater than the thickness of each individual event and artificially increasing the average flow thickness for a transect. Additionally, flow thickness can vary by several tens of centimeters at the scale of an outcrop, adding error of this magnitude to all field measurements. Finally, exact correlation of lava flows mapped in the field to specific layers in the terrestrial imagery is difficult. Handheld GPS units generally have horizontal accuracy of 5–10 m, though it can be as high as 15 m (www.garmin.com), enough possible error to misidentify flows within a sequence when trying to locate an exact position in a remote sensing image. As a result, features in the images must be visually correlated to features in the field to accurately find a location on a satellite image.

Caution should be exercised when describing flow thicknesses estimated from remote sensing data, particularly in the planetary case where ground-truthed comparisons cannot be made. With the image resolutions currently available, individual layers can be distinguished, however a stack of lava flows may not produce breaks in slope between

every flow. Even in the field, when composition and textures between successive flows are similar, it can be difficult to distinguish individual flows. It therefore is infeasible to make highly accurate interpretations of individual lava flows using remote sensing data.

4.6.4 *Lunar Implications*

The accuracy with which mare flow thicknesses can be measured has broad implications for lunar exploration and understanding of the thermal evolution of the Moon and its environment. As one example, exogenous volatiles, including solar wind and solar flare particles and the cosmogenic products of galactic cosmic rays, may be preserved in regolith deposits between lava flows provided that, (1) enough time elapsed between emplacement of subsequent lava flows for a significant regolith cover to develop, and (2) the heat pulse from the overlying lava flow does not fully penetrate the regolith deposits during emplacement, thereby volatilizing the exogenous particles and destroying the record [*Crawford et al.*, 2010; *Fagents et al.*, 2010; *Rumpf et al.*, 2013]. Overestimating the thicknesses of mare basalts will result in the overestimation of the amount of heat available to volatilize particles in regolith deposits, which in turn leads to overestimation of the predicted depths of volatile loss from buried paleoregoliths. In developing recommendations for future lunar exploration, some regions may be erroneously excluded from *in situ* investigation if the thickness of local mare basalts are perceived to be greater than in reality.

Overestimation of lava flow thicknesses can also lead to erroneous calculations of eruption rates, flow velocities, and rheological properties in models of lava emplacement dynamics that rely on flow morphology and dimensions. Basalt flows are commonly

regarded as Bingham plastics: movement is dependent on the yield strength and viscosity of the lava [*Pinkerton and Wilson*, 1994]. *Hulme* [1974] proposed that the thickness of a lava flow is, in part, dependent on material yield strength. Thus, yield strength can be approximated from lava flow thickness measurements. Thickness estimates that are too high will lead to overestimation of flow yield strength. Flow thicknesses are also used to approximate flow duration a flow will be active and volume eruption rates, given flow rheology [*Pinkerton and Wilson*, 1994; *Wilson and Head*, 2003]. Thickness overestimates may lead to misinterpretations of emplacement mechanics and rheology. Jeffreys Equation describes the velocity of a viscous fluid as

$$V = \rho\, g\, h^2 / B\, \eta\, \sin\alpha \quad , \qquad (4.1)$$

where ρ is density, g is gravitational acceleration, h is flow thickness, B is a constant, η is viscosity, and α is the topographic slope in degrees [*Francis and Oppenheimer*, 2004]. Overestimates of flow thicknesses will lead to calculations of flow velocities that are larger than in reality. In addition, the flux of mare basalts with time is calculated based on surface exposures and the thickness of exposed deposits [*Nyquist and Shih*, 1990]. Overestimation of the thickness of individual flow units will not greatly affect average flux rates over long durations, but will lead to overestimation of the flux of individual events, thus misinterpretations of the dynamics of mare flows. *Head and Wilson* [1992] inferred that late-stage mare features are the products of large volume events resulting from the need for progressively larger diapirs with time to overcome the high density of lunar mare rocks in order for magma ascent to be possible. Careful observations of basalt flow thickness trends can further constrain flow volume and eruption rates with time to more precisely interpret the thermal evolution of the Moon.

Finally, prolonged manned missions to the lunar surface will require a high degree of self-sufficiency, demanding that explorers mine needed resources from near the lunar surface [e.g., *Taylor*, 2001; *Duke et al.*, 2006]. Thick lava flows will cool slowly, leading to the possible differentiation and concentration of mineral-bearing crystals needed for development and exploration [*Duke et al.*, 2006]. Misidentification of thick lava flows could lead to selection of sites for exploration that are not as resource-rich as projected.

4.7 CONCLUSIONS

Terrestrial analogs can be used to test our interpretations of volcanic deposits throughout the Solar System. Basalt flow thicknesses were measured on hillsides on O‘ahu Island, Hawai‘i to ground-truth interpretations of layered lava flow thicknesses observed in remote sensing datasets. In eight out of nine ground-truthed transects, remote sensing interpretations of minimum unit thicknesses were greater than those measured in the field by factors up to 3.1. Maximum interpretations of flow thickness from WV2 images were greater than field measurements by factors of 1.3 to 6.3 (Figure 4.12). The overestimation of flow thickness in remote sensing data can be attributed to (1) the inability to discern individual flows within a single outcrop containing multiple flow units, and (2) the high erosional potential of thin pāhoehoe flows, which often form low-sloping terrain between outcrops that may not be distinguishable in satellite images. In addition, ‘a‘ā flow cores are more resistant to erosion than pāhoehoe flows and more likely to be found in outcrops containing multiple flow units, suggesting that the presence of ‘a‘ā flows will lead to

underestimations in flow counts and overestimations in flow thicknesses in remote sensing data.

Data collected by LROC have provided high-resolution views of layered mare flows in large impact craters and pit craters on the Moon. We estimated the average thicknesses of lava flows exposed in the walls of four craters on the lunar nearside; along 41 transects thicknesses range between 1.2 and 29.5 m. The average of all minimum and maximum flow thicknesses estimates were 5.9 and 15.5 m, respectively. Assuming similar morphologies to terrestrial outcrops, these thicknesses represent maximum flow thicknesses for lunar basalts. Overestimation of mare flow thicknesses may lead to erroneous inferences for effusion rates, magma fluxes, and the time-evolution of flow emplacement, as well as to misrepresentation of the preservation potential of ancient exogenous particles in paleoregolith deposits. Improved image resolutions and data processing techniques could increase our ability to distinguish individual lava flows in remote sensing data. However, we argue that interpretations of subtle features such as geologic unit contacts require observations at scales much better than current orbital image resolutions, which in turn argues for continued human or rover surface exploration and in situ field measurements. As has been amply demonstrated by the success of Mars surface missions [e.g., *McEwen et al.*, 2007], only with observations at these fine scales can we begin to fully understand the implications for the geologic processes and surface evolution of planetary bodies.

4.8 ACKNOWLEDGEMENTS

The authors would like to thank the Fred M. Bullard Graduate Fellowship Program, the

NASA Space Grant Consortium, and the McNair Scholarship Program for financial support. Mahalo to J. Sinton and S. Rowland for excellent information on field locations and to K. Trang and E. Fitch for field assistance. Thank you to M. Barbee and the Hawai‘i Coastal Geology Group for WorldView-2 image access.

CHAPTER 5.

CONCLUSIONS

5.1 SUMMARY

This dissertation investigated the preservation potential of exogenous particles in lunar regolith deposits protected by lava flows. The depths to which particles will be volatilized by an overlying lava flow were examined through numerical modeling and laboratory experiments. Lunar lava flow thicknesses were measured through remote sensing techniques and terrestrial analogs. Each dissertation chapter provides specific contributions toward lunar and terrestrial volcanology. Together they form an integrated look at lava–substrate thermal interactions and at the potential discovery of ancient records of Solar System activity near the lunar surface.

Chapter 2 used numerical simulations to determine the maximum depths to which pertinent isotherms will penetrate lunar regolith deposits heated by overlying lava flows. The use of temperature- and depth-dependent properties in models suggested that solar wind volatiles would be disturbed at depths in the regolith that are 60% greater than predicted by models in which constant properties were used. Solar wind implanted particles are predicted to be volatilized to a depth of 20.4 cm beneath a one-meter thick lava flow. At the current average regolith accumulation rate, 204 million years would be required to create a regolith layer of this thickness. These modeled depths represent the minimum thickness of regolith needed to retain a record of exogenous particles.

Chapter 3 presented a set of laboratory experiments measuring the *in situ* heat transfer between molten basalt and lunar regolith simulant. Numerical simulations of experiments constrained the temperature-dependency of the effective thermal conductivity of GSC-1 to vary between 0.35 – 0.45 W m^{-1} K^{-1} at 23 °C and 0.65 – 0.80 W

m^{-1} K^{-1} at 1227 °C. Melt layers 8 – 10 cm thick heated simulant to particle-volatilizing temperatures to depths of 5.6 – 7.2 cm. These depths represent a generous maximum depth to which exogenous particles will be volatilized on the Moon if covered by a flow of similar thickness.

Chapter 4 investigated the accuracy of lava flow thickness estimates made from satellite images of flow sequences exposed in the walls of valleys on O‘ahu and impact craters on the Moon. Sequences of layered lava flows were mapped in terrestrial and lunar remote sensing images. Average thicknesses of flows on the Moon ranged between 1.2 and 29.5 m. Ground-truthing of locations on O‘ahu found that average flow thicknesses were overestimated by factors up to 6.3 based on image analysis. Overestimation is primarily caused by outcrops containing more than one flow that are not distinguishable at available image resolutions. It is likely lunar image interpretations are also overestimated.

As individual projects, the research conducted here contributes toward several outstanding problems in lunar and terrestrial science. Combined, this research provides a basis for the discovery of implanted ancient solar and galactic records in the lunar regolith. Surface regolith samples brought to Earth during the Apollo missions contained solar wind and solar flare particles, and the products of galactic cosmic ray interactions. However, surface deposits have been exposed to space for millions of years complicating the ability to extract a historic record from the deposits [e.g. *McKay et al.*, 1991]. Future “sortie-class” missions to the lunar surface could focus on finding buried paleoregoliths with the goal of extracting ancient solar and galactic records from below the lunar surface. A combination of the techniques used and knowledge gained in this dissertation

would allow for the identification of such deposits. The methods used in Chapter 4 to identified areas of layered basalt sequences can be combined with surface flow age [e.g. Hiesinger et al., 2000, 2002, 2003] to locate potential exploration sites. Although image resolution does not yet allow for the recognition of regolith packets between basalt layers, first-order estimate of the maximum thickness of individual lava flows can be derived from LROC images, as in Chapter 4. Sites will be chosen in areas that display discernable, thin flows and a succession of surface flows spanning > 1 Ga, allowing for maximum duration of regolith development. Once preliminary exploration sites are chosen, numerical models with temperature- and depth-dependent thermophysical property definitions, such as described in Chapters 2 and 3, can be used in conjunction with average flow thickness in the region to determine the minimum amount of regolith required for volatile preservation beneath a mare flow. Determination of specific areas that are most likely to contain pristine deposits of ancient exogenous particles will be recommended as mission exploration sites. During future surface missions, knowledge of local mare flow thicknesses, as investigated in Chapter 4, and of the response of regolith to heating, discussed in Chapter 3, will allow for smoother drilling and extraction of paleoregolith samples.

5.2 POTENTIAL FUTURE WORK

The research conducted throughout the completion of this dissertation has provided answers to pertinent questions in planetary science and volcanology. It has also opened opportunities for further investigations. The numerical models presented in Chapter 2

simulate stagnant flows. I am interested in developing the model further to simulate emplacement and inflation dynamics to determine how these processes affect substrate heating. In addition, our current model fails to include the effects of the movement of volatilized particles from the lunar regolith. Released particles may temporarily pressurize the substrate, raising the effective thermal conductivity and increasing heat transfer rates.

More theoretical work could be implemented in regards to the derivation of effective heat transfer from my experiments. As discussed in Section 3.6.3, it is possible to theoretically predict gas conductivity, radiative conductivity, and the grain-to-grain conductivity of the regolith under lunar conditions as individual components. I would like to conduct a study that includes close examination of the above properties to allow for the distinction between contributing factors in regolith effective conductivity. This would improve my current model and allow for direct application of the study to heat transfer problems on the Moon.

There are several analyses that could be performed on the lava blocks resulting from our experiments. Thin sections were made from the block interiors. These could to be analyzed to quantify the microlite crystallization during cooling and to determine vesicle distribution. In addition, analysis of bubbles formed on the melt surface could constrain the origin of the gas creating the bubbles. I would like to expand experiments to include additional substrate materials. Interesting substrates include solid basalt, assorted sands, and volcanic tephra. I would also like to make more use of the infrared data of external system temperatures during the experiments and to develop the numerical simulation of the experiments in three dimensions to include the lava block and infrared

surface data to consider a treatment of the full system. Experiments looking at the effects of heating and burning of wood samples by a lava flow could be performed to investigate any resulting carbon-14 offsets. Currently, carbon-14 dating is used on samples of wood in volcanic deposits to determine eruption dates, yet it is unknown how interactions with the volcanic products affect carbon fractionation in wood.

Also in Chapter 3, the release of latent heat during cooling of the lava blocks is left largely unexplored. Before submitting that chapter for publication, I plan to conduct an in-depth quantitative analysis of the latent heat measured in my experiments. MELTS and Rhyolite-MELTS will be used to quantify the amount of latent heat available in the Kīlauea basalt used. Study of microlite content in the lava blocks will provide an evaluation of the proportion of quenched material and microlitic material, allowing for an estimate of the actual latent heat potentially released as each block cooled. Non-dimensional numerical analysis of cooling rates in the lava block and in the upper 1 cm of the regolith simulant will allow for recognition of deviations from a strict convective cooling model and the quantification of latent heat release measured during experiments. Comparison of latent heat measured during experiments to potential latent heat will validate our conclusion that delayed cooling in the regolith simulant was caused by release of latent heat from the basalt.

My terrestrial analog study could be expanded to include an in-depth analysis of the effects of emplacement setting on the appearance of terrestrial lava flow sequences in remote sensing images. Sequences of distal, proximal, and intra-caldera flows may be distinguishable in imagery. Identification of distinguishing characteristics could be applied to planetary imagery. Additionally, lava flow thicknesses seen in satellite images

can be used to derive first-order estimates of basalt viscosities and yield strengths for terrestrial and lunar sequences. These estimates can be compared to viscosity and yield strength values that are known from samples or that have been measured during emplacement (for Hawaiian basalts). These comparisons will provide another test as to the accuracy of lava flow thickness measurements made using remote sensing techniques.

REFERENCES

Abtahi, A. A., A. B. Kahle, E. A. Abbott, A. R. Gillespie, D. Sabol, G. Yamada, and D. Pieri (2002), Emissivity changes in basalt cooling after eruption from Pu'u O'o, Kilauea, Hawaii, *Eos Trans. AGU*, *83*(47), *Fall Meet. Suppl.*, Abstract V71A-1263.

Armstrong, J. C., (2010). Distribution of impact locations and velocities of Earth meteorites on the Moon. *Earth, Moon, Planets*, *107*, 43-54.

Armstrong, J. C., L. E. Wellsand, and G. Gonzales (2002), Rummaging through the Earth's attic for remains of ancient life. *Icarus*, *160*, 183-196.

Ashley, J. W., A. K. Boyd, H. Hiesinger, T. Tran, C. H. van der Bogert, R. V. Wagner, and the LROC Science Team (2011), Lunar pits: Sublunarean voids and the nature of mare emplacement. *Lunar Planet. Sci. Conf., 42, #2115.*

Ashley, J. W., M. S. Robinson, A. K. Boyd, R. V. Wagner, E. J. Speyerer, B. R. Hawke, H. Hiesinger, C. H. van der Bogert, K. N. Burnes, and H. Sato (2012), LROC imaging of thin layering in lunar mare deposits, *Lunar Planet. Sci. Conf., 43, Abstract #2115.*

Asimow P. D., and M. S. Ghiorso (1998), Algorithmic modifications extending MELTS to calculate subsolidus phase relations, *Amer. Mineral.*, *83*, 1127-1131.

Blumberg, W. and E.-U. Schlünder (1995), Thermal conductivity of packed beds consisting of porous particles wetted with binary mixtures.

Botterill, J. S. M., A. G. Salway, and Y. Teoman (1989a), The effective thermal conductivity of high temperature beds – I. Experimental determination, *Int. J. Heat Mass Transfer, Vol. 32*, No. 3, 585-593.

Botterill, J. S. M., A. G. Salway, and Y. Teoman (1989a), The effective thermal

conductivity of high temperature beds – II. Model predictions and the implication of the experimental values, *Int. J. Heat Mass Transfer, Vol. 32*, No. 3, 595-609.

Brandeis, G., and C. Jaupart (1987), The kinetics of nucleation and crystal growth and scaling laws for magmatic crystallization, *Contrib. Mineral. Petrol., 96*, 24-34.

Brandeis, G, C. Jaupart, and C . J. Allegre,, (1987), Nucleation, crystal growth, and the thermal regime of cooling magmas, *J. Geophys. Res., 89*, 10161-10177.

Burgi, P., M. Caillet, and S. Haefeli (2002), Field temperature measurements at Erta'Ale lava lake, Ethiopia, *Bull. Volcanol.*, *64*, 472-485.

Büttner, R., B. Zimanowski, J. Blumm, and L. Hagemann, (1998), Thermal conductivity of a volcanic rock material (olivine-melilitite) in the temperature range between 288 and 1470 K, *J. Volcanol. Geotherm. Res., 80*, 293-302.

BVSP (Basaltic Volcanism Study Project) (1981), Basaltic Volcanism on the Terrestrial Planets. Pergamon, New York, 1286.

Carrier, W. D., G. R. Olhoeft, and W. W. Mendell (1991), Physical properties of the lunar surface, in *The Lunar Sourcebook: A User's Guide to the Moon*, edited by G. H. Heiken, D. T. Vaniman, and B. M. French, pp. 475-594, Cambridge University Press, Cambridge.

Carslaw, H. S. and J. C. Jaeger (1986), *Conduction of Heat in Solids*, 510 pp., Oxford University Press, Oxford.

Čermàk, V., H.-G. Huckenholz, L. Rybach, R. Schmid, J. R. Schopper, M. Schuch, D. Stöffler, and J. Wohlenberg (Eds.) (1982), *Physical Properties of Rocks*, *Numerical Data and Functional Relationships in Science and Technology, 1a*, pp. 341-371, Springer-Verlag, New York.

Crawford, I. A., S. A. Fagents, and K. H. Joy, (2007), Full Moon exploration, *Astron. Geophys.*, *48*, 3.18-3.21.

Crawford, I. A., E. C. Baldwin, E. A. Taylor, J. A. Bailey, and K. Tsembelis, (2008), On the survivability and detectability of terrestrial meteorites on the Moon, *Astrobiol.*, *8*, 242-252.

Crawford, I. A., S. A. Fagents, K. H. Joy and M. E. Rumpf (2009), Lunar palaeoregolith deposits as recorders of the galactic environment of the Solar System and implications for astrobiology, *Earth, Moon, Planets*, *107*, 75-85.

Cremers, C. J., R. C. Birkebak, and J. P. Dawson (1970), Thermal conductivity of fines from Apollo 11, *Proc. Apollo 11 Lunar Sci. Conf.*, *3*, 2045-2050.

Crisp, J., A. B. Kahle, and E. A. Abbott (1990), Thermal infrared spectral character of Hawaiian basaltic glasses, *J. Geophys. Res.*, *95*, 21,657-21,669.

Crozaz, G., U. Haack, M. Hair, M. Maurette, R. Walker, and D. Woolum (1970), Nuclear track studies of ancient solar radiations and dynamic lunar surface processes, *Proc. Apollo 11 Lun. Sci. Conf., 3*, 2051-2080.

Cruikshank, D. P., and C. A. Wood (1972), Lunar rilles and Hawaiian volcanic features: Possible analogues, *The Moon, V3*, 4, 412-447.

Danes, Z. F. (1972), Dynamics of lava flows*, J. Geophys. Res., 77*, 1430–1432.

Duke, M. B., L. R. Gaddis, G. J. Taylor, and H. H. Schmitt (2006), Development of the Moon, in *New Views of the Moon*, *Rev. Mineral Geochem*., *60*, 614–639.

Duraud, J. P., Y. Langevin, M. Maurette, G. Comstock, and A. L. Burlingame (1975), The simulated depth history of dust grains in the lunar regolith, *Proc. 6th Lun. Sci. Conf.*, 2397-2415.

Edwards, B.R., J. Karson, R. Wysocki, E. Lev, I. Bindeman, and U. Kueppers (2013), Insights on lava–ice/snow interactions from large-scale basaltic melt experiments, *Geology*, *41*, 851–854.

Eugster, O. (2003), Cosmic-ray exposure ages of meteorites and lunar rocks and their significance, *Chemie der Erde*, *63*, 3-30.

Fagents, S. A. and R. Greeley (2001), Factors influencing lava-substrate heat transfer and implications for thermomechanical erosion, *Bull. Volcanol.*, *62*, 519-532.

Fagents, S. A., R. Greeley, R. J. Sullivan, R. T. Pappalardo, and L. M. Prockter (2000). Cryomagmatic mechanisms for the formation of Rhadamanthys Linea, triple band margins, and other low albedo features on Europa. *Icarus, 144,* 54-88.

Fagents, S. A., M. E. Rumpf, I. A. Crawford, and K. H. Joy (2010), Regolith heating by lunar mare lava flows: Implications for the preservation potential of implanted extra-lunar volatiles. *Icarus, 207*, 595-604.

Fegley, B. and T. D. Swindle (1993), Lunar volatiles: Implications for lunar resource utilization, in *Resources of Near-Earth Space*, edited by J. Lewis, M. S. Matthews and M. L. Guerrieri, pp. 367-426, University of Arizona Press, Tuscon.

Flynn, L. P., P. J. Mouginis-Mark, J. C. Gradie, and P. G. Lucey (1993), Radiative temperature measurements at Kupaianaha Lava Lake, Kilauea Volcano, Hawaii, *J. Geophys. Res.*, *98*, 6461-6476.

Fountain, J. A. and E. A. West (1970), Thermal conductivity of particulate basalt as a function of density in simulated lunar and martian environments, *J. Geophys. Res.*, *75*, 4063-4069.

Francis, P. and C. Oppenheimer (2004), Lava Flows, in *Volcanoes, 2nd Edition*, Oxford

University Press, New York, 142.

Ghiorso, M. S., and R. O. Sack (1995), Chemical mass transfer in magmatic processes. IV. A revised and internally consistent thermodynamic model for the interpolation and extrapolation of liquid-solid equilibria in magmatic systems at elevated temperatures and pressures, *Cont. Mineral. Petrol.*, *119*, 197-212.

Gibson, E. K. and S. M. Johnson (1971), Thermal analysis– inorganic gas release studies of lunar samples, *Proc. 2nd Lun. Sci. Conf.,* 1351-1366.

Gifford, A. N. and F. El-Baz, (1981), Thicknesses of mare flow fronts, *Moon Plan., 24*, 391-398.

Goswami, J. N. (2001), Interactions of energetic particles and dust grains with asteroidal surfaces, *Earth, Planets, Space*, *53*, 1029-1037.

Greeley, R. (1971), Lava tubes and channels in the lunar Marius Hills, *The Moon*, *V3*, 3, 289–314.

Greeley, R. (1974a), Aerial reconnaissance of the geology over the Island of Hawaii, in *Geologic Guide to the Island of Hawaii: A field guide for comparative planetary geology*, NASA-CR152416, 114-183.

Greeley, R. (1974b), Kaumana Lava Tube, in *Geologic Guide to the Island of Hawaii: A field guide for comparative planetary geology*, NASA-CR152416, 233-238.

Greeley, R. (1975), A model for the emplacement of lunar basin-filling basalts, *Lunar Sci. Conf. VI, Houston, Texas,* 309-310.

Greeley, R. (1976), Modes of emplacement of basalt terrains and an analysis of mare volcanism in the Orientale Basin, *Proc. Lunar Sci. Conf. 7th (1976)*, p. 2747-2759.

Griffiths R.W., 2000, The dynamics of lava flows, *Annu. Rev. Fluid Mech. 32*: 477–518.

Grott, M., J. Knollenberg, and C. Krause (2010), Apollo lunar heat flow experiment revisited: A critical reassessment of the in situ thermal conductivity determination, *J. Geophys. Res., 115*, E11005, doi:10.1029/2010JE003612.

Gualda, G. A. R., M. S. Ghiorso, R. V. Lemons, and T. L. Carley (2012), Rhyolite-MELTS: A modified calibration of MELTS optimized for silica-rich, fluid-bearing magmatic systems, *J. Petrol., 53 (5)*, 875-890.

Haskin, L. and P. H. Warren (1991), Lunar chemistry, in *The Lunar Sourcebook: A User's Guide to the Moon*, edited by G. H. Heiken, D. T. Vaniman, and B. M. French, pp. 357-474, Cambridge University Press, Cambridge.

Head, J. W. and L. Wilson (1992), Lunar mare volcanism: Stratigraphy, eruption conditions, and the evolution of secondary crusts, *Geochimica et Cosmochimica Acta*, Vol. 56, 2155-2175.

Hemingway, B. S. and R. A. Robie (1973), Specific heats of lunar basalt, 15555, and soils 15301 and 60601 from 90 to 350 K, *Proc. 3rd Lun. Sci. Conf.,* 355-356.

Hemingway, B. S., R. A. Robie, and W. H. Wilson (1973), Specific heats of lunar soils, basalt, and breccias from the Apollo 14, 15, and 16 landing sites, between 90 and 350˚K, *Proc. 4th Lun. Sci. Conf., Geochim. Cosmochim. Acta*, *3*, 2481-2487.

Hiesinger, H., Head III, J.W., Wolf, U., Jaumann, R., Neukum, G. (2002), Lunar mare basalt flow units: thickness determined from crater size-frequency distributions. *Geophysical Research Letters, 29*, 1248, http://dx.doi.org/10.1029/2002GL014847.

Hiesinger, H., J. W. Head III, U. Wolf, R. Jaumann, and G. Neukum (2003), Ages and stratigraphy of mare basalts in Oceanus Procellarum, Mare Nubium, Mare Cognitum, and Mare Insularum, *J. Geophys. Res., 108*(8), p. 5065, doi:10.1029/2002JE001985.

Hiesinger, H. and J. W. Head (2006), New views of lunar geoscience: An introduction and overview, in *New Views of the Moon*, *Rev. Min. Geochem., 60,* 1-81.

Hiesinger, H., R. Jaumann, G. Neukum, and J. W. Head (2000), Age of mare basalts on the lunar nearside, *J. Geophys. Res.*, *105*, 29,239-29,275.

Hiesinger, H., J. W. Head, U. Wolf, R. Jaumann, and G. Neukum (2002), Lunar mare basalt flow units: Thicknesses determined from crater size-frequency distributions, *Geophys. Res. Lett.*, *29*, doi:10.1029/2002Gl014847.

Hiesinger, H., J. W. Head, U. Wolf, R. Jaumann, and G. Neukum (2003), Ages and stratigraphy of mare basalts in Oceanus Procellarum, Mare Nubium, Mare Cognitum, and Mare Insularum, *J. Geophys. Res.*, *108*(5065), doi:10.1029/2002JE001985.

Hon, K., J. Kauahikaua, R. Denlinger, and K. MacKay (1994), Emplacement and inflation of pahoehoe sheet flows: Observations and measurements of active lava flows on Kilauea Volcano, Hawaii, *Geol. Soc. Am. Bull.,106*, 351-370.

Horai, K., G. Simmons, H. Kanamori, D. Wones (1970), Thermal diffusivity, conductivity and thermal inertia of Apollo 11 lunar material, *Proc. Apollo 11 Lun. Sci. Conf.*, *3*, 2243-2249.

Hörz, F., R. Grieve, G. Heiken, P. Spudis, and A. Binder (1991), Lunar surface processes, in *The Lunar Source Book: A User's Guide to the Moon*, edited by G. H. Heiken, D. T. Vaniman, and B. M. French, pp. 61-120, Cambridge Univ. Press, Cambridge.

Howard, K.A., Head J.W.III (1972), Regional Geology of Hadley Rille. in: Apollo 15: Preliminary Science Report. *NASA SP-289*, 53–58.

Howard K. A., Head J. W., and Swann G. A. (1972), Geology of Hadley Rille, *Proc. Lunar Sci. Conf. 3rd*, 1–14.

Huetter, E. S., N. I. Koemle, G. Kargl, and E. Kaufmann (2008), Determination of effective thermal conductivity of granular materials under varying pressure conditions, *J. Geophys. Res., 113, E12004*, doi:10.1029/2008JE003085.

Hulme, G. (1974), The interpretation of lava flow morphology, *Geophys. J. R. Astron. Soc., 39*, 361– 383.

Joy K. H., D. A. Kring, D. D. Bogard, D. S. McKay, and M. E. Zolensky (2011), Re-examination of the formation ages of Apollo 16 regolith breccias, *Geochim. Cosmochim. Acta*, *75*, 7208-7225.

Joy K. H., Zolensky M. E., Nagashima K., Huss G. R., McKay D. S., Ross D. K., and Kring D. A. (2012), Direct detection of projectile relics from the end of the lunar basin-forming epoch. *Science.* 336, 1426-1429. doi 10.1126/science.1219633.

Keil K., T.E. Prinz, and T.E. Bunch (1971), Mineralogy, petrology and chemistry of some Apollo 12 samples, *Proc. 2nd Lunar Sci. Conf.*, 319-341.

Keszthelyi, L. (1994), Calculated effect of vesicles on the thermal properties of cooling basaltic lava flows, *J. Volcanol. Geotherm. Res., 63*, 257-266.

Keszthelyi, L. (1995), A preliminary thermal budget for lava tubes on the Earth and planets, *J. Geophys. Res.*,*100*, B10, 20,411-20,420.

Keszthelyi, L. and R. Denlinger (1996), The initial cooling of pahoehoe flow lobes, *Bull. Volcanol., 58*, 5-18.

Kickapoo Lunar Research Team and Georgiana Kramer (2014), Stratified ejecta boulders as indicators of layered plutons on the Moon, *Icarus, 228*, 141–148.

Korotev, R. L. (1997), Some things we can infer from the Moon from the composition of the Apollo 16 regolith, *Meteorit. Planet. Sci.*, *32*, 447-478.

Kramer, G. Y (2010), Characterizing bedrock lithologies using small crater rims and ejecta probing (SCREP), *Adv. Space Res.*, *45*, 1257-1276.

Kring, D.L. (2006), Overturned Rim Sequence in *Barringer Crater Guidebook*, LPI Contribution No. 1355, Ch. 6, 53–58.

Lange, R. A. and A. Navrotsky (1992), Heat capacities of Fe_2O_3-bearing silicate liquids. *Cont. Mineral. Petrol.*, *110*, 311-320.

Lange, R. A., K. V. Cashman, and A. Navrotsky (1994), Direct measurements of latent heat during crystallization and melting of a ugandite and an olive basalt, *Cont. Mineral. Petrol.*, *118*, 169-181.

Langseth M. G. Jr., Clark S. P. Jr., Chute J. L Jr., Keihm S., and Wechsler A.E. (1972) Heat-flow experiment, in *Apollo 15 Preliminary Science Report*, NASA SP-289, pp. 11–1 to 11–23.

Langseth M. G. Jr., Keihm S. J., and Chute J. L. Jr. (1973) Heat-flow experiment, in *Apollo 17 Preliminary Science Report*, NASA SP-330, pp. 9–1 to 9–24.

Langseth, M. G., S. J. Keihm, and K. Peters (1976), Revised lunar heat-flow values, *Proc. 7th Lun. Planet. Sci. Conf.*, 3143-3171.

Lev, E., Spiegelman, M., Karson, J., and Wysocki, R., (2012), Investigating lava flow rheology using video analysis and numerical flow models, *J. Volcanol. Geotherm. Res.*, 247–248, 62–73.

Lucey, P. G., R. L. Korotev, J. J. Gillis, L. A. Taylor, D. Lawrence, B. A. Campbell, R. Elphic, B. Feldmann, L. L. Hood, D. Hunten, M. Mendillo, S. Noble, J. J. Papike, R. C. Reedy, S. Lawson, T. Prettyman, O. Gasnault, and S. Maurice (2006), Understanding the lunar surface and space-Moon interaction, in *New Views of the*

Moon, Rev. Mineral. Geochem, *60*, pp. 83-219.

Macdonald, G. A. (1953), Pahoehoe, aa, and block lava, *American Journal of Science, v. 251*, 169-191.

McBirney A. R., and T. Murase (1984), Rheological properties of magmas, *Annu. Rev. Earth Sci.12*, 337–57.

McEwen, A. S., B. S. Preblich, E. P. Turtle, N. A. Artemieva, M. P. Golombek, M. Hurst, R. L. Kirk, D. M. Burr, and P. R. Christensen (2005), The rayed crater Zunil and interpretations of small impact craters on Mars, *Icarus, 176*, 351-381.

McEwen, A.S., and 14 colleagues (2007), Mars Reconnaissance Orbiter's High Resolution Imaging Science Experiment (HiRISE). *J. Geophys. Res., 112*, doi:10.1029/2005JE002605.

McKay, D. S., D. D. Bogard, R. V. Morris, R. L. Korotev, S. J. Wentworth, and P. Johnson (1989), Apollo 15 regolith breccias: Window to a KREEP regolith, *Proc. 19th Lun. Planet. Sci. Conf.,* 19-41.

McKay, D. S., G. Heiken, A. Basu, G. Blanford, S. Simon, R. Reedy, B. M. French, and J. Papike (1991), The lunar regolith, in *The Lunar Source Book: A User's Guide to the Moon*, edited by G. H. Heiken, D. T. Vaniman, and B. M. French, pp. 285-356, Cambridge University Press, Cambridge.

McKay, D. S. (2009), Do lunar pyroclastic deposits contain the secrets of the Solar System?, paper presented at Lunar Reconnaissance Orbiter Science Targeting Meeting, Tempe, Arizona, pp. 77-78.

Melosh, H.J. (1989), Impact Cratering: A Geologic Process, *Oxford Monographs On Geology And Geophysics*, Oxford University Press, No. 11.

Mills, A. F. (1999), Multidimensional and unsteady conduction, in *Heat Transfer, 2nd Ed.*, Prentice Hall, New Jersey, 143-274.

Mouginis-Mark, P.J., Harris, A.J.L., Rowland, S.K. (2007), Terrestrial analogs to the calderas of the Tharsis volcanoes of Mars. In: Chapman, M. (Ed.), *Environments on Earth: Clues to the Geology of Mars*. Cambridge University Press, New York, 71–94.

Mouginis-Mark, P.J., and Rowland, S.K. (2008), Lava flows at Arsia Mons, Mars: Insights from a graben imaged by HiRISE, *Icarus*, *198*, 27–36.

Mouginnis-Mark, P. J., S. K. Rowland, and S. A. Fagents (2011), NASA volcanology field workshops on Hawai‘i: Part 2. Understanding lava flow morphology and flow field emplacement, *Geological Society of America Special Papers*, 483, 401-435,doi:10.1130/2011.2483(01).

Murase, R. and A. T. McBirney (1970), Viscosity of lunar lavas, *Science*, *167*, 1491-1492.

Murase, R. and A. T. McBirney (1973), Properties of some common igneous rocks and melts at high temperatures, *Geol. Soc. Amer. Bull.*, *84*, 3562-3592.

NRC (2007), *The Scientific Context for Exploration of the Moon*, National Research Council, Washington DC (http://www.nap.edu/catalog.php?record_id=11954).

Ono, T., A. Kumamoto, H. Nakagawa, Y. Yamaguchi, S. Oshigami, A. Yamaji, T. Kobayashi, Y. Kasahara, and H. Oya (2009), Lunar Radar Sounder observations of subsurface layers under the nearside maria of the Moon, *Science*, *323*, 90-92.

Ozima, M., K. Seki, N. Terada, Y. N. Miura, F. A. Podosek, and M. Shinagawa (2005), Terrestrial nitrogen and noble gases in lunar soils, *Nature*, *436,* 655-659.

Ozima, M., Q.-Z. Yin, F. A. Podosek, and Y.N. Miura (2008), Toward prescription for

approach from terrestrial noble gas and light element records in lunar soils understanding early Earth evolution, *Proc. Nat. Acad. Sci.*, *105*, 17,65-17,658.

Papike, J., L. Taylor, and S. Simon (1991), Lunar Minerals, in *The Lunar Source Book: A User's Guide to the Moon*, edited by G. H. Heiken, D. T. Vaniman, and B. M. French, Cambridge University Press, Cambridge,121-181.

Papike G. Ryder, and C. K. Shearer (1998), Lunar samples, in *Planetary Materials*, edited by J. J. Papike, pp. 5-1-5-234, Mineralogical Society of America. Washington D.C.

Patankar, S. V., 1980, *Numerical Heat Transfer and Fluid Flow*, Hemisphere Pub. Corp., pp. 15-16.

Patrick, M. R., J. Dehn, and K. Dean (2004), Numerical modeling of lava flow cooling applied to the 1997 Okmok eruption: Approach and analysis, *J. Geophys. Res.*, *109*, B03202, doi:10.1029/2003JB002537.

Pieri, D. C., L. S. Glaze, and M. J. Abrams (1990), Thermal radiance observations of an active lava flow during the June 1984 eruption of Mount Etna, *Geology*, *18*, 1018-1022.

Pinkerton, H., and L. Wilson (1994), Factors controlling the lengths of channel fed lava flows, Bull. Volcanol., 56, 108– 120.

Pinkerton, H., M. James, and A. Jones (2002), Surface temperature measurements of active flows on Kilauea volcano, Hawaii, *J. Volcanol. Geotherm. Res., 113*, 159-176.

Presley, M. A., and P. R. Christensen (1997a), Thermal conductivity measurements of particulate materials 1. Review, *J. Geophys. Res., 102,* 6538-6550.

Presley, M. A., and P. R. Christensen (1997b), Thermal conductivity measurements of

particulate materials 2. Results, *J. Geophys. Res., 102,* 6551-6566.

Ramsey, M. S. and R. J. Lee (2011), Thermal emissivity measurements of molten silicates: implications for lava flow emplacement and hazards, *IUGG XXV General Assembly Abstracts & Programs,* abs. #4184.

Rhodes J. M. and N. J. Hubbard (1973), Chemistry, classification, and petrogenesis of Apollo 15 mare basalts, *Proc. 4th Lun. Sci. Conf.*, 1127-1148.

Robie, R. A., B. S. Hemingway, and W. H. Wilson (1970), Specific heats of lunar surface materials from 90 to 350 K, *Proc. 2nd Lun. Sci. Conf.*, 2361-2367.

Robinson, M. S., S. M. Brylow, M. Tschinnel, D. Humm, S. J. Lawrence, P. C. Thomas, B. W. Denevi, E. Bowman-Cisneros, J. Zerr, M. A. Ravine, M. A. Caplinger, and F. T. Ghaemi (2010), Lunar Reconnaissance Orbiter Camera (LROC) instrument overview, *Space Sci. Rev., 150*, 81-124, doi:10.1007/s11214-010-9634-2.

Robinson, M.S. J.W. Ashley, A.K. Boyd, R.V. Wagner, E.J. Speyerer, B. Ray Hawke, H. Hiesinger, C.H. van der Bogert (2012), Confirmation of sublunarean voids and thin layering in mare deposits, *Planet. Space Sci., 69*, 18–27.

Rowland, S. K., P. J. Mouginnis-Mark, and S. A. Fagents (2011), NASA volcanology field workshops on Hawai‘i: Part 1. Description and history, *Geological Society of America Special Papers*, 483, 401-435, doi:10.1130/2011.2483(01).

Rumpf, M. E., S. A. Fagents, I. A. Crawford, and K.H. Joy (2013), Numerical modeling of lava–regolith heat transfer on the Moon and implications for the preservation of implanted volatiles, *J. Geophys. Res. Planets*, *118*, 382–397.

Schaber, G.G. (1973), Lava flows in Mare Imbrium: Geologic evaluation from Apollo orbital photography, *Proc. Lunar Sci. Conf. 4th,* Houston, TX, 73-92.

Schmitt, H.H., A.W. Snoke, M.A. Helper, J.M. Hurtado, K.V. Hodges,and J.W. Rice, Jr. (2011), Motives, methods, and essential preparation for planetary field geology on the Moon and Mars, Geological Society of America Special Papers, 483, 1-15, doi:10.1130/2011.2483(01).

Schotte, W. (1960), Thermal conductivity of packed beds, *AIChE J., 6*, 63-67.

Schultz, P.H. and P.D. Spudis (1983), Beginning and end of lunar mare volcanism, *Nature, 302*, 233-236.

Sharpton, V. L. (2014), Outcrops on lunar crater rims: Implications for rimconstruction mechanisms, ejecta volumes and excavation depths, *J. Geophys. Res. Planets*, 119, 154–168, doi:10.1002/2013JE004523.

Sherrod, D. R. , J. M. Sinton, S. E. Watkins, and K. M. Brunt (2007), Geologic Map of the State of Hawai‘i, *U.S. Geological Survey, Open-File Report* 2007-1089.

Shoemaker, E. M. (1960), Penetration mechanics of high velocity meteorites, illustrated by Meteor Crater, Arizona, *In Rept. of the Int. Geol. Congress, XXI Session, Norden. Part XVIII*, 418-434.

Shoemaker, E. M. (1963), Impact mechanics at Meteor Crater, Arizona, in B. M. Middlehurst and G. P. Kuiper (Eds.), *The Solar System, 4*, 301-336.

Simoneit, B. R., P. C. Christiansen, and A. L. Burlingame (1973), Volatile element chemistry of selected lunar, meteoritic, and terrestrial samples, *Proc. 4th Lun. Sci. Conf.*, 1635-1650.

Smales A. A., D. Mapper, M. S. W. Webb, R. K. Webster, J. D. Wilson, and J. S. Hislop (1971), Elemental composition of lunar surface material (part 2), *Proc. 2nd Lun. Sci. Conf.*, 1253-1258.

Smith, D.E. et al. (2010), The Lunar Orbiter Laser Altimeter investigation on the Lunar Reconnaissance Orbiter Mission, *Space Sci. Rev*., *150*, 209–241.

Spudis, P.D., Swann, G.A., Greeley, R. (1988), The formation of Hadley Rille and implications for the geology of the Apollo 15 region. *Proceedings of the Lunar Planetary Science Conference 18*, 243–254.

Spudis, P. D. (1996), *The Once and Future Moon*, Smithsonian Institution Press, Washington D.C.

Spudis, P. D. and G. J. Taylor (2009), A Major KREEP-Basalt–Mare Basalt unconformity on the Moon, *40th Lunar Planet. Sci. Conf.,* Abstract #1039.

Swann, G.A. et al. (1972), Preliminary Geologic Investigation of The Apollo 15 Landing Site in: Apollo 15: Preliminary Science Report. *NASA SP-289*, 21–31.

Taylor, G. J., P. H. Warren, G. C. Ryder, J. W. Delano, C. M. Pieters, and G. W. Lofgren (1991), Lunar rocks, in *The Lunar Source Book: A User's Guide to the Moon*, edited by G. H. Heiken, D. T. Vaniman, and B. M. French, pp. 183-284, Cambridge University Press, Cambridge.

Taylor, G. J. (2001), Manufacturing a substrate for the solar cells by the *in situ* melting of the lunar surface: Analysis of the concept, AIAA Aero. Sc. Mtg, Abs. 4577.

Taylor P. T., P. D. Lowman, S. Nagihara, M.B. Milam, and Y. Nakamura (2008), Jurassic diabase from Leesburg, VA: A proposed lunar simulant, *Lun. Planet. Sci. Conf.,* 39, Abs. 2054.

Touloukian, Y. S., W. R. Judd, and R. F. Roy (1981), *Physical Properties of Rocks and Minerals*, *Data Series on Material Properties*, 1-2. McGraw-Hill, New York.

Touloukian, Y. S., W. R. Judd, and R. F. Roy (1989), *Physical Properties of Rocks and*

Minerals, *Data Series on Material Properties, Group II, Properties of special materials*, II-2, Hemisphere Pub. Corp., New York.

Vaniman, D. T., R. Reedy, G. H. Heiken, G. Olhoeft, and W. W. Mendell (1991), The lunar environment, in *The Lunar Source Book: A User's Guide to the Moon*, edited by G. H. Heiken, D. T. Vaniman, and B. M. French, pp. 27-60, Cambridge University Press, Cambridge.

Vondrak, R., J. Keller, G. Chin, and J. Garvin (2010), Lunar Reconnaissance Orbiter (LRO): Observations for Lunar Exploration and Science, Space Sci. Rev., 150, 7–22, doi:10.1007/s11214-010-9631-5.

Watson, K. (1964), The thermal conductivity measurements of selected silicate powders in vacuum from 150 to 350 K, *PhD thesis,* Calif. Inst. Tech., Pasadena, CA.

Wechsler, A. E., and P. E. Glaser (1965), Pressure effects on postulated lunar materials, *Icarus*, *4*, 335-352.

Wechsler, A. E., P. E. Glaser, and J. A. Fountain (1972), Thermal properties of granulated materials, in *Thermal Characteristics of the Moon*, edited by J. W. Lucas, pp. 215-241, MIT Press, Cambridge, Mass.

Weider, S. Z., I. A. Crawford, and K. H. Joy (2010), Individual lava flow thicknesses in Oceanus Procellarum and Mare Serenitatis determined from Clementine multi-spectral data, *Icarus*, *209*, 323-336.

Wentworth, C. K., and Macdonald, G. A. (1953), Structures and forms of basaltic rocks in Hawaii: *U.S. Geol. Survey Bull. 994*, 98.

Wieczorek, M. A., B. L. Jolliff, A. Khan, M. E. Pritchard, B. P. Weiss, J. G. Williams, L. L. Hood, K. Righter, C. R. Neal, C. K. Shearer, I. S. McCallum, S. Tompkins, B. R.

Hawke, C. Peterson, J. J. Gillis, and B. Bussey (2006), The constitution and structure of the lunar interior, in *New Views of the Moon, Rev. Mineral. Geochem., 60,* pp. 221-364.

Wieler, R., K. Kehm, A. P. Meshik, and C. M. Hohenberg (1996), Secular changes in the xenon and krypton abundances in the solar wind recorded in single lunar grains, *Nature, 384*, 46-49.

Wilhelms, D. (1987), Geologic history of the Moon, *U.S. Geol. Surv. Prof. Paper 1348.*

Wilhelms D. E. and McCauley J. F. (1971) Geologic map of the nearside of the Moon. U.S. Geol. Surv. Map I–703.

Williams, D. A., S. A. Fagents, and R. Greeley (2000), A reassessment of the emplacement and erosional potential of turbulent, low-viscosity lavas on the Moon, *J. Geophys. Res.*, *105*, 20,189-20,205.

Willis J. P., A. J. Erlank, J. J. Gurney, R. H. Theil, and L. H. Ahrens (1972), Major, minor, and trace element data for some Apollo 11, 12, 14, and 15 samples. *Proc. 3rd. Lun. Planet. Sci. Conf.*, 1269-1273.

Wilson, L., and J. W. Head (1981), Ascent and eruption of basaltic magma on the Earth and Moon, *J. Geophys. Res., 86(B4)*, 2971– 3001.

Wilson, L., and J. W. Head (1983), A comparison of volcanic eruption processes on Earth, Moon, Mars, Io and Venus, *Nature, 302*, 663– 669.

Wilson, L., and J. W. Head (2003), Lunar Gruithuisen and Mairan domes: Rheology and mode of emplacement, J. Geophys. Res., 108(E2), 5012, doi:10.1029/2002JE001909.

Woodside, W. and J. H. Messmer (1961), Thermal conductivity of porous media. I: Unconsolidated sands, *J. Appl. Phys.*, *32*, *9*, 1688–1699.

Xiao, Z., Z. Zeng, and G. Komatsu (2014), A global inventory of central pit craters on the Moon: Distribution, morphology, and geometry, *Icarus 227*, 195–201.

Yuan, Z.-G., and J. E. Kleinhenz (2011), Measurement of apparent thermal conductivity of JSC-1A under ambient pressure*, 49th AIAA Aerospace Sciences Meeting,* Orlando, FL.

Zanetti, M., H. Heisinger, C. H. van der Bogert, and B. L. Jolliff (2011), Observation of stratified ejecta blocks at Aristarchus Crater, *Lunar Planet. Sci. Conf., 42*, Abstract #2262.

Zolensky M. E. (1997) Structural water in the Bench Crater chondrite returned from the Moon. *Meteorit. Planet. Sci.* 32, 15-18.